Naval Research Laboratory

Washington, DC 20375-5320

NRL/MR/5310--19-9969

Ultra Wideband Time Domain RCS Prediction of Navy Platforms

Sadasiva M. Rao

Radar Analysis Branch
Radar Division

March 26, 2020

REPORT DOCUMENTATION PAGE		*Form Approved* *OMB No. 0704-0188*

1. REPORT DATE *(DD-MM-YYYY)* 26-03-2020	**2. REPORT TYPE** NRL Memorandum Report	**3. DATES COVERED** *(From - To)* 10/01/2016–09/30/2019

4. TITLE AND SUBTITLE Ultra Wideband Time Domain RCS Prediction of Navy Platforms	**5a. CONTRACT NUMBER**
	5b. GRANT NUMBER
	5c. PROGRAM ELEMENT NUMBER PE-61153N
6. AUTHOR(S) Sadasiva M. Rao	**5d. PROJECT NUMBER** NRL/531G5707
	5e. TASK NUMBER EW-53-P048-17
	5f. WORK UNIT NUMBER 1G57
7. PERFORMING ORGANIZATION NAME(S) AND ADDRESS(ES) Naval Research Laboratory 4555 Overlook Avenue, SW Washington, DC 20375-5320	**8. PERFORMING ORGANIZATION REPORT NUMBER** NRL/MR/5310--19-9969
9. SPONSORING / MONITORING AGENCY NAME(S) AND ADDRESS(ES) Office of Naval Research One Liberty Center 875 N. Randolph Street, Suite 1425 Arlington, VA 22203-1995	**10. SPONSOR / MONITOR'S ACRONYM(S)** ONR
	11. SPONSOR / MONITOR'S REPORT NUMBER(S)

12. DISTRIBUTION / AVAILABILITY STATEMENT

DISTRIBUTION STATEMENT A: Approved for public release distribution is unlimited.

13. SUPPLEMENTARY NOTES

14. ABSTRACT

A simple and straight-forward method of moments solution procedure is presented to obtain the radar cross section of an arbitrarily-shaped conducting body in the time domain. The method presented in this report, besides being stable, is also capable of handling mutiple excitation pulses of varying frequency content from different directions in a trivial manner.

15. SUBJECT TERMS

Electromagnetic fields Time domain Integral equations
Method of moments Numerical methods

16. SECURITY CLASSIFICATION OF:			**17. LIMITATION OF ABSTRACT**	**18. NUMBER OF PAGES**	**19a. NAME OF RESPONSIBLE PERSON** Sadasiva M. Rao
a. REPORT Unclassified Unlimited	**b. ABSTRACT** Unclassified Unlimited	**c. THIS PAGE** Unclassified Unlimited	Unclassified Unlimited	89	**19b. TELEPHONE NUMBER** *(include area code)* (202) 404-1985

Standard Form 298 (Rev. 8-98)
Prescribed by ANSI Std. Z39.18

This page intentionally left blank.

ULTRA WIDEBAND TIME DOMAIN RCS PREDICTION OF NAVY PLATFORMS

1. INTRODUCTION

In recent times, the transient analysis of electromagnetic scattering has received a great deal of attention. With the advent of faster computers and an increase of memory space, many scattering problems of complex objects are being performed directly in the time domain. There are various reasons as to why we should be interested in calculating and predicting transient electromagnetic behavior. First, many systems are employing short-pulse radar systems. These systems are being used for target identification, high range resolution, and wide-band digital communications. Although transient data may be obtained by solving the problem in the frequency domain and taking an inverse Fourier or Laplace transform, direct time-domain methods may be better suited and more straight forward to apply. Direct time-domain techniques can generally handle nonlinearities more conveniently. Further, these techniques provide an opportunity to observe and interpret electromagnetic scattering behavior. By noting the return times of various peaks, it may be possible to identify major scattering centers on an object. Also, for certain types of problems, direct time-domain techniques are more efficient where broad-band spectral information is desired. Besides, it seems natural to observe actions and responses as a function of time since return pulses observed from radar or on oscilloscopes are functions of time. Finally, the direct time-domain technique may be viewed as another way to verify results or another tool to understand the complex nature of electromagnetic scattering behavior.

1.1 Methods of Transient Analysis

Of all the available solution techniques to obtain transient responses, the most popular are a) the finite-difference time-domain (FDTD) approach, b) the transmission line matrix (TLM) method, c) frequency domain solutions with inverse Fourier transforms, and d) time-domain integral equation (TDIE) solvers. A more detailed overview of time domain techniques may be found in references [1, 2].

The FDTD method directly solves Maxwell's differential equations in the time domain and was initially presented by Yee [3]. In this method, the scatterer and the surrounding infinite space are discretized into cubical cells. The spatial and temporal derivatives in Maxwell's equations are approximated by a set of finite difference equations. An explicit expression may be obtained by "leap frogging" the electric and magnetic fields in space and time. This means that the fields at one time instant depends only upon the fields at previous time instants. This explicitness aids in speeding up the computation time. An advantage of FDTD is that it can model complex structures including inhomogeneous materials rather easily. However, in order to obtain a numerical solution, the discretization grid has to be truncated at a suitable distance from the scatterer. Also, problems arise from spurious reflections at the lattice truncation boundaries and the modeling of curved structures with stair step approximations. In three-dimensional cases, the memory requirement is large due to the fact that six field quantities and three material parameters need to be stored for each cell. Finally, if the angle of incidence, polarization, or time variation of the incident field is changed, the solution procedure must be started all over again.

Manuscript approved February 6, 2020.

The TLM method was developed by Johns and Beurle [4] in which space is modeled as an interconnection of transmissions lines and may be considered as a discretized form of Huygen's principle. By calculating the shunt voltages and currents at each node, the field quantities may be obtained. Like FDTD, TLM is a time stepping procedure in which the currents and voltages at one time instant are written explicitly in terms of currents and voltages of previous time steps. The impulse response may be obtained by exciting the mesh with an ideal Dirac impulse function. Therefore, the response to a general waveform (with frequency content below the mesh cutoff frequency) may be obtained by convolution of the output impulse function with the desired excitation function. However, if the polarization or angle of incidence of the excitation field is changed, the solution must be performed again. TLM suffers from similar computer storage problems of FDTD in that the material parameters, voltages, and currents need to be stored at each node. TLM also experiences dispersion problems where frequency components experience different velocities due to the discrete nature of the mesh.

The classical frequency domain approach solves for the induced current or the scattered fields from a scatterer for a range of frequencies from the lower end to the upper end and then performs an inverse Fourier transform. The solution at each frequency may be carried out by using the quasi-static solution or the method of moments at low frequencies and the geometrical theory of diffraction (GTD) or the physical theory of diffraction (PTD) approximations at higher frequencies. In the low frequency range, MOM is the preferred approach wherein integral equations are formed by enforcing boundary conditions on the electromagnetic fields [5]. The integral equation techniques are generally confined to the scattering structure, and the radiation condition is automatically enforced. In this solution method a set of basis functions with unknown weight are used to represent the unknown quantities, and a matrix equation is obtained by testing the integral equations with a set of testing functions.

Some of the early analytical work in transient electromagnetic problems were based on physical optics to obtain the approximate impulse response from conducting flat plates, spheres, and prolate spheroids [6]. A time domain solution for an infinite cylindrical antenna was performed by Wu in 1961 [7]. Bennett observed that an integro-differential equation obtained by enforcing the boundary conditions of the tangential field components on the surface of the scatterer could be solved for directly in the time domain [8]. This technique has been labeled the marching-on-in-time (MOT) algorithm or the space-time integral-equation (STIE) technique. Like MOM, the MOT method discretizes the scatterer into segments or patches. The time axis is generally divided into equal increments. With this method, the currents on the scatterer at a certain time $t = t_1$ are related to the currents on the scatterer at $t < t_1$. This is because the "effect" of a current requires a finite time to "travel" to the observation point. By properly choosing a time step, an explicit solution for the present-time currents may be obtained which may be solved iteratively. So, once the currents at t_1 are determined, the time is incremented to the next interval, and the procedure is repeated.

Although MOT or STIE solutions have been attempted for complex problems, until recently, most radar cross section (RCS) prediction algorithms have been developed in the frequency domain (FD) using Maxwell equations as the starting point and assuming time-harmonic behavior. Hence, whenever there is a time domain (TD) RCS signature requirement, it is a common practice to model the given object suitable for FD solution, run the algorithm at a number of frequencies, and use the Inverse Discrete Fourier Transform (IDFT) to accomplish the task. It should be noted that except for some simple canonical problems, TD RCS calculations are prohibitively expensive, since the calculations must be repeated for different frequencies where each frequency calculation requires substantial computational resources. To alleviate computational burden, recent efforts for predicting TD RCS for complex objects are concentrated in solving the problem directly in the time domain.

In theory, direct TD prediction techniques are inherently superior to FD techniques by providing the signature for a wideband of frequencies from a single set of calculations. We note that the TD methods provide several other advantages, such as: 1) more suitable for ultra-wideband signature studies 2) provide better visual representation for understanding the field interactions and, 3) computationally more efficient when solution is required over a large band of frequencies.

Generally, all the available TD prediction techniques may be classified into two categories: a) Differential equation (DE) based solution methods, such as Finite Difference Time Domain (FDTD) method [3], and b) Integral equation (IE) based solution methods. In this work, we only consider IE based methods.

Next, we note that the IE based TD solution is invariably obtained by a time-stepping process popularly known as the Marching-on-in-Time (MOT) method [9]. The main advantage of MOT method is that, when used as an explicit scheme, requires no matrix inversion, a computationally intensive step in any numerical algorithm [9]. Unfortunately, the MOT procedure is prone to late-time instabilities and there have been several proposed remedies to overcome this problem [9–13]. However, most of the proposed remedies only try to arrest the instabilities, work only for simple problems, and invariably fail for complex objects. Even the implicit schemes in TD, which require a matrix-inversion, are vulnerable to instability problem [9] and hence of little use to a practicing engineer.

Recently, a new type of algorithm was developed to obtain TD RCS by a process known as marching-on-in-degree (MOD) method [14–16]. In this method, the time variable is modeled by a series of decaying polynomials *viz.* Laguerre Polynomials. The underlying philosophy is that the decaying functions would not be prone to late-time instabilities. Although the MOD solution scheme appears to suppress instabilities, in our experience, the procedure, as appeared in the published literature, is computationally intensive requiring a large number of time functions even for simple canonical problems.

Another important limitation of all the available TD methods, whether the method is DE or IE based, is the inability to process multiple excitations in an economical manner. Since all the TD methods are some sort of iterative methods, the solution has to be obtained for each excitation separately. Mathematically speaking, if x is the amount of time to solve one incident field, then nx is the total time required for n incident fields. This is in complete contrast to the frequency domain solution, where handling multiple excitations is a trivial task *viz.* IE based frequency-domain method of moments (FD-MOM) solution technique [5]. In the FD-MOM solution, once the matrix is formed and inverted, thousands of incident fields can be processed with a fraction of total computation time. However, in FD-MOM, only one frequency can be handled at a time because once the frequency is changed, the whole solution process must be restarted.

In this work, we present a new TD solution method based on conventional method of moments (MOM) solution procedure, ideally suited to handle a large number of excitations in a trivial manner. The method presented in this work can handle multiple incident pulses, with varying frequency signature bands, in a trivial manner with only a fraction of additional cost as compared to a single incident field, a very useful feature not available via frequency-domain MOM. We further emphasize that a) all the previous time-marching solutions, although efficient, are plagued by instability problems. The source of instability is primarily the method itself where the accumulation of error occurs at each time step. For many practical cases, the previously available methods are simply useless. The new method is based on entirely a new line of thinking where the error is suppressed in both time and space. There is no time marching involved in this procedure. Further, this new algorithm remains stable for a very long solution time. In the following Chapters, we present the evolution of the method with detailed mathematical steps, numerical solution procedure, and numerical results. The numerical results in each case are compared with data obtained using the FD-MOM plus IDFT procedure.

2. WIRE-GRID MODELING OF ARBITRARY BODIES - FULL MATRIX APPROACH

In this chapter, a stable solution method is presented to obtain scattering response from arbitrary wire structures illuminated by a Gaussian plane wave directly in the time domain. Although the method presented in this chapter is not efficient, it forms the basis for a new and highly efficient method presented in later chapters. The method presented in this chapter represents a new way of approaching the problem. Further, contrary to all the available time domain algorithms until now, this method, besides being stable, is also capable of handling multiple excitations in a trivial manner. The new procedure is based on the conventional method of moments and utilizes standard pulse functions for expansion of the space variable and time-shifted Gaussian functions for the time variable. The testing procedure is accomplished by collocation. The numerical results obtained using the new procedure are validated by comparing with the data obtained from the frequency domain solution using the same modeling scheme and performing aninverse discrete Fourier transform.

2.1 Wire-Grid Modeling of Arbitrary Surface

Figure 1 shows several conducting objects modeled by a series of electrically short, straight wires to be used in the numerical scheme. In this scheme, we assume a constant radius for each wire although it is not required for the solution procedure. Note that all the wire-grid models include wire junctions where several wires are attached to a common point, referred to as *node*. Thus, each node, in general, will have multiple wires connected to it, except the *boundary node* where only one wire is connected. We note that, in the present work, the induced current is calculated at the nodes via MOM procedure. In the next two sections, we present mathematical steps and MOM solution procedure for a single, arbitrarily-oriented wire for the sake of brevity and discuss modifications necessary to include wire-junctions.

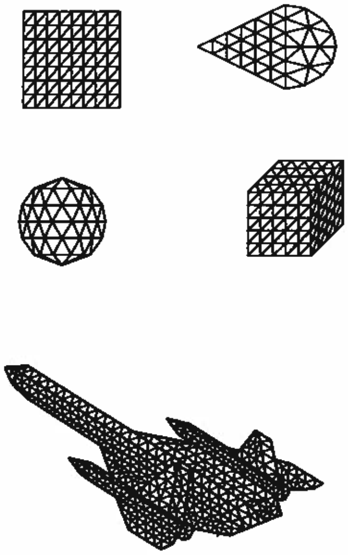

Fig. 1 — Wire-grid model of conducting objects

2.2 Mathematical Formulation

Let S denote an open or closed perfectly conducting, arbitrarily-oriented wire of radius a, modeled by a series of straight wire segments, as shown in Figure 2.

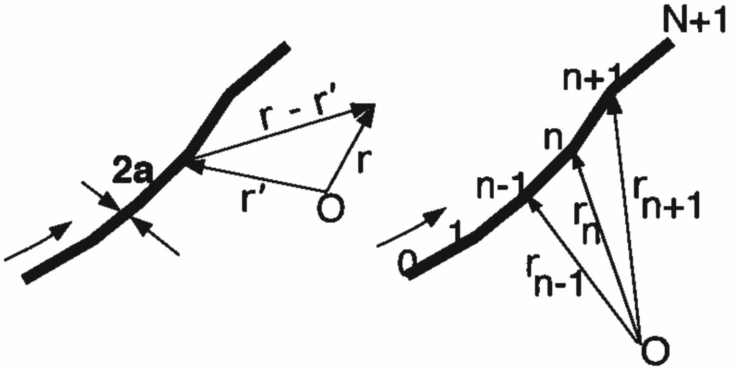

Fig. 2 — Arbitrary wire divided into subdomains

An electric field $E^i(t,\mathbf{r})$, defined in the absence of the scatterer, is incident on and induces a surface current $I(t,\mathbf{r})$ on S. Using basic mathematical steps outlined in [9], the scattered electric field $E^s(t,\mathbf{r})$ computed from the surface current is given by

$$E^s(t,r) = -\frac{\partial A(t,r)}{\partial t} - \nabla\Phi(t,r), \tag{1}$$

where the magnetic vector potential and the electric scalar potentials are given by

$$A(t,r) = \mu \int_\ell \frac{\hat{s}' I(t-R/c,r')}{4\pi R}\, d\ell' \tag{2}$$

and

$$\Phi(t,r) = \frac{1}{\varepsilon} \int_\ell \frac{q_\ell(t-R/c,r')}{4\pi R}\, d\ell'. \tag{3}$$

In Eqs. (2) and (3), $\hat{s}'$ represents the unit vector of the source term along the wire axis, $R = \sqrt{|r-r'|^2 + a^2}$, μ and ε denote the permeability and permittivity of the surrounding medium, respectively, r and r' are the locations of the observation and source points on the wire, a is the radius, and c is the velocity of the electromagnetic wave. Also, ℓ represents the parameter along the length of the wire. The linear charge density q_ℓ is related to the induced current I by

$$\frac{\partial q_\ell}{\partial t} = -\frac{\partial I}{\partial \ell}. \tag{4}$$

Differentiating Eq. (1) with respect to time and using Eq. (4), we obtain the following expression for the time derivative of the scalar potential as

$$\Psi \triangleq \frac{\partial \Phi}{\partial t} = \frac{-1}{\varepsilon} \int_{\ell} \frac{\partial I(t - R/c, r')/\partial \ell}{4\pi R} \, d\ell'. \tag{5}$$

The integro-differential equation for I can be derived using the boundary condition $(E^i + E^s)_{tan} = 0$ on S as

$$\left[\frac{\partial A}{\partial t} + \nabla \Phi\right]_{tan} = E^i_{tan}. \tag{6}$$

The charge density appearing in the scalar potential of Eq. (6) may be eliminated by differentiating Eq. (6) with respect to time and using Eq. (5). Thus, the electric field integral equation for an arbitrary wire in the time domain is given by

$$\left[\frac{\partial^2 A}{\partial t^2} + \nabla \Psi\right]_{tan} = \left[\frac{\partial E^i}{\partial t}\right]_{tan} \tag{7}$$

which needs to be solved for the unknown current $I(t,r)$.

2.3 Method of Moments Solution Procedure

For numerical purposes, the wire is divided into $N+1$ linear segments. The position vector r_n, $n = 0, 1, \ldots, N+1$, defined with respect to the global coordinate origin $\bigcirc$, represents the beginning point of each linear segment along the wire axis. Although not included in the present work, notice that, we can assign different radii for each segment which allows us to model wire structures with non-uniform radius. Further, we divide the time axis into uniform time intervals given by Δt and denote $t_m = m\Delta t$ for $m = 0, 1, 2, \ldots.\infty$.

Next, we discuss the numerical solution procedure to solve Eq. (7) using the method of moments. As a first step, define a set of basis functions for time variable t and space variable ℓ, given by

$$f_m(t) \equiv e^{-\left(\frac{t - m\Delta t}{\Delta t}\right)^2} \quad 0 < t < \infty \tag{8}$$

and

$$g_n(\ell) \equiv \begin{cases} 1 & \ell_{n-\frac{1}{2}} \le \ell \le \ell_{n+\frac{1}{2}} \\ 0 & \text{otherwise.} \end{cases} \tag{9}$$

where $\ell_{n\pm\frac{1}{2}} = \ell_n \pm \frac{\Delta\ell}{2}$. Note that Eq. (8) represents time-shifted Gaussian functions utilized for representing the time variable. Since these functions span the time interval 0 to ∞, they can be considered as entire domain basis functions. We further note that the Gaussian functions decay as time progresses, reach zero at infinity, easily differentiable, not prone to late-time instabilities, and well-suited for the present work. Further, the pulse functions, defined in Eq. (9) to represent the space variable ℓ, are standard subdomain basis functions commonly used in the FD-MOM scheme. Also, note that the node points, excluding the boundary nodes, refer to the unknowns in space and the current pulse function spans half-pulse distance on either side of the node. This type of description satisfies the required Kirchoff's current law.

Using Eqs. (8) and (9), the induced current $I(t,\ell)$ for the first M time steps is approximated as

$$I(t,\ell) \approx \sum_{m=1}^{M} \sum_{n=1}^{N} I_{m,n}\, f_m(t)\, g_n(\ell) \tag{10}$$

where $I_{m,n}$ represents the unknown coefficients to be determined by the MOM procedure. Note that there are $P = M \times N$ number of unknowns in this scheme and M denotes the number of time steps required to represent the incident pulse adequately.

2.3.1 Testing Procedure

For testing purposes, we use delta functions for both time and space variables in accordance with the collocation scheme. Thus, we can write Eq. (7) after testing as

$$\frac{\partial^2 A_n(t_m)}{\partial t^2} + \frac{\partial \Psi_n(t_m)}{\partial \ell} = F_n(t_m) \tag{11}$$

for $m = 1, 2, \cdots M$ and $n = 1, 2, \cdots N$, where

$$A_n(t_m) = a_n \cdot A(t_m, \ell_n) \tag{12}$$

$$\frac{\partial \Psi_n(t_m)}{\partial \ell} = a_n \cdot \nabla \Psi(t_m, \ell_n) \tag{13}$$

$$F_n(t_m) = a_n \cdot \frac{\partial E_n^i(t_m)}{\partial t} \tag{14}$$

and a_n is the unit tangential vector at $\ell = \ell_n$.

Using finite difference approximation for time and space derivatives, we may re-write Eq. (11) as

$$\frac{A_{m+1,n} - 2A_{m,n} + A_{m-1,n}}{\Delta t^2} + \frac{\Psi_{m,n+\frac{1}{2}} - \Psi_{m,n-\frac{1}{2}}}{|\ell_{n+\frac{1}{2}} - \ell_{n-\frac{1}{2}}|} = F_{m,n} \tag{15}$$

where $A_{m,n} = A_n(t_m)$, $\Psi_{m,n} = \Psi_n(t_m)$, and $F_{m,n} = F_n(t_m)$. Lastly, by replacing the time index m by $m-1$, we have

$$\frac{A_{m,n} - 2A_{m-1,n} + A_{m-2,n}}{\Delta t^2} + \frac{\Psi_{m-1,n+\frac{1}{2}} - \Psi_{m-1,n-\frac{1}{2}}}{|\ell_{n+\frac{1}{2}} - \ell_{n-\frac{1}{2}}|} = F_{m-1,n} \tag{16}$$

Next, we consider the expansion procedure.

2.3.2 Expansion Procedure

Using Eq. (10), $A_{m,n}$, as defined in Eq. (12) , may be written as

$$A_{m,n} = \mu \sum_{i=1}^{M} \sum_{j=1}^{N} I_{i,j}\, f_i(t_m - \frac{R_{n,j}}{c})\, [a_n \cdot a_j] \kappa_{n,j} \tag{17}$$

where

$$\kappa_{n,j} = \int_{\ell_j} \frac{d\ell'}{4\pi R_n}, \tag{18}$$

$R_n = |r_n - r'|$, $R_{n,j} = |r_n - r_j|$, and a_j is the unit tangential vector at $\ell = \ell_j$.

Next, let us consider the evaluation of $\Psi_{m,n}$. Considering Eq. (5), replacing the derivative operation with finite difference approximation, and substituting Eq. (10), we have

$$\Psi_{m,n} = \frac{-1}{\varepsilon} \sum_{i=1}^{M} \sum_{j=1}^{N} I_{i,j} \frac{1}{|\ell_{j+\frac{1}{2}} - \ell_{j-\frac{1}{2}}|} \times \left[f_i(\tau_{m,n,+\frac{1}{2}})\, \kappa_{n,j+\frac{1}{2}} - f_i(\tau_{m,n-\frac{1}{2}})\, \kappa_{n,j-\frac{1}{2}} \right] \tag{19}$$

where

$$\kappa_{n,j\pm\frac{1}{2}} = \int_{\ell_{j\pm\frac{1}{2}}} \frac{d\ell'}{4\pi R_n}, \tag{20}$$

$$R_{n,j\pm\frac{1}{2}} = |r_n - r_{j\pm\frac{1}{2}}| \tag{21}$$

$$\tau_{m,n,j\pm\frac{1}{2}} = t_m - \frac{R_{n,j\pm\frac{1}{2}}}{c} \tag{22}$$

Using the expansion and testing procedures described so far, it is trivial to generate a matrix equation $ZX = Y$ of dimension $P = M \times N$. The elements of Z-matrix are formed by assembling either $A_{m,n}$ and $\Psi_{m,n}$. Note that this matrix is not a dense matrix because of the causality condition. The right hand side Y involves the incident field terms which is trivial to calculate once the incident wave form is described. By solving the matrix equation, using any of the standard matrix equation solving methods such as Gaussian elimination or LU-decomposition, it is simple to obtain the induced current at all locations for the first M time steps. It is obvious, at this stage, to note that multiple incident fields can be processed in a trivial manner with this procedure by adding more columns to Y-matrix.

In order to generate the response for next M time steps, we note that only the right hand side of the matrix equation needs to be modified. We note that for this case, the right hand side would be $Y - \overline{Z}X_{pre}$ where X_{pre} represents the coefficients already calculated for zero to M-steps and $\overline{Z}$ represents the matrix containing vector and scalar potential terms contributing to zero to M time steps. The $\overline{Z}$-matrix can be obtained in the same manner as Z-matrix. Also note that $\overline{Z}$-matrix need not be inverted and does not require to be stored. Hence, obtaining induced current for $M+1, \cdots, 2M$ is a trivial task. This process can be easily repeated for as many multiples of M-time steps and can be terminated when the norm of the right hand side at the k^{th}-multiple of M-time steps falls below a pre-determined value, *i.e.* less than 10^{-4}, when compared to the norm of the first multiple of M- time steps.

2.3.3 Application to Multiple Wires and Wire-Junctions

The analysis described so far is only applicable to a single, arbitrarily-oriented wire. However, to apply for more complex cases, we recognize that, referring to Figure 2, the induced current is evaluated at node points $n = 1,\ldots,N$. Note that the node points r_0 and r_{N+1} are excluded since the current is zero at these locations or, in other words, referred to as *boundary nodes*. One easy way to distinguish a boundary node is to note that only one wire segment is attached to it. For a non-boundary node, the number of wires attached must be two or more. If only two wires are connected to the non-boundary node then we have a simple arbitrary wire and that node would support just one basis function. However, if K number of wires are attached to the non-boundary node, then we have a junction node and $K-1$ basis functions must be defined for this node. Assuming that the current flows from lower number wire segment to higher numbered wire segment, the Kirchoff's current law is automatically satisfied in this procedure for the wire-grid model.

Next, we note that a wire-grid model for a truly arbitrary body can be generated by specifying two sets of input data. The first is an indexed list or **node matrix** of position vectors $r_i = (x_i, y_i, z_i), i = 1, 2, \cdots, N_v$. The components of the vectors r_i are the Cartesian coordinates of the i^{th} vertex with respect to a global coordinate system. The second set of data is an **edge matrix**

$$E = [e_{ij}], \quad i = 1, 2, \cdot, N_e; \ j = 1, 2 \ , \tag{23}$$

in which is listed in the i^{th} row the indices of the two vertices to which the i^{th} edge is connected.The vertex and the edge matrix together completely determine the surface geometry and would be amenable for further processing to obtain a wire-grid model. Since, the non-boundary nodes support the basis functions required for the TD calculation, we note that identifying the non-boundary nodes and calculating the total number of basis functions from the given set of data can be carried out in the pre-processing stage efficiently. We further note that multiple wire-grids can be handled in a similar way.

2.3.4 Far-Field Calculation

Once the transient currents on the scatterer have been determined, we can calculate the electric and magnetic fields anywhere outside the scatterer using the following procedure.

First of all, we note that the scattered magnetic field, $H^s(t,r)$, at a point r is related to the induced currents by

$$H^s(t,r) \ = \ \frac{1}{\mu}\nabla \times A = \nabla \times \int_\ell \frac{\hat{s}'\, I(t-\frac{R}{c},r')}{4\pi R}\, d\ell' \tag{24}$$

where $R = \sqrt{|r-r'|^2 + a^2}$. Taking the curl operator inside the integral and using the vector identity $\nabla \times (wA) = w\nabla \times A + \nabla w \times A$, results in

$$H^s(t,r) \ = \ \int_\ell \left[\frac{\nabla \times \hat{s}'\, I(t-\frac{R}{c},r')}{4\pi R} - \frac{a_R}{4\pi R^2} \times \hat{s}'\, I(t-\frac{R}{c},r') \right] d\ell'. \tag{25}$$

where a_R is a unit vector in the direction $r - r'$. Since we are restricting ourselves to the far field, we may neglect the second term in Eq. (25). Using simple algebra, we have

$$\nabla \times \hat{s}' \, I(t - \frac{R}{c}, r') = \frac{1}{c}\frac{\partial I}{\partial t_R}\hat{s}' \times a_R \tag{26}$$

where $t_R = t - \frac{R}{c}$. Substituting Eqs. (10) and (26) into Eq. (25) gives

$$H^s(t_n, r) \approx \sum_{k=1}^{N} \frac{1}{c}\frac{\partial I_k(t_R)}{\partial t_R}\int_\ell \frac{\hat{s}' \times a_R}{4\pi R}\, d\ell'. \tag{27}$$

For far field calculations, we can make the following approximations: $R \approx r$, for magnitude terms where $r = |r|$, $R \approx r - r' \cdot a_r$, for time retardation terms, and $a_R \approx a_r$. The time derivative of the current is approximated with a finite difference approximation.

The far-scattered electric field may then be obtained with

$$E^s(t_n, r) = \eta H^s(t_n, r) \times a_r \tag{28}$$

where η is the wave impedance in the medium surrounding the scatterer.

2.4 Numerical Results

In this section, we present numerical results for several representative example problems illuminated by a Gaussian plane wave, given by

$$E^i(t, r) = E_o \frac{4}{T\sqrt{\pi}} e^{-\gamma^2} \tag{29}$$

with

$$\gamma = \frac{4}{T}(ct - ct_o - r \cdot a_k), \tag{30}$$

where a_k is the unit vector in the direction of propagation of the incident wave, T is the pulse width of the Gaussian impulse, $E_o \cdot a_k = 0$, r is a position vector relative to the origin, c is the velocity of propagation in the external medium, and t_o is a time delay which represents the time at which the pulse peaks at the origin. The time delay is introduced to ensure a smooth rise of the incident field from a zero value. The pulse width T is defined such that for $ct - ct_o - r \cdot a_k = \pm\frac{T}{2}$, the exponential has fallen to about 2% of its peak value. For all example problems, we have $E_o = 120\pi a_x$, $ct_o = 6.0$ LM, $T = 4.0$ LM, and $k = -a_z$. Note that 1 LM = 3.333 nSecs. Further, for all example problems, the wire radius is chosen equal to 0.001m.

Next, we note that the incident field, as described by Eqs. 29 and 30, reaches it's maximum value at 6 LM and essentially becomes zero at 12 LM. Thus, for all the example problems, we approximate the time variable by 60 Gaussian functions spanning $0 - 12$ LM, each one shifted by 0.2 LM, except for the aircraft-like structure example where 30 functions have been used to keep the matrix size smaller. The IDFT solution, for comparison purposes, is obtained by using the same wire-mesh as used for the TD solution and sampled at 256 equally spaced frequency points in the interval 0 – 400 MHz.

As a first example, consider three straight wires, each 2.0 m long, placed along the x, y, and z axes and joined at the origin, as shown in the inset of Figure 3. Each wire is divided into 10 segments and the wire-junction is illuminated by a Gaussian plane wave described by Eq. 29. The induced current at the center of the wire placed along the x-axis is obtained using the new procedure and shown in Figure 3. The result is compared with the FD-MOM solution. There are 30 and 60 basis functions for space and time variables, respectively, for the time domain solution. Hence the matrix size for this problem is $30 \times 60 = 1,800$. Since the wires are high-Q structures, the induced current remains significant for a very long time and both solutions compare very well throughout. Further, the new TD solution remains stable in the late time as seen in the second part of the figure spanning from 60 to 300 LM. The x-component of the scattered electric far-field is shown in Figure 4 and compared with the IDFT solution. The scattered far-field is obtained in the back-scattered direction, *i.e.* along the a_z-axis. Again, we note good comparison in the two solutions.

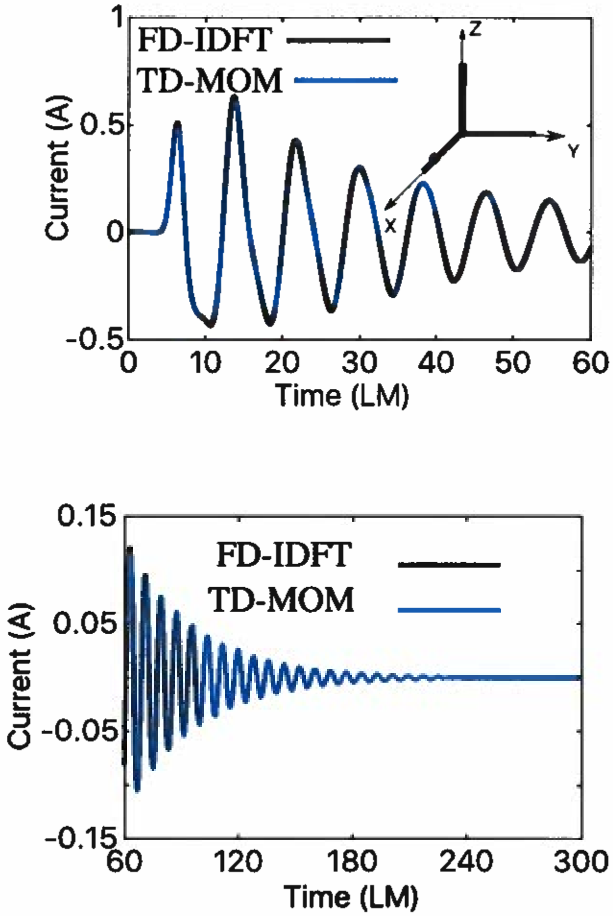

Fig. 3 — Current induced on a 3-wire structure illuminated by a Gaussian plane wave. The wire radius=0.001 m

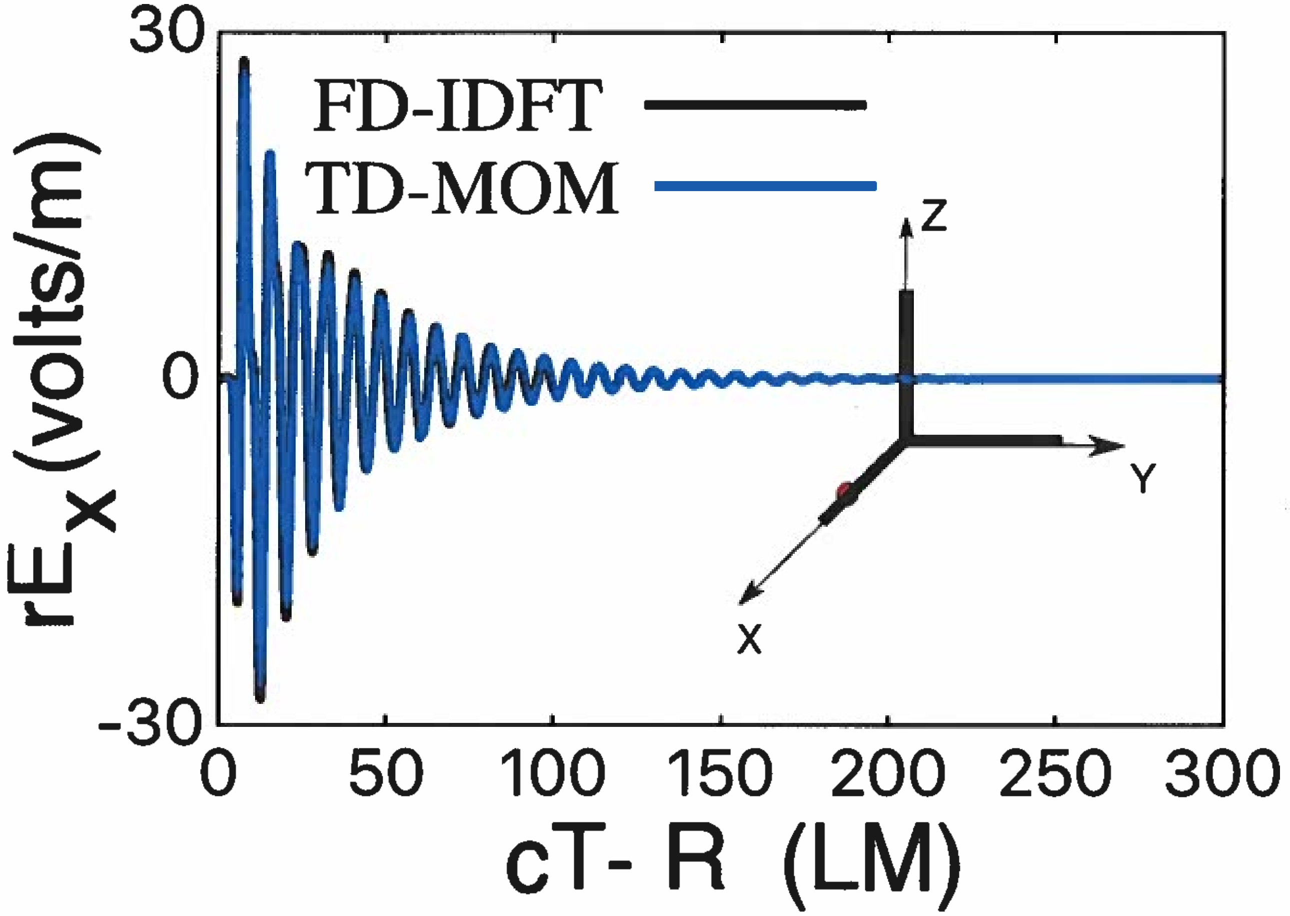

Fig. 4 — X-component of the scattered electric field from the 3-wire structure illuminated by a Gaussian plane wave.

Next, consider a wire-mesh arranged in the shape of a square plate of 1.0 × 1.0 m, located in the XY-plane. The mesh is illuminated by a Gaussian plane wave described by Eq. 29. The induced current at the center of the mesh, highlighted by a dot in the inset of Figure 5, is obtained using the new procedure and compared with the FD-MOM solution. There are 377 and 60 basis functions for space and time variables, respectively, for the time domain solution. Hence the matrix size for this problem is $377 \times 60 = 22,620$. Although, the matrix size is large, it is a sparse matrix with many zeros. Both TD and IDFT solutions compare very well, as shown in Figure 5, and remain stable in the late time as seen in the second part of the figure spanning from 60 to 300 LM.

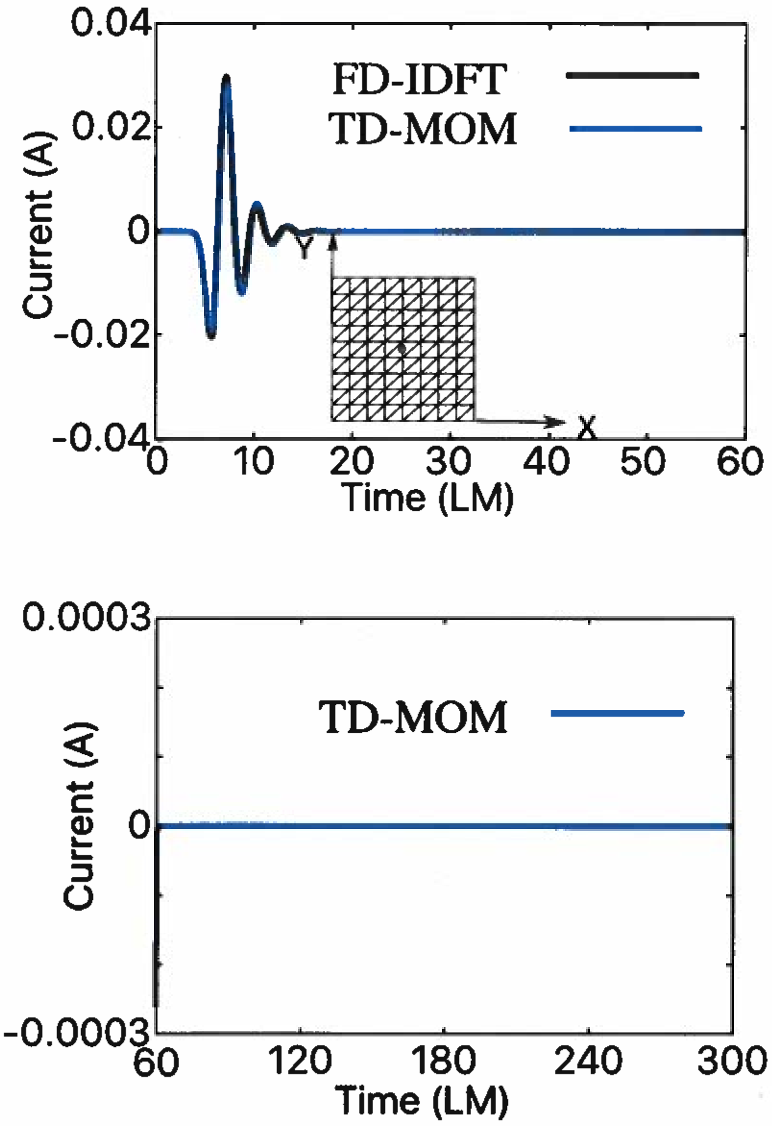

Fig. 5 — Current induced on a wire-mesh model of a square plate illuminated by a Gaussian plane wave. The wire radius=0.001 m

The x-component of the scattered electric far-field is shown in Figure 6 and compared with the IDFT solution. The scattered far-field is obtained in the back-scattered direction, *i.e.* along the a_z-axis. Again, we note good comparison in the two solutions.

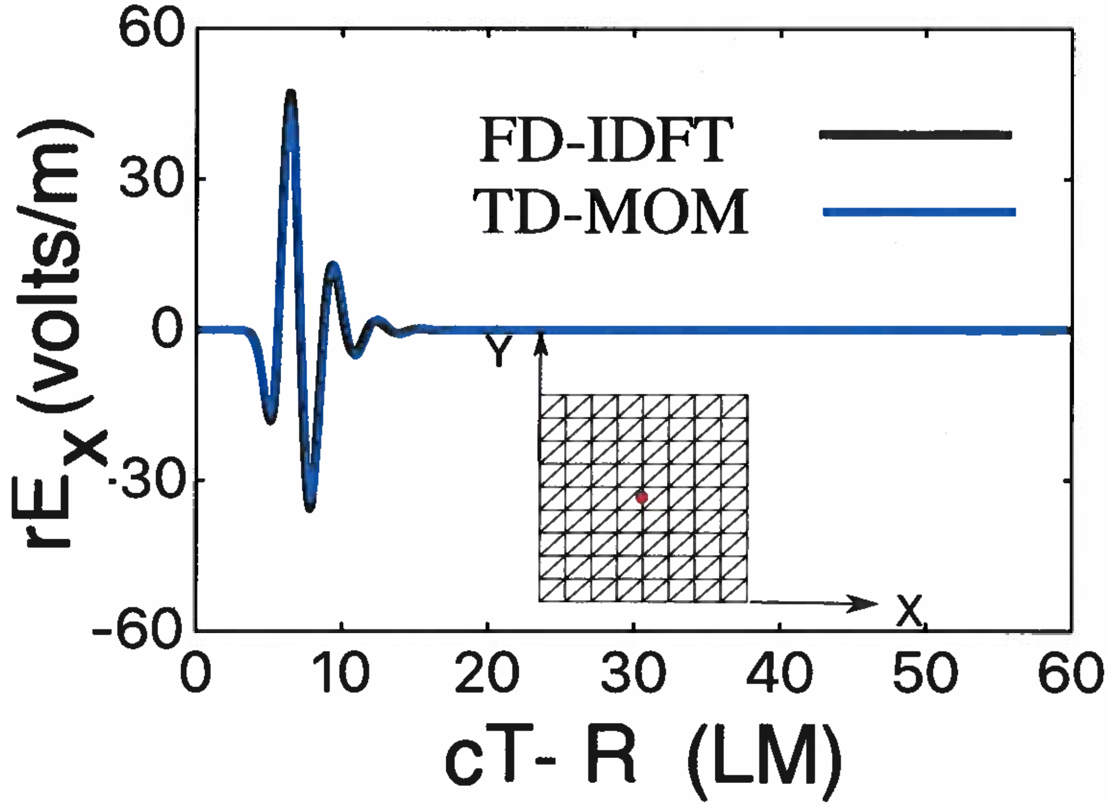

Fig. 6 — X-component of the scattered electric field from a square plate illuminated by a Gaussian plane wave.

Next, we consider a spherical wire-cage, 1.0 m radius, located with the center of the wire cage coinciding with the coordinate center. The mesh is illuminated by a Gaussian plane wave described by Eq. 29. The induced current is obtained at the equator of the sphere, highlighted by a dot in the inset of Figure 7 using the TD solution procedure and compared with the IDFT solution. There are 559 and 60 basis functions for space and time variables, respectively, for the time domain solution. Hence the matrix size is $559 \times 60 = 33,540$. Both TD and IDFT solutions compare very well, as shown in Figure 7, and remain stable in the late time as seen in the second part of the figure spanning from 60 to 300 LM.

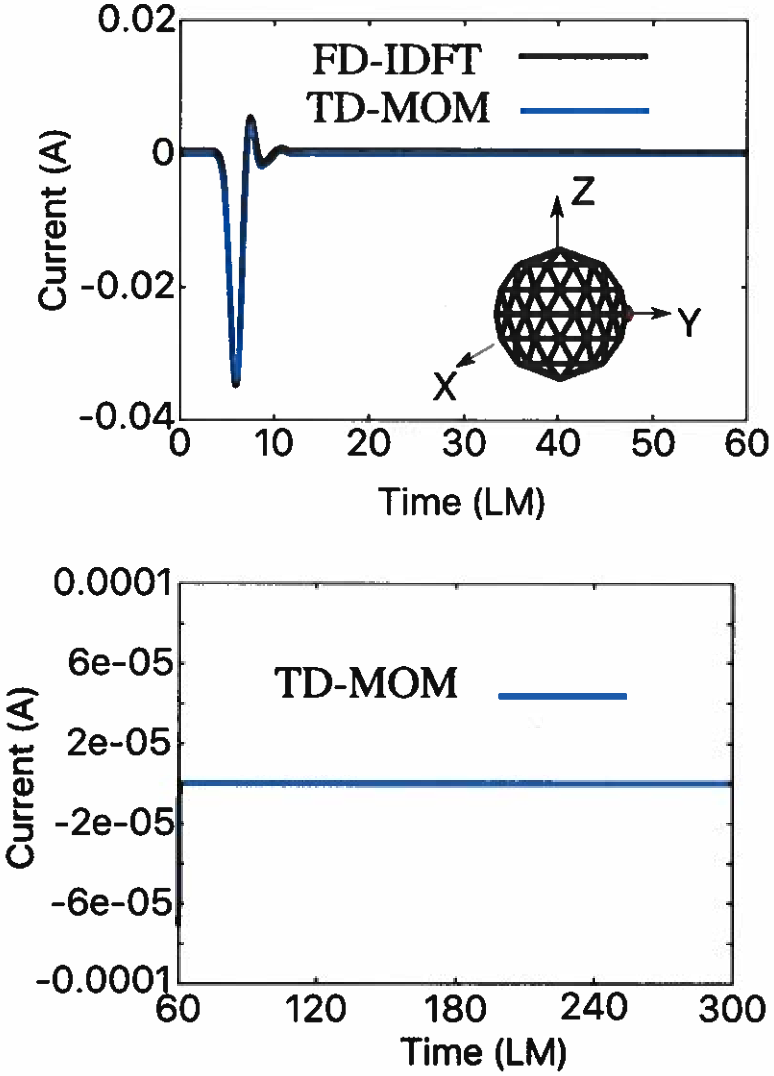

Fig. 7 — Current induced on a wire-mesh model of a sphere illuminated by a Gaussian plane wave. The wire radius=0.001 m

The x-component of the scattered electric far-field is shown in Figure 8 and compared with the IDFT solution. The scattered far-field is obtained in the back-scattered direction, *i.e.* along the a_z-axis. Again, we note good comparison in the two solutions.

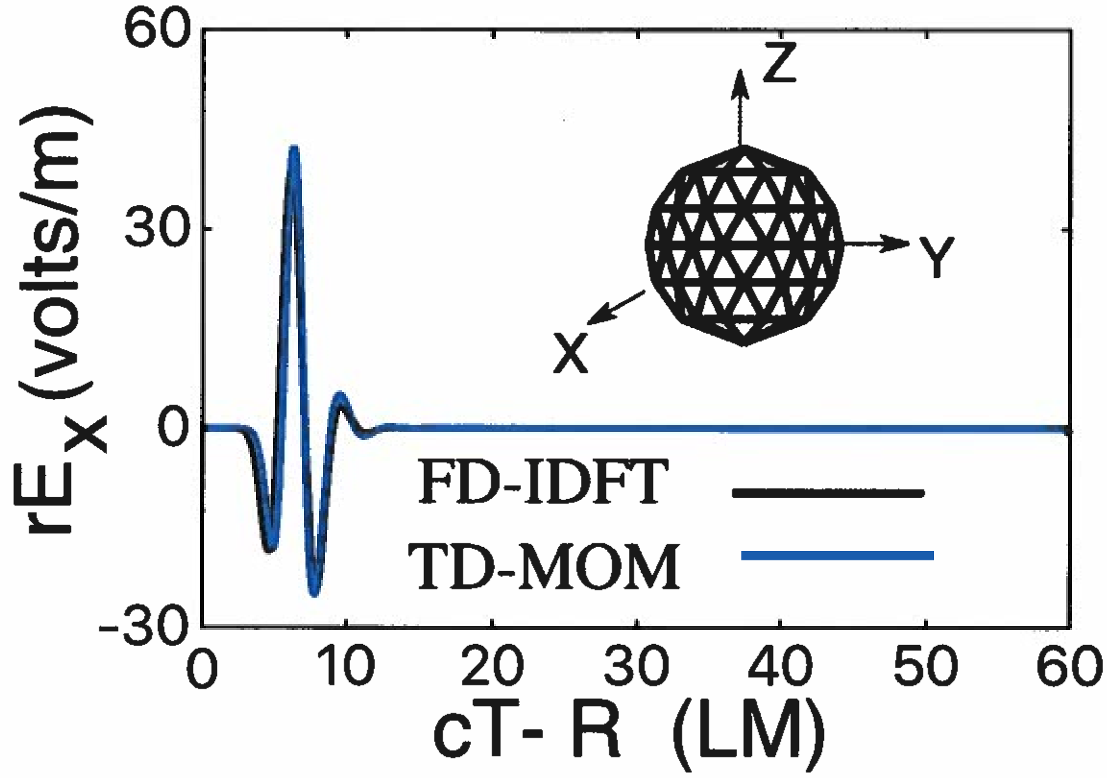

Fig. 8 — X-component of the scattered electric field from a sphere illuminated by a Gaussian plane wave.

As a fourth example, we consider a cubical wire-cage, 1.0 m on a side. The mesh is illuminated by a Gaussian plane wave described by Eq. 29. The induced current is obtained at the center of the top plate using the TD solution procedure and compared with the IDFT solution. There are 469 and 60 basis functions for space and time variables, respectively, for the time domain solution. Hence the matrix size is $469 \times 60 = 28,140$. Both TD and IDFT solutions compare very well, as shown in Figure 9, and remain stable in the late time as seen in the second part of the figure spanning from 60 to 300 LM.

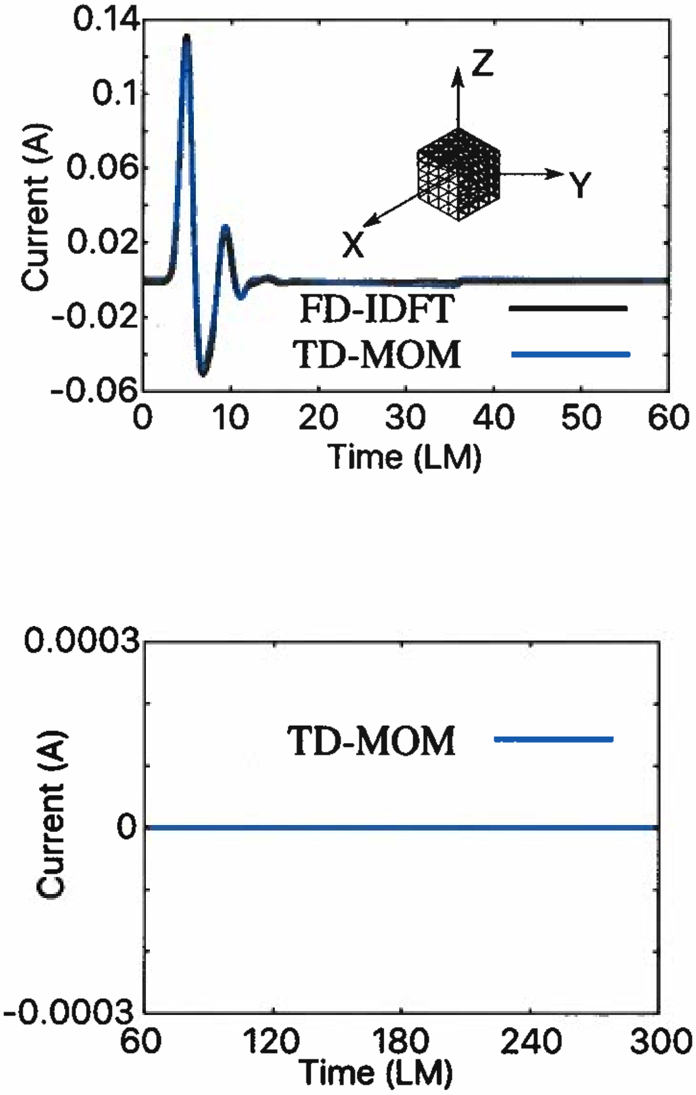

Fig. 9 — Current induced on a wire-mesh model of a cube illuminated by a Gaussian plane wave. The wire radius=0.001 m

The x-component of the scattered electric far-field is shown in Figure 10 and compared with the IDFT solution. The scattered far-field is obtained in the back-scattered direction, *i.e.* along the a_z-direction. Again, we note good comparison in the two solutions. The apparent discrepancy in the two graphs can be attributed to the fact that the FD solution did not have a data point at the peak.

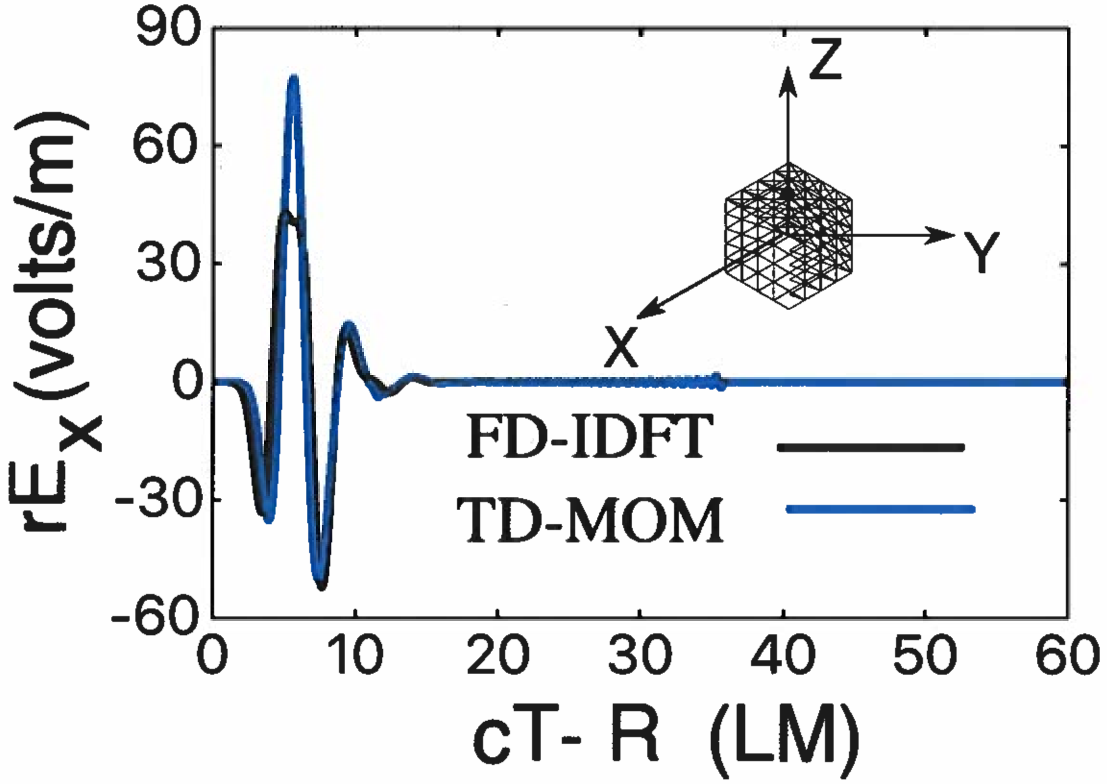

Fig. 10 — X-component of the scattered electric field from a conducting cube iluminated by a Gaussian plane wave.

As a final example, consider an aircraft-like object, shown in Figure 11, illuminated by the incident Gaussian pulse plane wave described by Eq. 29. The object is symmetrically placed in the XY-plane such that the center of the lower-side (belly) approximately coincides with the coordinate origin. The object dimensions for this example are: 2.5 m, 2.2 m, and 0.6 m along the X, Y, and Z axes, respectively. There are 1700 and 30 basis functions for space and time variables, respectively, for the time domain solution. Hence the matrix size for TD solution is $1700 \times 30 = 51,000$. The current is sampled at the middle of one of the edges connecting the nose to the first ring. For comparison, we also present the IDFT solution. The results obtained by TD and FD-IDFT solutions are shown in Figure 12. We note a good comparison for both solutions. Further, the TD solution remains stable in the late-time as shown in the second part of the figure. The small discrepancies in the two results can be attributed to insufficient number of spatial unknowns required to model a large body such as an aircraft.

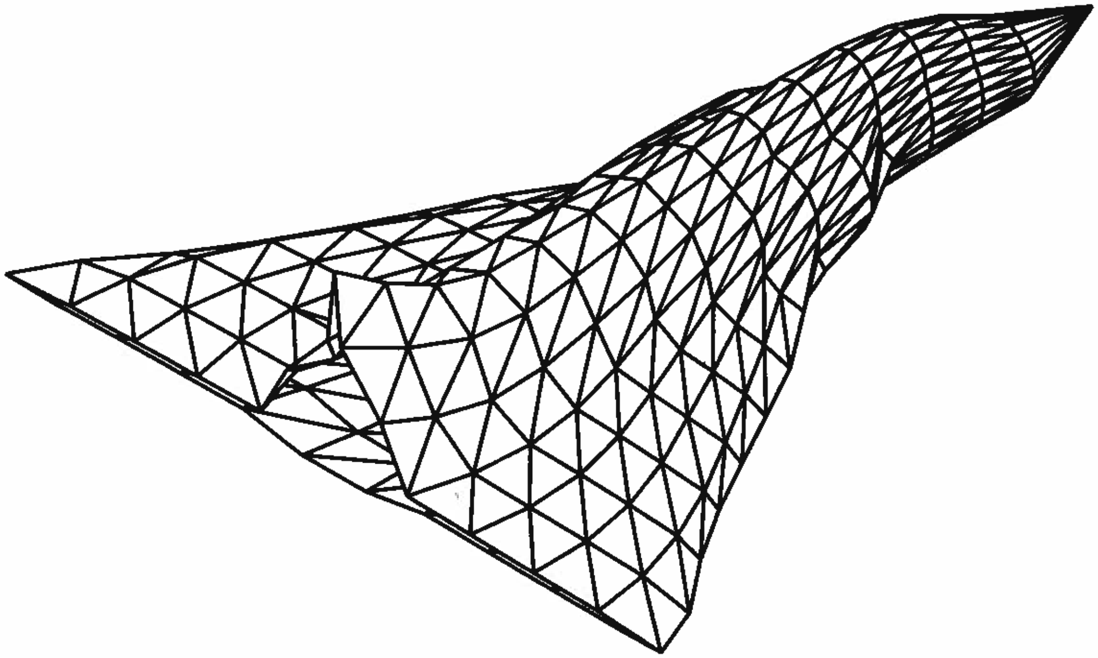

Fig. 11 — An aircraft-like object modeled by wire-grid.

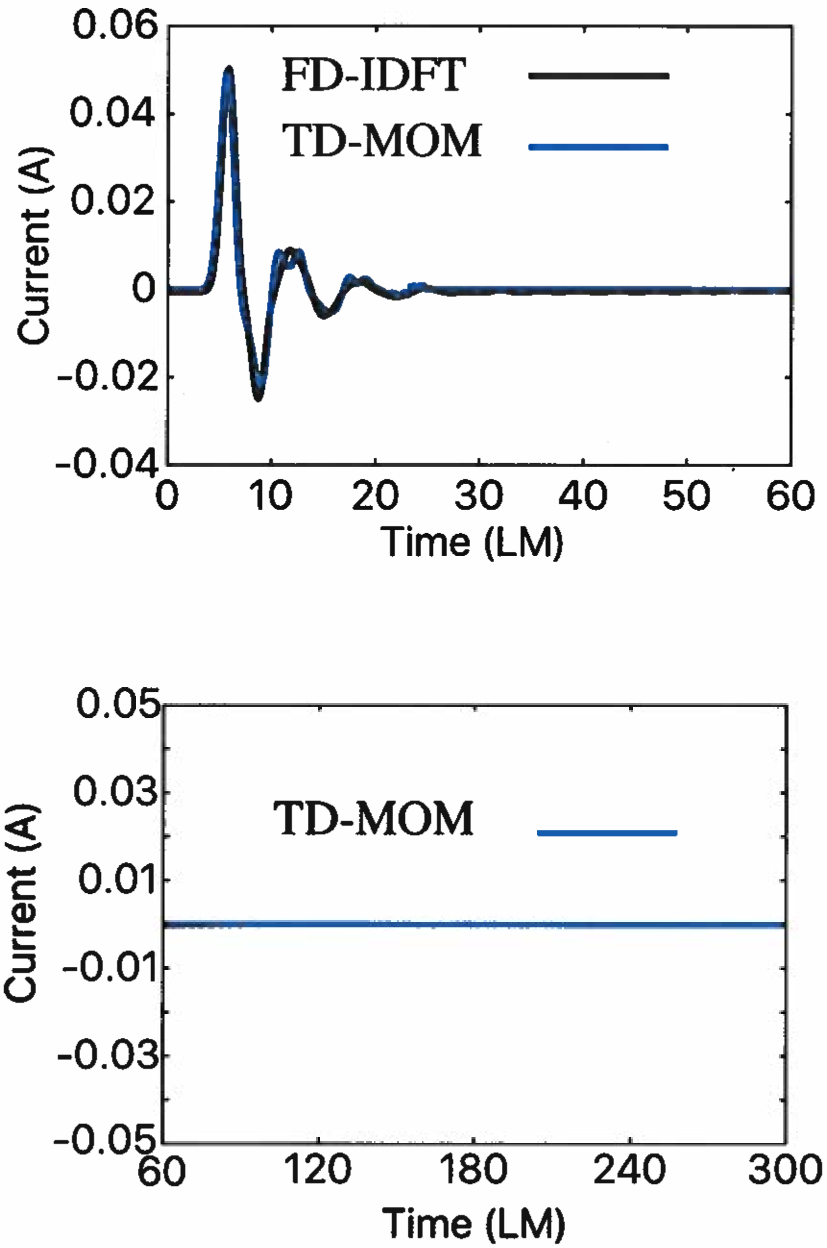

Fig. 12 — Current induced on a wire-mesh model of an aircraft-like object illuminated by a Gaussian plane wave. The wire radius=0.001 m.

2.5 Conclusion

In this chapter, a stable time-domain procedure is presented to calculate the currents induced and far-fields on a perfect electric conducting object via wire-grid modeling and method of moments. The novelty of the present solution scheme is the simplicity and capability to handle multiple incident fields with ease. We use entire domain, time-shifted Gaussian functions to approximate the induced current variation with respect to time ensuring the elimination of late-time instabilities. Note that the MOM matrix generated in this procedure is real and sparse. Admittedly, it is a large matrix and hence the solution is not efficient. In the next chapter, we develop an improved scheme where the solution is extremely efficient.

3. WIRE-GRID MODELING OF ARBITRARY BODIES - LOWER TRIANGULAR MATRIX APPROACH

Until recently, a time-stepping process, popularly known as the Marching-on-in-Time (MOT) method [9], has been the preferred technique for solving the numerical solution of Time Domain Integral Equation (TDIE) for electromagnetic field problems. The main advantage of MOT method is that, when used as an explicit scheme, it requires no matrix inversion, a computationally intensive step in any numerical algorithm [9]. Unfortunately, the MOT procedure is prone to late-time instabilities. The primary source of instability seems to be the method itself where the accumulation of error occurs at each time step. Even the implicit schemes in time domain, which require a matrix inversion, are vulnerable to the instability problem and hence are of little use to a practicing engineer.

In the previous chapter, a new type of algorithm was developed and applied to wire-grid models of arbitrary bodies to solve the time domain integral equation (TDIE) using the conventional method of moments (MOM) solution procedure. In the MOM numerical solution scheme, the arbitrary wire was divided into subdomains and the standard pulse functions were used to represent the space variable along the length of the wire. The time variable is approximated by a set of time-shifted Gaussian functions. Note that the time-shifted Gaussian functions represent entire domain functions and decay as time extends to infinity. As a result, the time domain signature stays stable even at a late time. For testing purposes, point matching was used for both the space and time variables. Because of the conventional MOM procedure, the new method can handle multiple incident pulses, with varying frequency signature bands and directions of incidence, necessary for monostatic RCS calculations, with only a fractional additional cost as compared to a single incident field. However, one disadvantage of this new procedure is the required inversion of a large real matrix of dimension $P = M \times N$, where M and N represent the number of time functions and number of wire subdomains, respectively. Thus, the matrix P could be quite large even for moderately complex wire models.

In this chapter we present an improvement which alleviates this problem, *i.e.* storage and inversion of a large matrix, by re-defining the Gaussian functions used for expressing the time variable in a controlled manner and adopting Galerkin procedure as described in the following sections. These modifications allow us to generate a block-wise lower triangular matrix, which is also block-wise Toeplitz, instead of a full matrix as in Chapter 2. Further, the block-wise Toeplitz nature of the new matrix drastically reduces the storage also. Finally, the solution is obtained by a trivial process of back substitution resulting in an extremely efficient numerical procedure.

The new procedure offers several advantages and makes the algorithm computationally efficient. First of all, the MOM matrix of dimension P is a block-wise lower triangular matrix and hence easily solvable by back-substitution avoiding expensive matrix-inversion. Next, the lower triangular matrix is also a block Toeplitz matrix with each block of dimension N. Thus, we need to compute only $P \times N$ elements compared to P^2 elements as in Chapter 2. Since the matrix inversion step is eliminated, the new algorithm is very efficient and remains stable for very long solution times. The most important point to be noted regarding the work presented in Chapter 2, and work presented in this chapter, is that the central idea is a departure from the time-marching methods of the previous 50 years. It should be noted that the problem is solved by developing a matrix equation over a fixed time interval and space domain utilizing the standard method of moments (MOM). Obviously, we have a lot of freedom in selecting basis and testing functions for the MOM solution which eventually dictates the structure of the MOM matrix and accuracy of the solution. The final matrix equation can be solved in any suitable manner including inverting the matrix as done in Chapter 2.

Also, because of this fact, one can solve multiple right-hand sides unlike any previously available MOT methods.

In the following sections, we present detailed mathematical steps, numerical solution procedure of the improved scheme, and numerical results comparing with data obtained using the frequency domain method of moments (FD-MOM) solution plus IDFT procedure.

3.1 Mathematical Formulation

Consider an arbitrary shaped body, modeled as a wire-mesh as shown in Figure 13, illuminated by a time-domain pulse.

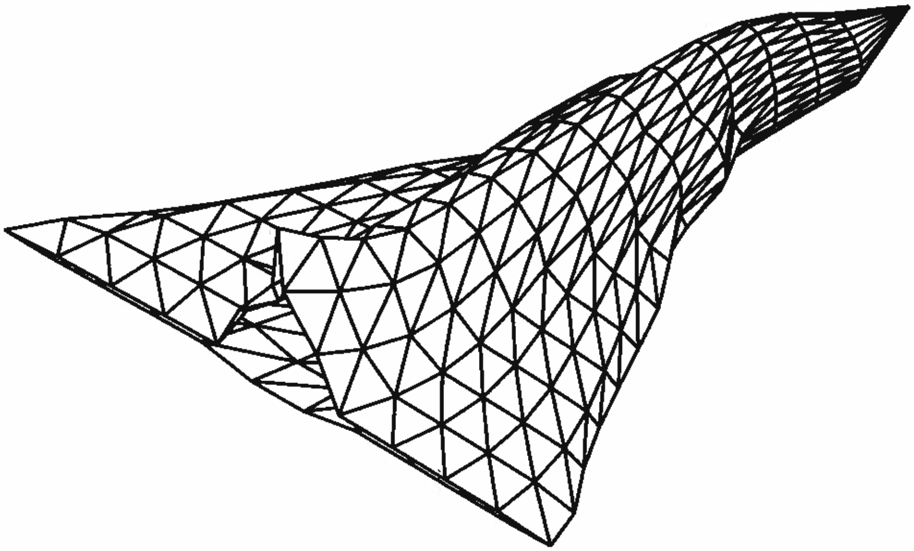

Fig. 13 — An arbitrary body modeled by wire-grid.

Following the mathematical procedure presented in Chapter 2, the time-domain integral equation (TDIE) may be written as

$$\left[\frac{\partial^2 A}{\partial t^2} + \nabla\Psi\right]_{tan} = \left[\frac{\partial E^i}{\partial t}\right]_{tan} \tag{31}$$

where

$$A(t,r) = \mu \int_\ell \frac{\hat{s}' I(t-R/c,r')}{4\pi R}\, d\ell' \tag{32}$$

$$\Psi(t,r) = \frac{-1}{\varepsilon} \int_\ell \frac{\partial I(t-R/c,r')/\partial \ell}{4\pi R}\, d\ell'. \tag{33}$$

$$\text{and } R = \sqrt{|r-r'|+a^2}. \tag{34}$$

In Eqs. (31) - (34),

$\hat{s}$ → Unit vector along the wire axis.
I → Induced current.
r → Observation point on the body.
r' → Source point on the body.
E^i → Incident electric field.
μ → permeability of the surrounding space.
ε → permittivity of the surrounding space.
a → radius of the wire.

Next, we consider the solution of Eq. (31) using the MOM.

3.2 MOM Solution Procedure

First of all, we note that the wire mesh consists of several electrically short wires, referred to as wire segments, mutually attached to each other to approximate the given body. The common point where several wire-segments are attached is known as a *node*. If only one segment is attached to a node, then that node is referred to as a *boundary node* and removed from the solution scheme. When only two wires are attached to a given node, the node is referred to as an *ordinary node* and one unknown is associated with this node as shown in Figure 14. Further, if more than two wire segments are attached to a given node, then we have a *junction node* and the number of unknowns associated with this junction node is one less than the total number of wires connected to this node. We note that the junction node can be easily handled in an identical manner as an ordinary node as presented in Chapter 2.

Let us consider an ordinary node as shown in Figure 14. Let the position vector r_n, defined with respect to the global coordinate origin ○, represent the n^{th} node. Two-wire segments, $S_n^{\pm}$, with radii $a_n^{\pm}$, are connected to this node and the induced current is arbitrarily chosen as flowing from S_n^- to S_n^+.

Next, for numerical purposes, let us define the upper limit on the time variable $t = T$, where T represents the time when the incident pulse becomes negligible. Then, we divide the time axis $0 \to T$ into M uniform time intervals given by Δt and denote $t_m = m\Delta t$ for $m = 1, 2, \ldots. M$. We note that, initially, the MOM scheme is applied to a finite interval $0 \to T$. We also note that extending the time interval to later times is trivial as discussed later.

Now, we define the approximation to the induced current $I(t,r)$ as

$$I(t,r) \approx \sum_{m=1}^{M} \sum_{n=1}^{N} I_{m,n}\, f_m(t)\, g_n(r) \tag{35}$$

where

$$f_m(t) \equiv e^{-\left(\frac{t-m\Delta t}{\sigma}\right)^2} \qquad 0 < t < \infty \tag{36}$$

and

$$g_n(r) \equiv \begin{cases} 1 & r \in (r_{n-\frac{1}{2}}, r_{n+\frac{1}{2}}) \\ 0 & \text{otherwise.} \end{cases} \tag{37}$$

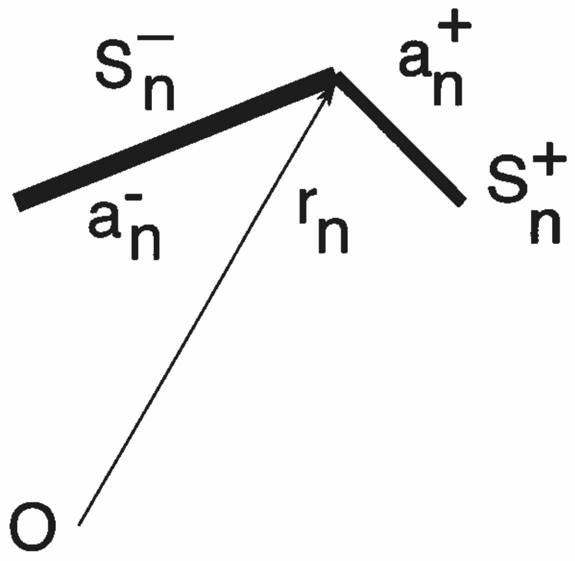

Fig. 14 — Wire segments connected to an ordinary node.

In Eqs. (36) and (37) σ, represents the standard deviation of the Gaussian function and $r_{n\pm\frac{1}{2}}$ represent the midpoint of segment $S_n^\pm$. Here, we note that the choice of σ is critical to obtain a block-wise Toeplitz moment matrix as discussed later.

Thus, for a complex body approximated by a wire mesh, we have N space basis functions including basis functions associated with junction nodes, M time functions, and $P = M \times N$ unknowns in the MOM scheme. The induced current is calculated for each unknown by solving Eq. (31) as described in the following:

Considering the Galerkin testing procedure, we use the functions defined in Eq. (36) for time variable and Eq. (37) for space variables, respectively. Defining

$$< f_m(t)g_n(r)\hat{s}, f_p(t)g_q(r')\hat{s}' > \; = \; \int_t \int_\ell f_m(t) f_p(t) g_n(r) g_q(r')\, \hat{s}\cdot\hat{s}' \; d\ell \, dt \qquad (38)$$

we can write Eq. (31) after testing as

$$< f_m(t)g_n(r)\hat{s}, \left[\frac{\partial^2 A}{\partial t^2} + \nabla\Psi\right] > \; = \; < f_m(t)g_n(r)\hat{s}, \left[\frac{\partial E^i}{\partial t}\right] > \qquad (39)$$

for $m = 1, 2, \cdots M$ and $n = 1, 2, \cdots N$.

Considering the integration on space variable, we can rewrite Eq. (39) as,

$$\begin{aligned} \ell_n \int_t f_m(t) \left[\frac{\partial^2 A(t, r_n, r')}{\partial t^2} \cdot \hat{s}_n\right] dt \; &+ \; \int_t f_m(t) \left[\Psi(t, r_{n-\frac{1}{2}}, r') - \Psi(t, r_{n+\frac{1}{2}}, r')\right] dt \\ &= \; \ell_n \int_t f_m(t) \left[\frac{\partial E^i(t, r_n)}{\partial t} \cdot \hat{s}_n\right] dt \qquad (40) \end{aligned}$$

where $\hat{s}_n$ and ℓ_n represent the unit tangential vector at $r = r_n$ and length of the n^{th}-wire segment, respectively [9].

Next, the integration on the time variable is carried out in the following manner:

- Divide the interval $0 \to T$ into K uniform time intervals given by Δt_k and denote $t_k = (k-1)\Delta t_k + 0.5\Delta t_k$ for $k = 0, 1, 2, ...K$. Note that, in general, $\Delta t_k \neq \Delta t$ which also implies that $K \neq M$. However, for simplicity, we may choose them to be same.
- Applying the numerical integration on time variable and using finite difference approximation, we can re-write Eq. (40), as

$$\begin{aligned}
&\frac{\ell_n}{\Delta t_k}\sum_{k=1}^{K} f_m(t_k)\,\left[A(t_k,r_n,r')\cdot\hat{s}_n\right] - \frac{2\ell_n}{\Delta t_k}\sum_{k=1}^{K} f_m(t_k)\,\left[A(t_{k-1},r_n,r')\cdot\hat{s}_n\right] \\
&+\frac{\ell_n}{\Delta t_k}\sum_{k=1}^{K} f_m(t_k)\,\left[A(t_{k-2},r_n,r')\cdot\hat{s}_n\right] + \sum_{k=1}^{K} f_m(t_k)\,\Psi(t_k,r_{n-\frac{1}{2}},r')\Delta t_k \\
&-\sum_{k=1}^{K} f_m(t_k)\,\Psi(t_k,r_{n+\frac{1}{2}},r')\Delta t_k = \ell_n\sum_{k=1}^{K} f_m(t_k)\,\left[\frac{\partial E^i(t_k,r_n)}{\partial t}\cdot\hat{s}_n\right]\,\Delta t_k
\end{aligned} \tag{41}$$

Considering the expansion procedure next, we have

$$A(t_k,r_n,r') = \mu\sum_{i=1}^{M}\sum_{j=1}^{N} I_{i,j}\,f_i(t_k - \frac{R_{n,j}}{c})\,\hat{s}_j\,\kappa_{n,j} \tag{42}$$

for $k = 1, 2, \cdots, K$, where

$$\kappa_{n,j} \;=\; \int_{\ell_j}\frac{d\ell'}{4\pi\,R_n}, \tag{43}$$

$R_n = |r_n - r'|$, $R_{n,j} = |r_n - r_j|$, and $\hat{s}_j$ is the unit tangential vector at $\ell = \ell_j$.

Next, let us consider the evaluation of $\Psi(t_k, r_n, r')$. Considering Eq. (33), replacing the derivative operation with finite difference approximation, and substituting Eq. (35), we have

$$\Psi(t_k,r_n,r') = \frac{-1}{\varepsilon}\sum_{i=1}^{M}\sum_{j=1}^{N} I_{i,j}\,\frac{1}{|\ell_{j+\frac{1}{2}} - \ell_{j-\frac{1}{2}}|}\left[f_i(\tau_{k,n,j+\frac{1}{2}})\,\kappa_{n,j+\frac{1}{2}} - f_i(\tau_{k,n,j-\frac{1}{2}})\,\kappa_{n,j-\frac{1}{2}}\right] \tag{44}$$

for $k = 1, 2, \cdots, K$ where

$$\kappa_{n,j\pm\frac{1}{2}} \;=\; \int_{\ell_{j\pm\frac{1}{2}}}\frac{d\ell'}{4\pi\,R_{n,j\pm\frac{1}{2}}}, \tag{45}$$

$$R_{n,j\pm\frac{1}{2}} \;=\; |r_n - r_{j\pm\frac{1}{2}}| \tag{46}$$

$$\tau_{k,n,j\pm\frac{1}{2}} \;=\; t_k - \frac{R_{n,j\pm\frac{1}{2}}}{c} \tag{47}$$

Using the expansion and testing procedures described so far, it is trivial to generate a matrix equation $ZX = Y$ of dimension $P = M \times N$. The elements of Z-matrix are formed by using Eqs. (41), (42), and (44). Note that $Z_{p,q}$ represents a matrix element of the Z-matrix, where

$$p = (m-1)N + n, \quad q = (i-1)N + j, \quad m, i = 1, 2, \cdots, M, \text{ and } n, j = 1, 2, \cdots, N.$$

Thus, we have

$$\begin{aligned}
Z_{p,q} \;=\;& \frac{\mu \ell_n}{\Delta t_k} \left[\hat{s}_n \cdot \hat{s}_j \; \kappa_{n,j}\right] \sum_{k=1}^{K} f_m(t_k) \left[f_i(\tau_{k,n,j}) - 2 f_i(\tau_{k-1,n,j}) + f_i(\tau_{k-2,n,j})\right] \\
+\;& \frac{\Delta t_k}{\varepsilon |\ell_{j+\frac{1}{2}} - \ell_{j-\frac{1}{2}}|} \sum_{k=1}^{K} f_m(t_k) f_i(\tau_{k,n+\frac{1}{2},j+\frac{1}{2}}) \; \kappa_{n+\frac{1}{2},j+\frac{1}{2}} \\
-\;& \frac{\Delta t_k}{\varepsilon |\ell_{j+\frac{1}{2}} - \ell_{j-\frac{1}{2}}|} \sum_{k=1}^{K} f_m(t_k) f_i(\tau_{k,n-\frac{1}{2},j+\frac{1}{2}}) \; \kappa_{n-\frac{1}{2},j+\frac{1}{2}} \\
-\;& \frac{\Delta t_k}{\varepsilon |\ell_{j+\frac{1}{2}} - \ell_{j-\frac{1}{2}}|} \sum_{k=1}^{K} f_m(t_k) f_i(\tau_{k,n+\frac{1}{2},j-\frac{1}{2}}) \; \kappa_{n+\frac{1}{2},j-\frac{1}{2}} \\
+\;& \frac{\Delta t_k}{\varepsilon |\ell_{j+\frac{1}{2}} - \ell_{j-\frac{1}{2}}|} \sum_{k=1}^{K} f_m(t_k) f_i(\tau_{k,n-\frac{1}{2},j-\frac{1}{2}}) \; \kappa_{n-\frac{1}{2},j-\frac{1}{2}}
\end{aligned} \tag{48}$$

The right hand side Y involves the incident field terms, given by

$$Y = [Y_1, Y_2, Y_3, \cdots, Y_M]^T, \tag{49}$$

where each $Y_m, m = 1, 2, \cdots M$ is a column vector of dimension N and the elements are given by

$$(Y_n)_m = \ell_n \sum_{k=1}^{K} f_m(t_k) \left[\frac{\partial E^i(t_k, r_n)}{\partial t} \cdot \hat{s}_n\right] \Delta t_k \tag{50}$$

At this stage, we note that multiple incident pulses with varying frequency content can be easily accommodated by adding more column blocks to the Y-matrix.

As mentioned earlier, the choice of σ, defined in Eqs. (36) is important for the generation of a block Toeplitz matrix. Considering Eq. (36) and with the choice of $\sigma = \frac{\Delta t}{6}$, we observe that the m^{th}-Gaussian function is essentially nonzero only in the interval $t = (m-1)\Delta t$ to $t = (m+1)\Delta t$. Here, we note the following:

- Because of the nature of the retarded kernel, the matrix generated is a lower triangular matrix given by

$$Z = \begin{bmatrix} Z_{1,1} & O & O & \cdots & O \\ Z_{2,1} & Z_{2,2} & O & \cdots & O \\ Z_{3,1} & Z_{3,2} & Z_{3,3} & \cdots & O \\ \vdots & \vdots & \vdots & \vdots & \vdots \\ Z_{M,1} & Z_{M,2} & Z_{M,3} & \cdots & Z_{M,M} \end{bmatrix}, \tag{51}$$

where each $Z_{m,i}$, $m = 1,2,\cdots M$ and $i = 1,2,\cdots,M$ is a matrix of dimension N representing the mutual interaction between the spatial basis functions for a given pair of testing time function m and and source time function i.

- Referring to Eq. (48), we note that for $i > m$, the matrix blocks are zero. This is because, for time functions $f_m(t_k)$ and $f_i(\tau_{k,n,j})$, the time intervals do not overlap resulting in zero value of the product.
- We further note that all the diagonal blocks are the same and all off-diagonal blocks are given by $Z_{m,i} = Z_{|m-i|+1,1}$.
- Because of the Toeplitz nature, only the blocks in the first column of Eq. (51) need to be computed and stored. All other blocks can be generated from the first column as needed.
- Because of the lower-triangular nature of the matrix, the solution can be obtained in a trivial manner. To obtain the solution, we need to invert and store the first block $Z_{1,1}$. However, this needs to be done only once.

Further, the response to next M time steps, *i.e.* from $T \rightarrow 2T$ can be easily obtained by only modifying the right hand side. We note that for this case, the right hand side would be $Y - \overline{Z}X_{pre}$ where X_{pre} represents the coefficients already calculated for zero to M-steps and $\overline{Z}$ represents the matrix containing vector and scalar potential terms contributing to zero to M time steps. The $\overline{Z}$-matrix is also Toeplitz and can be obtained in the same manner as Z-matrix. Also note that the $\overline{Z}$-matrix need not be inverted and may be stored if several M-time steps are needed.

3.3 Numerical Results

In this section, we present numerical results for several conducting objects modeled by wire-grid with wire radius set equal to 0.001m. Further, for all examples, the incident field is given by

$$E^i(t,r) = E_o \frac{4}{T_P\sqrt{\pi}} e^{-\gamma^2} \tag{52}$$

where

$$\gamma = \frac{4}{T_P}(ct - ct_o - r \cdot a_k). \tag{53}$$

In Eqs. (52) and (53), a_k is the unit vector in the direction of propagation of the incident wave, T_P is the pulse width of the Gaussian impulse, $E_o \cdot a_k = 0$, r is a position vector relative to the origin, c is the velocity of propagation in the external medium, and t_o is a time delay which represents the time at which the pulse peaks at the origin. Also, we have $E_o = 120\pi a_x$, $ct_0 = 6.0$ LM, $T - P = 4.0$ LM, and $k = -a_z$. Note that 1 LM = 3.333 nSecs. Further, for all examples, we have $T = 2 * ct_0 = 12$ LM, by which time the incident pulse drops to negligible value. Lastly, we note that the number of time basis functions depend on the maximum frequency content of the incident pulse and 30-60 time-shifted Gaussian functions are required for the given incident field to generate reasonable accuracy in the time-domain solution.

Initially, we consider the same examples presented in Chapter 2 for comparison purposes and also to show that the present method is more efficient. The time history is restricted to 30 *LM* in each case to obtain proper measure of the efficiency.

As a first example, consider three straight wires, each 2.0 m long, placed along the x, y, and z axes and joined at the origin, as shown in Figure 15. Each wire is divided into 10 segments and the wire-junction is illuminated by a Gaussian plane wave described by Eq. (52). The induced current at the center of the wire placed along the x-axis is obtained using the present procedure and shown in Figure 15. The result is compared with the method presented in Chapter 2. There are 30 basis functions for space and time variables, respectively, for the time domain solution. The CPU times for this problem is: 0.024 seconds for the present method and 3.964 seconds for the solution presented in Chapter 2.

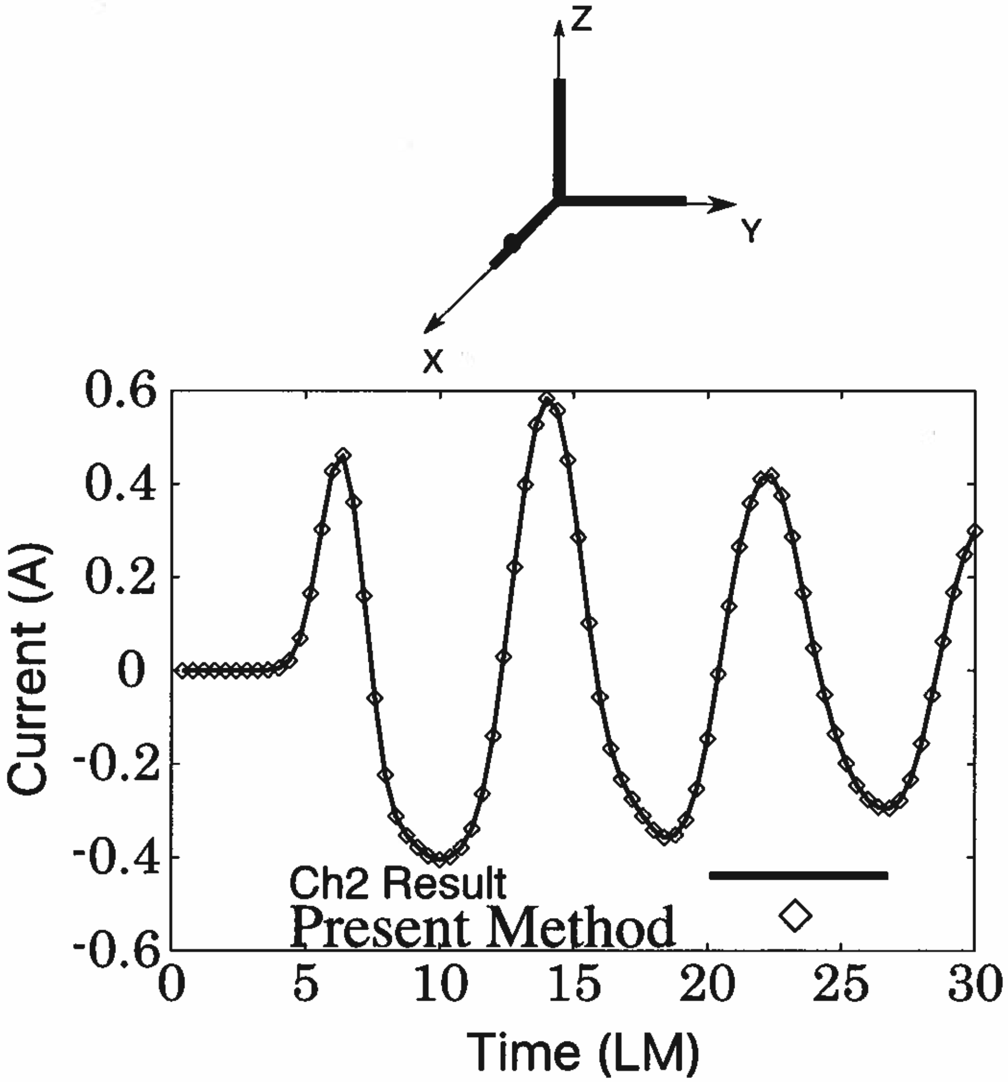

Fig. 15 — Current induced on a 3-wire structure illuminated by a Gaussian plane wave. The wire radius=0.001 m

Next, consider a wire-mesh arranged in the shape of a square plate of 1.0 × 1.0 m, located in the XY-plane. The mesh is illuminated by a Gaussian plane wave described by Eq. (52). The induced current at the center of the mesh, highlighted by a dot in the inset of Figure 16, is obtained using the new procedure and compared with the method presented in Chapter 2. There are 377 and 30 basis functions for space and time variables, respectively, for both time domain solutions. Both TD solutions compare very well, as shown in Figure 16. The CPU times for this problem is: 7.452 seconds for the present method and 2,126.2 seconds for the solution presented in Chapter 2.

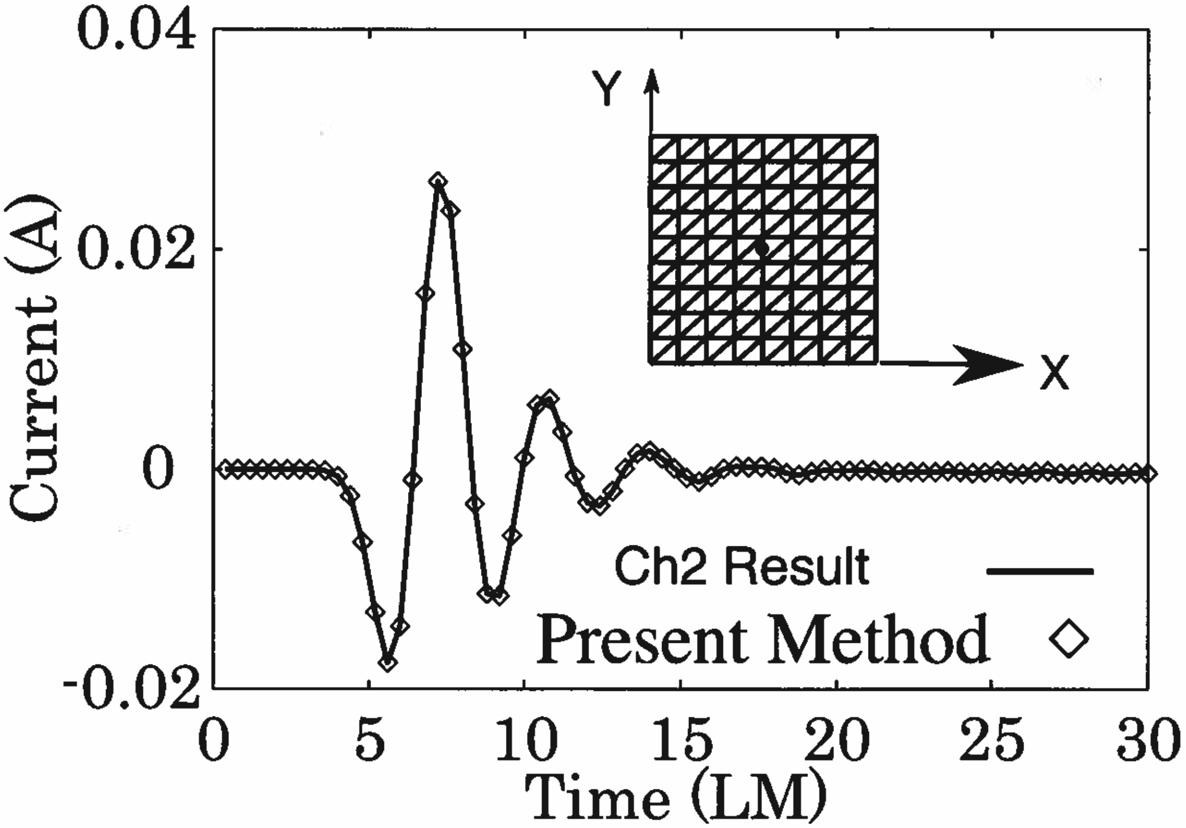

Fig. 16 — Current induced on a wire-mesh model of a square plate illuminated by a Gaussian plane wave. The wire radius=0.001 m

Next, we consider a spherical wire-cage, 1.0 m radius, located with the center of the wire cage coinciding with the coordinate center. The mesh is illuminated by a Gaussian plane wave described by Eq. (52). The induced current is obtained at the equator of the sphere, highlighted by a dot in the inset of Figure 17 using the TD solution procedure and compared with the solution procedure presented in Chapter 2. There are 449 and 30 basis functions for space and time variables, respectively, for both time domain solutions. Both TD solutions compare very well, as shown in Figure 17. The CPU times for this problem is: 9.68 seconds for the present method and 3,813.2 seconds for the solution presented in Chapter 2.

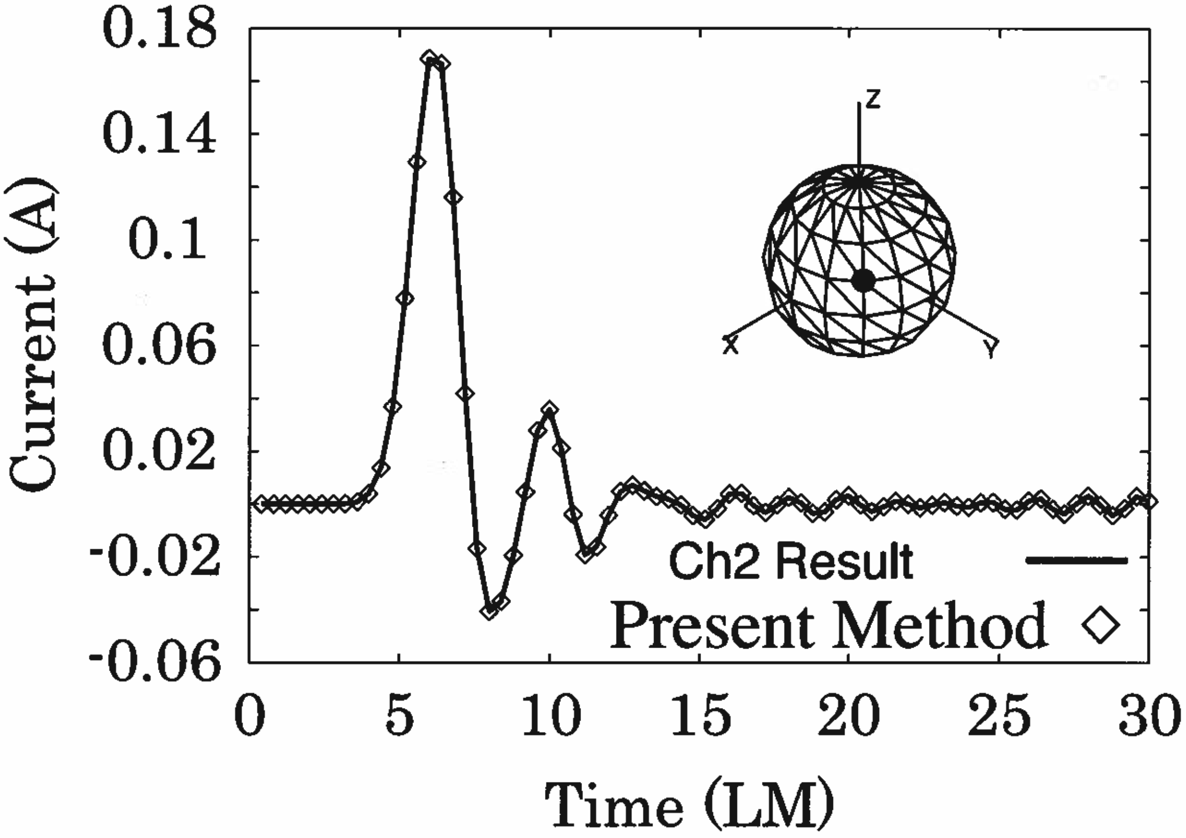

Fig. 17 — Current induced on a wire-mesh model of a sphere illuminated by a Gaussian plane wave. The wire radius=0.001 m

As a fourth example, we consider a cubical wire-cage, 1.0 m side. The mesh is illuminated by a Gaussian plane wave described by Eq. (52). The induced current is obtained at the center of the top surface using the TD solution procedures of Chapter 2 and the present procedure. There are 469 and 30 basis functions for space and time variables, respectively, for the time domain solution. The numerical results for the present method and the method presented in Chapter 2 are shown in Figure 18. The results compare very well. The CPU times for this problem is: 13.8 seconds for the present method and 4,174.2 seconds for the solution presented in Chapter 2.

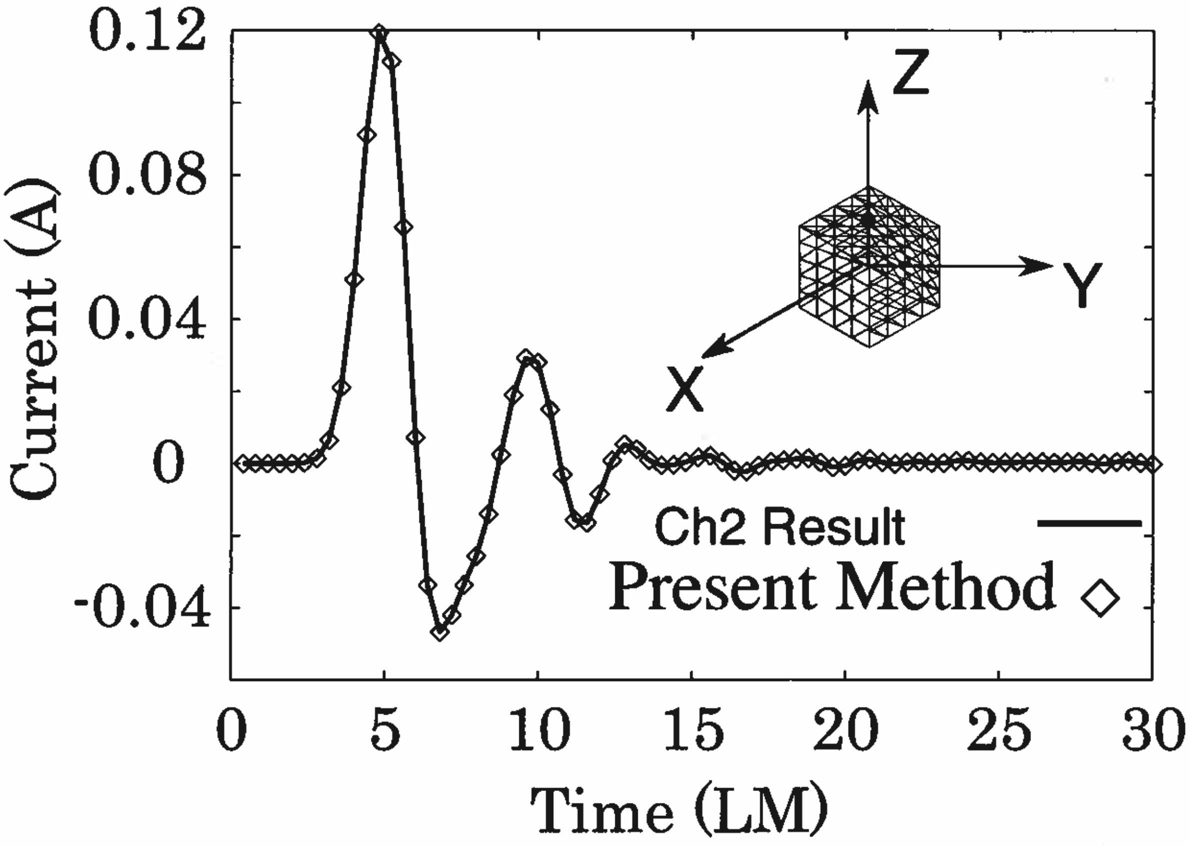

Fig. 18 — Current induced on a wire-mesh model of a cube illuminated by a Gaussian plane wave. The wire radius=0.001 m

Now, we consider a few more examples using only the present procedure and compare the results with the frequency domain solution combined with inverse discrete Fourier transform (IDFT) method.

Consider a conducting object shaped as an almond as shown in the inset of Figure 19. We note that this is an object with a low radar cross section, and hence difficult to model. The object is described mathematically as follows:

Let (s,t) represent two parametric coordinates. Then, for the upper surface, we have $-\frac{5}{12} < t < 0$, $x = Lt$, $y = 0.193333L\sqrt{1-(\frac{12t}{5})^2}\cos s$, and $z = 0.064444L\sqrt{1-(\frac{12t}{5})^2}\sin s$. For the lower surface, we have $-\frac{25}{12} < t < 0$

$$\begin{aligned} x &= Lt, \\ y &= 4.83345L\left[\sqrt{1-(\frac{12t}{25})^2}-0.96\right]\cos s, \\ \textit{and } z &= 1.61115L\left[\sqrt{1-(\frac{12t}{25})^2}-0.96\right]\sin s. \end{aligned}$$

Also, the parameter s changes from -π to π and $L = 1.4538$ m. The induced current is sampled at the center of the upper surface indicated by a dot in the figure. There are 1079 and 60 basis functions for space and time variables, respectively.The TD solution procedure is compared with the IDFT solution. The IDFT solution is obtained by solving the frequency domain MOM problem at 256 equally spaced frequency points in the 0 - 400 MHz frequency band and performing the inverse Fourier transform. We note a good comparison between the two solutions.

To illustrate the absence of late time instabilities, the magnitude of the current is plotted as a function of time using log scale and shown in the same figure. Note that the base of the logarithm is 10. We note that the current reaches a value of 10^{-300} at around 25 LM and set to zero beyond.

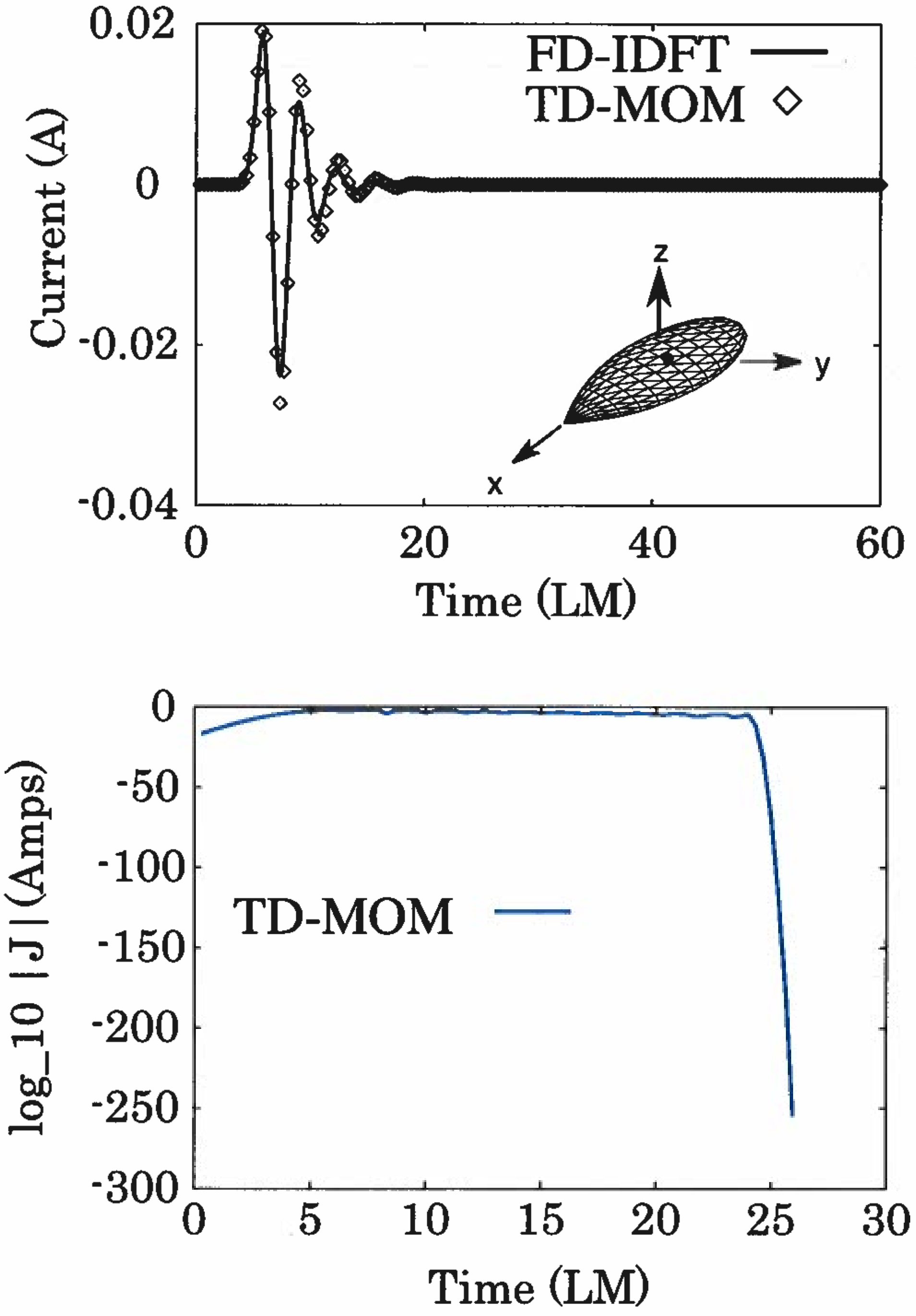

Fig. 19 — Current induced on a wire-mesh model of an almond illuminated by a Gaussian plane wave. The wire radius=0.001 m.

Next, consider a sphere of 0.5 m radius, with center coinciding with the coordinate origin, modeled by thin wires, as shown in the inset of Figure 20. This example is presented to illustrate the capability of the present method to handle multiple incident fields. The object is illuminated: a) by a Gaussian impulse as in the previous example (case 1), and b) by a similarly polarized pulse with half the pulse width (case 2). The time domain solution results are compared with the IDFT solution and presented in the Figure 20. There are 524 and 60 basis functions for space and time variables, respectively. We note good comparison for both cases.

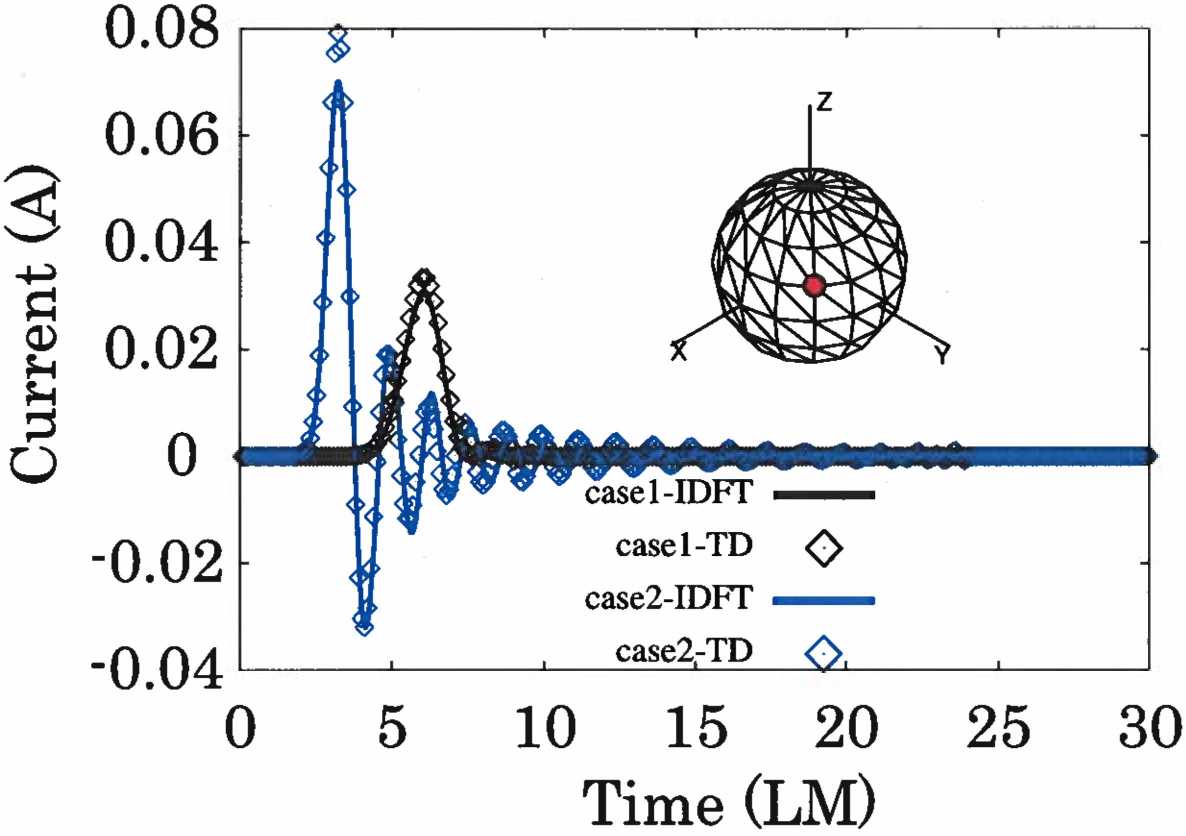

Fig. 20 — Current induced on a wire-mesh model of a sphere of 0.5 m radius illuminated by a Gaussian plane wave. The wire radius=0.001 m.

Next, we consider an aircraft-like object, as shown in Figure 13. The object is symmetrically placed in the XY-plane such that the center of the lower-side (belly) approximately coincides with the coordinate origin. The object dimensions are: 0.97 m, 0.86 m, and 0.25 m along the X, Y, and Z axes, respectively. There are 1700 and 30 basis functions for space and time variables, respectively, for the time domain solution. The current is sampled at the middle of an edge shown by a dot in the Figure 13. The IDFT solution is obtained in a similar manner as in the previous example. The results obtained by FD-IDFT, the method presented in Chapter 2, and the present method are shown in Figure 21. Although there is a good comparison for all solutions, some discrepancies are apparent. These discrepancies may be attributed to possible insufficient sampling at the higher frequencies for the IDFT solution and may be corrected by a denser grid. However, we did not attempt developing a denser grid since it involves considerable effort. The CPU times for this problem is: 452.89 seconds, 4,834.7 seconds, and 173,750 seconds for the present method, IDFT method, and the solution presented in Chapter 2, respectively. Also, as in the case of almond, the magnitude of the current is plotted as a function of time using log scale and shown in the same figure. Note that the base of the logarithm is 10. We note that the current reaches a value of 10^{-300} at around 60 LM and set to zero beyond.

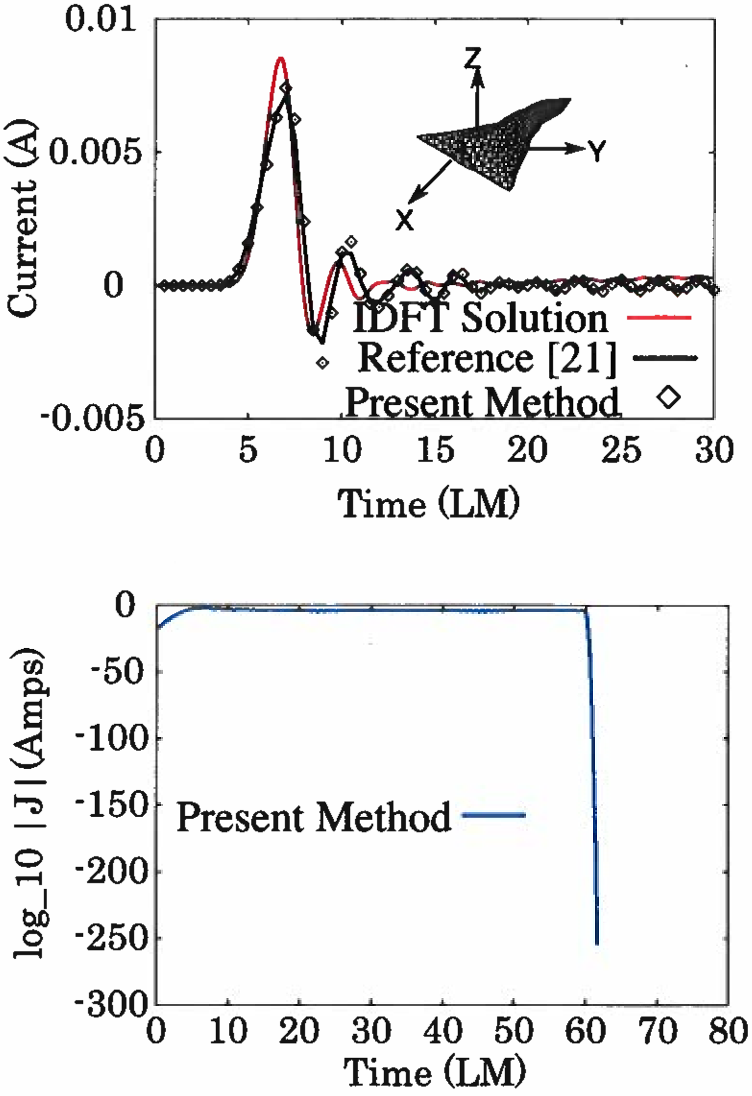

Fig. 21 — Current induced on a wire-mesh model of an aircraft-like object illuminated by a Gaussian plane wave. The wire radius=0.001 m.

Finally, we consider a ship-like object, shown in Figure 22. The ship is 5.56 m long, 0.716 m wide, and 0.387 m height and placed such that the origin is approximately coinciding with center of the top deck. There are 22,694 and 30 basis functions for space and time variables, respectively, for the time domain solution. The current is sampled at the middle of the upper-deck approximately coinciding with $x = y = 0$. The numerical results obtained by the method presented in this work is shown in Figure 23. Also, note that IDFT solution for this example is prohibitively expensive and hence not attempted.

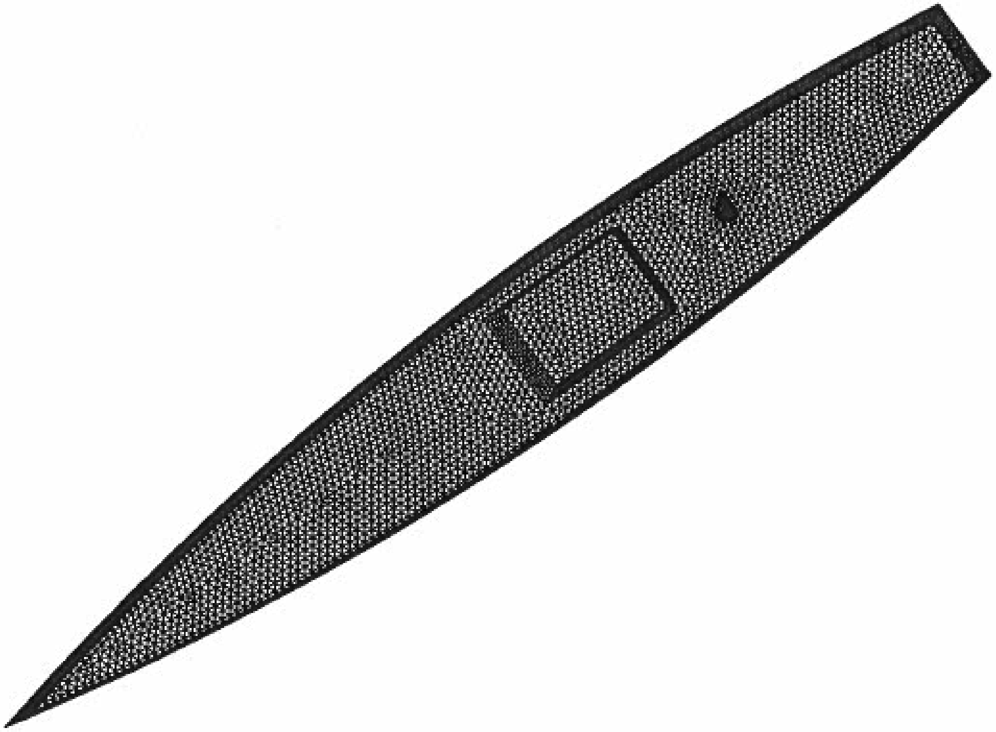

Fig. 22 — Wire-grid model of a ship-like object.

3.4 Conclusions

In this work, a stable procedure is to solve the time-domain integral equation for conducting bodies using MOM solution procedure is presented. Note that the MOM matrix generated in this procedure is lower triangular and block-wise Toeplitz. Hence, solution of this matrix is extremely efficient.

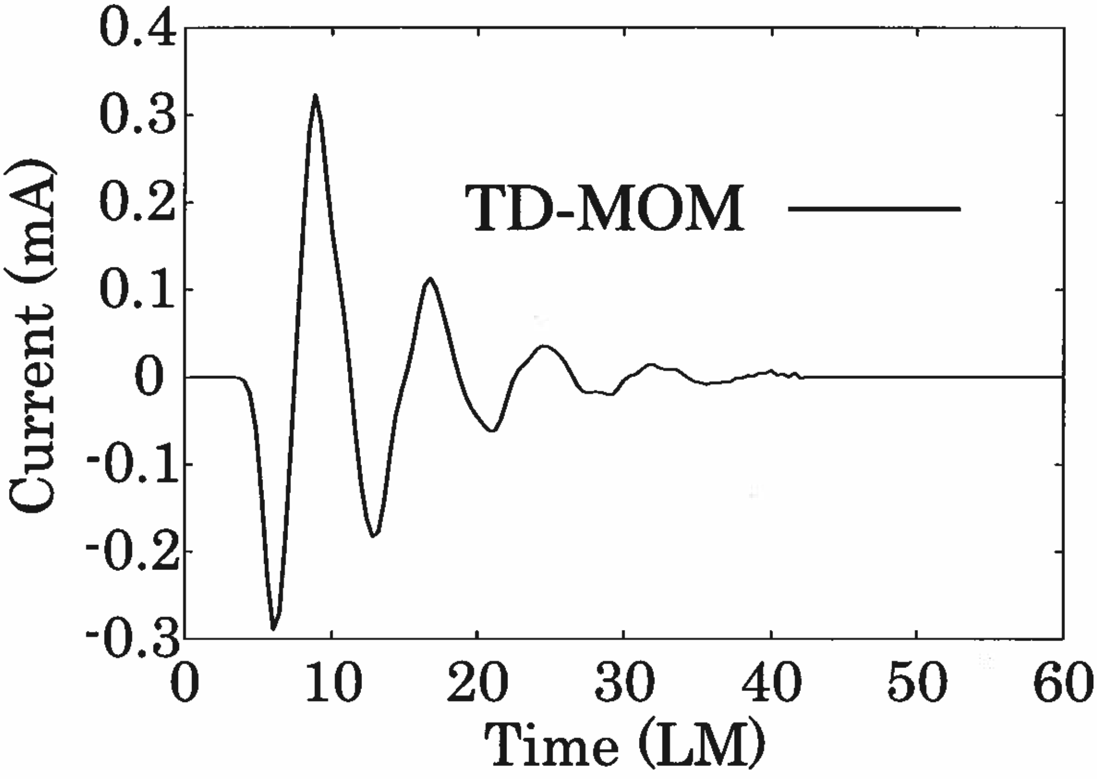

Fig. 23 — Current induced on a wire-mesh model of a ship-like object illuminated by a Gaussian plane wave. The ship is 5.56 m long, 0.716 m wide, and 0.387 m height and placed such that the origin is approximately coinciding with center of the top deck. The wire radius=0.001 m.

4. PATCH MODELING OF ARBITRARY BODIES

In this chapter, we discuss the numerical procedures to calculate the transient scattering from perfectly conducting, arbitrarily shaped, three dimensional, finite sized bodies via patch modeling approach. In the previous two chapters, we have developed the numerical procedures to solve the problem via wire-grid modeling approach. The wire-grid modeling approach has been remarkably successful in treating many problems, particularly in those requiring the prediction of far-field quantities such as radiation patterns and radar cross sections. Not only is the connectivity of a wire-grid model easily specified for computer input, but the approach also has the advantage that all numerically computed integrals in the moment matrix are one dimensional. However, the approach is not well suited for calculating near-field and surface quantities such as surface current and input impedance. Some of the problems encountered include the presence of fictitious loop currents in the solution, ill-condtioned moment matrices and incorrect currents at resonant frequencies of the scatterer, and difficulties in interpreting computed wire currents and relating them to equivalent surface currents. The accuracy of wire-grid modeling has also been questioned on theoretical grounds. Most of these difficulties can be either wholly or partially overcome by surface patch approaches and, hence, we develop numerical procedures for the solution of TDIE using the patch modeling scheme. However, the numerical procedures developed in this chapter follow similar numerical steps presented in Chapter 3.

4.1 Integral Equation Formulation

Let S denote the surface of a closed or open perfectly conducting body illuminated by a transient electromagnetic pulse as shown in Figure 24. This pulse induces a surface current, $J(r,t)$, on S which then re-radiates a scattered field. If S is open, $J(r,t)$ is regarded as the sum of the currents on the opposite sides of the surface.

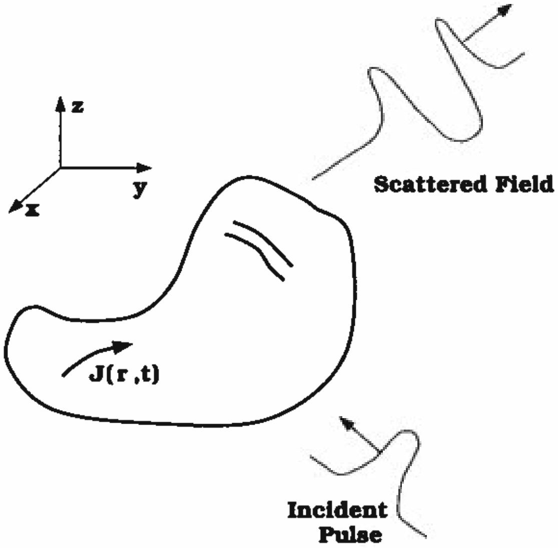

Fig. 24 — Transient pulse incident upon an arbitrarily shaped body.

The boundary conditions require that the total tangential electric field on the conducting surface be zero or

$$\left[E^s(J)+E^i\right]_{tan}=0 \qquad \text{on } S, \tag{54}$$

where $E^s(J)$ and E^i represent the scattered electric field due to the induced current J and the incident electric field, respectively. The scattered field radiated by the current J may be written in terms of the magnetic vector and electric scalar potentials as

$$E^s(J)=-\frac{\partial A}{\partial t}-\nabla\Phi \tag{55}$$

where

$$A(r,t) = \mu\int_S \frac{J(r',t-\frac{R}{c})}{4\pi R}dS', \tag{56}$$

$$\Phi(r,t) = \frac{1}{\varepsilon}\int_S \frac{q_s(r',t-\frac{R}{c})}{4\pi R}dS', \tag{57}$$

and, $R=|r-r'|$. In Eqs. (54)–(57), μ and ε are the permeability and permittivity of the surrounding medium, c is the velocity of propagation of the electromagnetic wave, r and r' are the arbitrarily located observation point and source point on the scatterer, respectively. Also, note that the incident field, E^i, is defined in the absence of the scatterer.

Upon using the continuity equation, given by

$$\nabla_s\cdot J=-\frac{\partial q_s}{\partial t}\Rightarrow q_s=-\int_{\tau=0}^{t}\nabla_s\cdot J d\tau, \tag{58}$$

we may rewrite the scalar potential term as

$$\Phi(r,t)=\frac{-1}{\varepsilon}\int_S\int_{\tau=0}^{t-R/c}\frac{\nabla\cdot J(r',\tau)}{4\pi R}dS'd\tau. \tag{59}$$

Using Eqs. (54) and (55), we may write the time domain electric field integral equation as

$$\left[\frac{\partial A(r,t)}{\partial t}+\nabla\Phi(r,t)\right]_{tan}=E^i_{tan}(r,t) \tag{60}$$

An alternate form of the TDIE may also be obtained by differentiating Eq. (60) with respect to time, given by

$$\left[\frac{\partial^2 A(r,t)}{\partial t^2}+\nabla\Psi(r,t)\right]_{tan}=\left[\frac{\partial E^i(r,t)}{\partial t}\right]_{tan} \tag{61}$$

where

$$\Psi(r,t) = \frac{-1}{\varepsilon} \int_S \frac{\nabla \cdot J(r', t - \frac{R}{c})}{4\pi R} dS'. \tag{62}$$

We remark here that, both versions *i.e.* Eqs. (60) and (61) are popular and have been used in the literature [10, 17, 18]

4.2 Numerical Solution Scheme

The first step in the numerical scheme is to describe adequately the geometry involved to the digital computer. This task is most easily accomplished by covering the body surface with planar triangles to generate a "patch model" of the actual body. We choose the planar triangular patches to model the body because they have the ability to conform to any geometrical surface or boundary. In fact, simple as well as complex bodies, can be easily modeled by planar triangular patches and can be described to the computer using automated schemes. Further, for numerical purposes, it is very easy to increase the patch density in areas where more resolution is required.

Next, we note that the triangular mesh consists of several electrically short patches, mutually attached to each other to approximate the given body. The common edge where several patches are attached is known as a *interior edge*. If only one patch is attached to an edge, then that edge is referred to as a *boundary edge* and removed from the solution scheme. When only two triangular patches are attached to a given edge, that interior edge is referred to as an *ordinary edge* and one unknown is associated with this edge. Further, if more than two triangular patches are attached to a given edge, then we have a *junction edge* and the number of unknowns associated with this junction edge is one less than the total number of patches connected to this edge.

The next task in the numerical solution procedure is to develop an algorithm to solve the integral equation (61). We accomplish this task by selecting the well-known method of moments [5] and applying the numerical procedures developed in Chapter 3 to obtain an accurate and efficient numerical method.

4.2.1 Definition of Sapce and Time Basis Functions

Assuming that the body is modeled with triangular patches, we define the basis function for any edge m common to the two triangles $T_m^{\pm}$, referring to Figure 25, given by

$$f_m(r) = \begin{cases} \frac{l_m}{2A_m^+} \rho_m^+ & \text{for } r \in T_m^+ \\ \frac{l_m}{2A_m^-} \rho_m^- & \text{for } r \in T_m^- \\ 0 & \text{otherwise} \end{cases} \tag{63}$$

In Eq. (63), l_m denotes the length of the m^{th} edge and $A_m^{\pm}$ is the area of triangle $T_m^{\pm}$. Further, an arbitrary point in T_m^+ may be located by the position vector r, relative to the origin, O, or by ρ_m^+, referenced at the free vertex of T_m^+. For an arbitrary point in T_m^-, the position vector ρ_m^- is similarly defined except that it is directed toward the free vertex of T_m^-. The "+" or "$-$" convention is determined by choosing a reference direction for positive current flow for the m^{th} edge. This current is assumed to flow from T_m^+ to T_m^-. Also, we

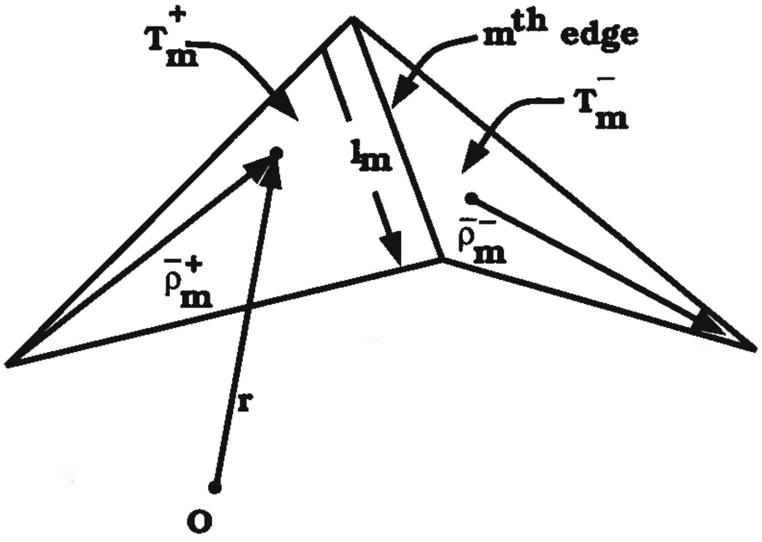

Fig. 25 — Triangle pair and geometrical parameters associated with the m^{th} interior edge.

follow the convention where superscripts refer to the faces and subscripts refer to the edges. For example, T_m^+ is the positive triangle associated with edge m.

Some advantages of expressing the current in terms of the f_m's have been noted here. For example, along the outer boundary of the triangle pair, the current has no component normal to the boundary so no line charges exist along the boundary. The current normal to the m^{th} edge, *i.e.* the edge common to T_m^+ and T_m^-, is constant and continuous across the edge. These two results imply that all of the edges of T_m^+ and T_m^- are free of line charges. This is an important consideration while developing an efficient and robust numerical procedure, since the presence of such line charges involve extra unknowns and cumbersome evaluation of singular integrals. Lastly, the surface divergence of the basis functions is given by

$$\nabla_s \cdot f_m(r) = \begin{cases} \frac{l_m}{A_m^+} & \text{for } r \in T_m^+ \\ -\frac{l_m}{A_m^-} & \text{for } r \in T_m^- \\ 0 & \text{otherwise.} \end{cases} \tag{64}$$

The surface divergence is proportional to the charge density. Therefore, the charge density is constant on each triangle, and the total charge associated with each triangle pair is zero.

Next, for numerical purposes, let us define the upper limit on the time variable $t = T$, where T represents the time when the incident pulse becomes negligible. Then, we divide the time axis $0 \rightarrow T$ into N_t uniform time intervals given by Δt and denote $t_n = n\Delta t$ for $n = 1, 2, \ldots. N_t$. We note that, initially, the MOM scheme is applied to a finite interval $0 \rightarrow T$. We also note that extending the time interval to later times is trivial as discussed in Chapter 3. Defining the basis function for time variable as,

$$g_n(t) \equiv \begin{cases} 1 - \frac{|t - t_n|}{\Delta t} & t \in (t_{n-1}, t_{n+1}) \\ 0 & \text{otherwise.} \end{cases} \tag{65}$$

we approximate the induced current $I(r,t)$ as

$$I(r,t) \approx \sum_{m=1}^{N_S} \sum_{n=1}^{N_t} I_{m,n}\, f_m(r)\, g_n(t) \tag{66}$$

where N_S and N_t represent the number of basis functions in space and time, respectively. Thus, for a complex body approximated by a triangular mesh, we have N_S space basis functions including basis functions associated with junction edges, N_t time functions, and $P = N_S \times N_t$ unknowns in the MOM scheme. The induced current is calculated for each unknown by solving Eq. (61) as described in the following:

4.2.2 *Testing Procedure*

Considering the Galerkin testing procedure, we use the functions defined in Eq. (63) for space variable and Eq. (65) for time variables, respectively. Defining

$$< f_m(r) g_n(t), f_p(r') g_q(t) > \; = \; \int_S \int_t f_m(r) \cdot f_p(r') \;\; g_n(t) g_q(t)\, dS\, dt \tag{67}$$

we can write Eq. (61) after testing as

$$< f_m(r) g_n(t), \left[\frac{\partial^2 A}{\partial t^2} + \nabla \Psi \right] > \; = \; < f_m(r) g_n(t), \left[\frac{\partial E^i}{\partial t} \right] > \tag{68}$$

for $m = 1, 2, \cdots N_S$ and $n = 1, 2, \cdots N_t$. Further, we can rewrite Eq. (68) as,

$$\begin{aligned} \int_t g_n(t)\, \frac{\partial^2}{\partial t^2} \int_S \left[A(r,r',t) \cdot f_m dS \right] dt \;&+\; \int_t g_n(t) \int_S \left[\nabla \Psi(r,r',t) \cdot f_m\, dS \right] dt \\ &= \int_t g_n(t) \int_S \left[\frac{\partial E^i(r),t}{\partial t} \cdot f_m\, dS \right] dt \end{aligned} \tag{69}$$

Now, let us consider the testing procedure on the time variable. Using the well-known integration by parts scheme on the first integral of Eq. (69), and using Eq. (65), the integration on the time variable is carried out, to obtain

$$\begin{aligned} \int_S \frac{[A(r,r',t_{n+1}) - 2A(r,r',t_n) + A(r,r',t_{n-1})]}{\Delta t^2} \cdot f_m dS \;&+\; \int_S \left[\nabla \Psi(r,r',t_n) \cdot f_m\, dS \right] \\ &= \int_S \left[\frac{\partial E^i(r),t_n}{\partial t} \cdot f_m\, dS \right] \end{aligned} \tag{70}$$

Next, we consider the testing procedure on the space variable, as follows:

First, let us consider the testing procedure with the vector potential term. Using Eq. (63), we can write $< A, f_m >$, at any time instant as,

$$\langle f_m, A\rangle = \int_{T_m^+} \frac{l_m}{2A_m^+}\rho_m^+ \cdot A\, dS + \int_{T_m^-} \frac{l_m}{2A_m^-}\rho_m^- \cdot A\, dS. \tag{71}$$

The integrals will be approximated by evaluating A at the centroid of the $T_m^{\pm}$ triangle. Therefore,

$$\langle f_m, A\rangle \approx \left[A(\rho_m^{c+}) \cdot \frac{l_m}{2A_m^+}\int_{T_m^+} \rho_m^{c+}\, dS + A(\rho_m^{c-}) \cdot \frac{l_m}{2A_m^-}\int_{T_m^-} \rho_m^{c-}\, dS\right]. \tag{72}$$

The integrations in Eq. (72) are trivial and the result is given by

$$\langle f_m, A\rangle \approx \frac{l_m}{2}\left[A(\rho_m^{c+}) \cdot \rho_m^{c+} + A(\rho_m^{c-}) \cdot \rho_m^{c-}\right] \tag{73}$$

where ρ_m^{c+} is the vector from the free vertex to the centroid of T_m^+ and ρ_m^{c-} is the vector from the centroid to the free vertex of T_m^-.

Next, let's consider the testing of the scalar potential term. Using the vector identity $\nabla \cdot (\Phi A) = A \cdot \nabla\Phi + \Phi\nabla \cdot A$ and using the properties of the basis function f_m, we have

$$\langle f_m, \nabla_s \Phi\rangle = -\int_S \Phi \nabla_s \cdot f_m\, dS. \tag{74}$$

Using Eq. (64) and approximating the integral by evaluating it at the centroids of the triangles, Eq. (74) becomes

$$\begin{aligned} -\int_S \Phi \nabla_s \cdot f_m\, dS &= -\left[\frac{l_m}{A_m^+}\int_{T_m^+} \Phi\, dS - \frac{l_m}{A_m^-}\int_{T_m^-} \Phi\, dS\right] \\ &\approx -l_m[\Phi(r_m^{c+}) - \Phi(r_m^{c-})] \end{aligned} \tag{75}$$

where $r_m^{c\pm}$ are the centroids of triangles $T_m^{\pm}$.

Finally, the testing procedure is applied to the incident field term. As in the vector potential case, we approximate the integral by using the field evaluated at the center of the m^{th} edge. This assumes that the incident field does not vary in time and space over the triangles $T_m^{\pm}$. This gives,

$$\langle f_m, E^i\rangle \approx \frac{l_m}{2}\left[E^i(\rho_m^{c+}) \cdot \rho_m^{c+} + E^i(\rho_m^{c-}) \cdot \rho_m^{c-}\right] \tag{76}$$

Next, we describe the expansion procedure.

4.2.3 Expansion Procedure

We now consider the expansion procedure. Here, we approximate the current on S by

$$J(r) = \sum_{p=1}^{N_S} \sum_{q=1}^{N_t} I_{p,q} f_p(r)\, g_q(t), \tag{77}$$

where $I_{p,q}$ is the unknown current coefficient at edge p at time $t = t_q$.

Let us first look at the determination of the vector potential at some observation point $r = r_m$ at time $t = t_n$. Substituting Eq. (77) into Eq. (56) gives

$$\begin{aligned} A(r_m, t_n) &= \mu \sum_{p=1}^{N_S} \sum_{q=1}^{N_t} I_{p,q} \int_S \frac{f_p(r') g_q(t_n - \frac{|r_m - r'|}{c})}{4\pi |r_m - r'|} dS' \\ &\approx \sum_{p=1}^{N_S} \sum_{q=1}^{N_t} I_{p,q} \left[g_q(t_n - \frac{R_{mp}^+}{c}) \kappa_{mp}^+ + g_q(t_n - \frac{R_{mp}^-}{c}) \kappa_{mp}^- \right] \end{aligned} \tag{78}$$

with

$$\kappa_{mp}^{\pm} = \int_{T_p^\pm} \frac{\mu f_p^\pm}{4\pi R_m} dS', \tag{79}$$

$$R_{mp}^{\pm} = |r_m - r_p^{c\pm}|, \tag{80}$$

$$R_m = |r_m - r'|, \tag{81}$$

where $T_p^\pm$ represent the triangles connected to p^{th}-basis function.

Now, we consider the evaluation of the derivative of the scalar potential at some observation point $r = r_m$ and time $t = t_n$. Following steps similar to the evaluation of the vector potential, we combine Eqs. (62) and (77) to get

$$\Psi(r_m, t_n) \approx \sum_{p=1}^{N_S} \sum_{q=1}^{N_t} I_{p,q} \left[g_q(t_n - \frac{R_{mp}^+}{c}) \psi_{mp}^+ + g_q(t_n - \frac{R_{mp}^-}{c}) \psi_{mp}^- \right] \tag{82}$$

where

$$\psi_{mp}^{\pm} = \frac{-l_p}{A_p^\pm} \int_{T_k^\pm} \frac{dS'}{4\pi\varepsilon R_m} \tag{83}$$

Using the expansion and testing procedures described so far, it is trivial to generate a matrix equation $ZX = Y$ of dimension $P = N_S \times N_t$. The elements of Z-matrix are formed by using Eqs. (73), (75), (78) and (82). Note that $Z_{p,q}$ represents a matrix element of the Z-matrix, where

$$p = (m-1)N + n, \quad q = (i-1)N + j, \quad m, i = 1, 2, \cdots, N_S, \text{ and } n, j = 1, 2, \cdots, N_t.$$

Further, we note that the Z-matrix in this case will be lower triangular, block-wise Toeplitz as in the case of wire-grid modeling presented in Chapter 3. At this stage, we note that multiple incident pulses with varying frequency content can be easily accommodated by adding more column blocks to the Y-matrix.

Lastly, note that the numerical procedure presented so far allows to obtain the current distribution on the scattering structure as a function as time. Once an accurate current distribution is obtained, it is a simple process to obtain near-fields, far-fields, and any other required parameters. The mathematical details to obtain such parameters are well-known and available in [9] and hence not repeated here.

4.3 Numerical Results

In this section, we present numerical results for several conducting objects modeled by triangular patches. Further, for all examples, the incident field is given by

$$E^i(t,r) = E_o \frac{4}{T_P\sqrt{\pi}} e^{-\gamma^2} \tag{84}$$

where

$$\gamma = \frac{4}{T_P}(ct - ct_o - r \cdot a_k). \tag{85}$$

In Eqs. (84) and (85), a_k is the unit vector in the direction of propagation of the incident wave, T_P is the pulse width of the Gaussian impulse, $E_o \cdot a_k = 0$, r is a position vector relative to the origin, c is the velocity of propagation in the external medium, and t_o is a time delay which represents the time at which the pulse peaks at the origin. Also, we have $E_o = 120\pi a_x$, $ct_0 = 6.0$ LM, $T_P = 4.0$ LM, and $k = -a_z$. Note that 1 LM $= 3.333$ nSecs. Further, for all examples, we have $T = 2 * ct_0 = 12$ LM, by which time the incident pulse drops to negligible value.

As a first example, consider a square plate of 2.0×2.0 m, located in the XY-plane. The plate is illuminated by a Gaussian plane wave described by Eq. (84). The induced current on the plate is obtained using the new procedure. There are 153 and 108 basis functions for space and time variables, respectively, for the time-domain solution. The results are compared with the solution obtained using the frequency domain MOM using the same spatial patch scheme and inverse discrete Fourier transform (FD-IDFT). The FD-IDFT solution is obtained by using 512 frequency samples in the 0 to 512 MHz range. For illustration purposes, the induced current density at the center of the plate is shown in Figure 26 and note that the solutions compare very well.

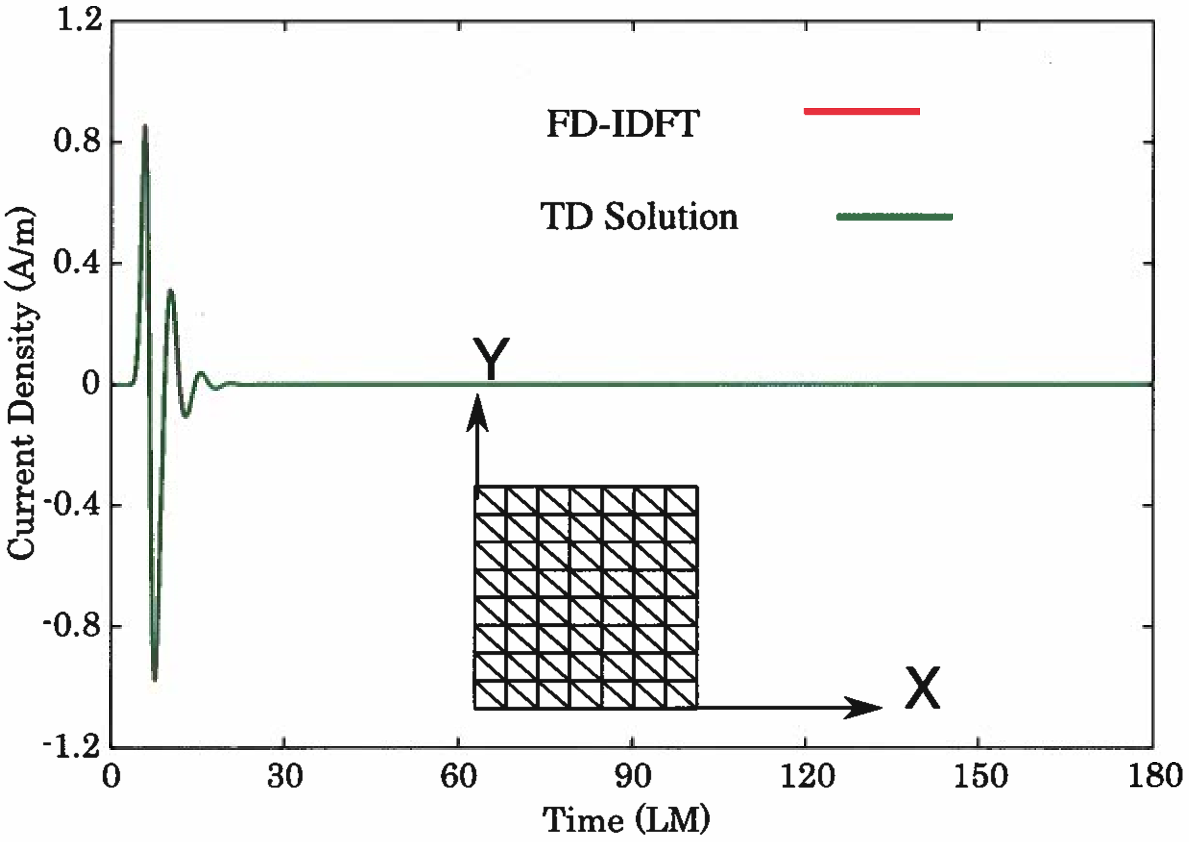

Fig. 26 — Current induced at the center of a square plate (L=2.0 m) illuminated by a Gaussian plane wave.

Next, we consider a sphere of radius 1.0 m, located with the center coinciding with the coordinate origin. The sphere is illuminated by a Gaussian plane wave described by Eq. (84). The sphere is modeled with 722 triangular patches with 1083 spatial basis functions. The time-domain solution is obtained by employing 60 basis functions in time. The results are compared with the solution obtained using the frequency domain MOM using the same spatial patch scheme and inverse discrete Fourier transform (FD-IDFT). The FD-IDFT solution is obtained by using 512 frequency samples in the 0 to 512 MHz range. For illustration purposes, the induced current density at the equator is shown in Figure 27 and note that the solutions compare very well.

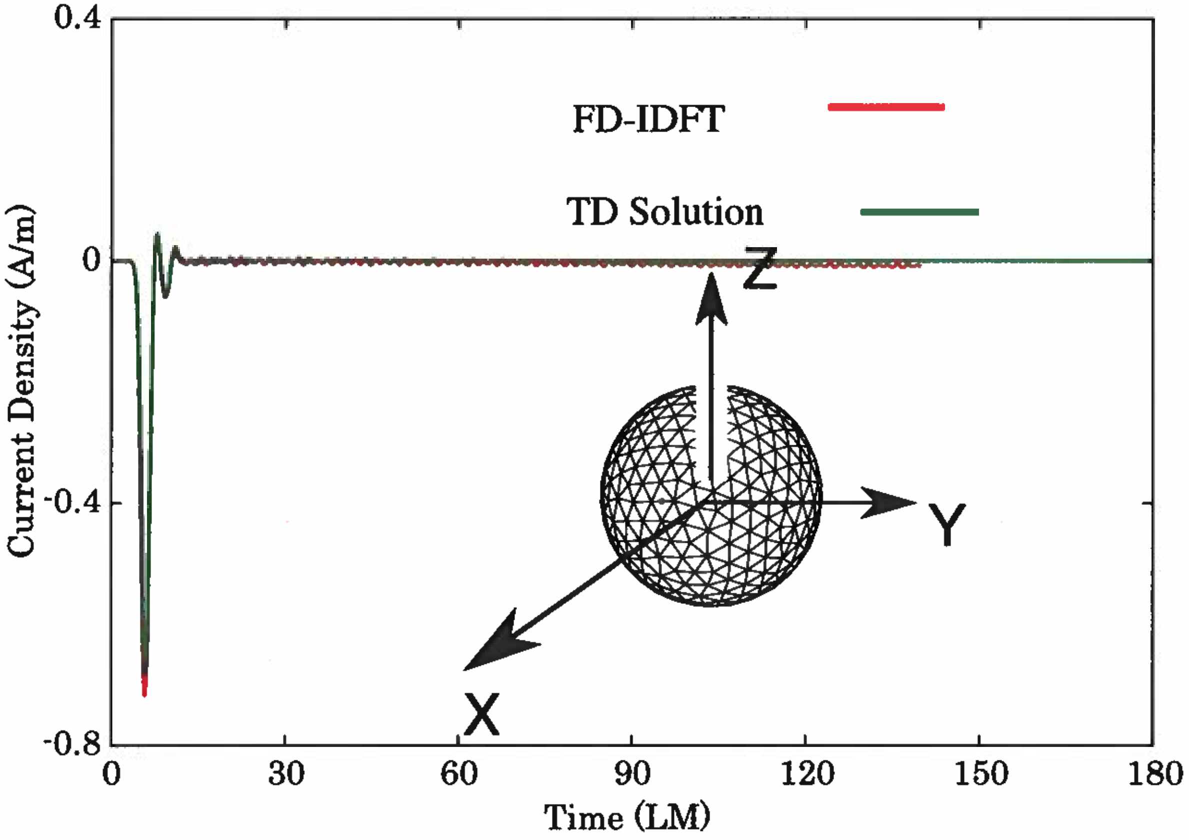

Fig. 27 — Current induced at the equator, shown by a red dot, of a conducting sphere (a=1.0 m) illuminated by a Gaussian plane wave.

Next, we consider a conducting cube of side length 1.0 m, located with the center coinciding with the coordinate origin. The cube is illuminated by a Gaussian plane wave described by Eq. (84). The cube is modeled with 224 triangular patches with 336 spatial basis functions. The time-domain solution is obtained by employing 60 basis functions in time. The results are compared with the solution obtained using the frequency domain MOM using the same spatial patch scheme and inverse discrete Fourier transform (FD-IDFT). The FD-IDFT solution is obtained by using 512 frequency samples in the 0 to 512 MHz range. For illustration purposes, the induced current density at the center of the top face is shown in Figure 28 and note that the solutions compare very well.

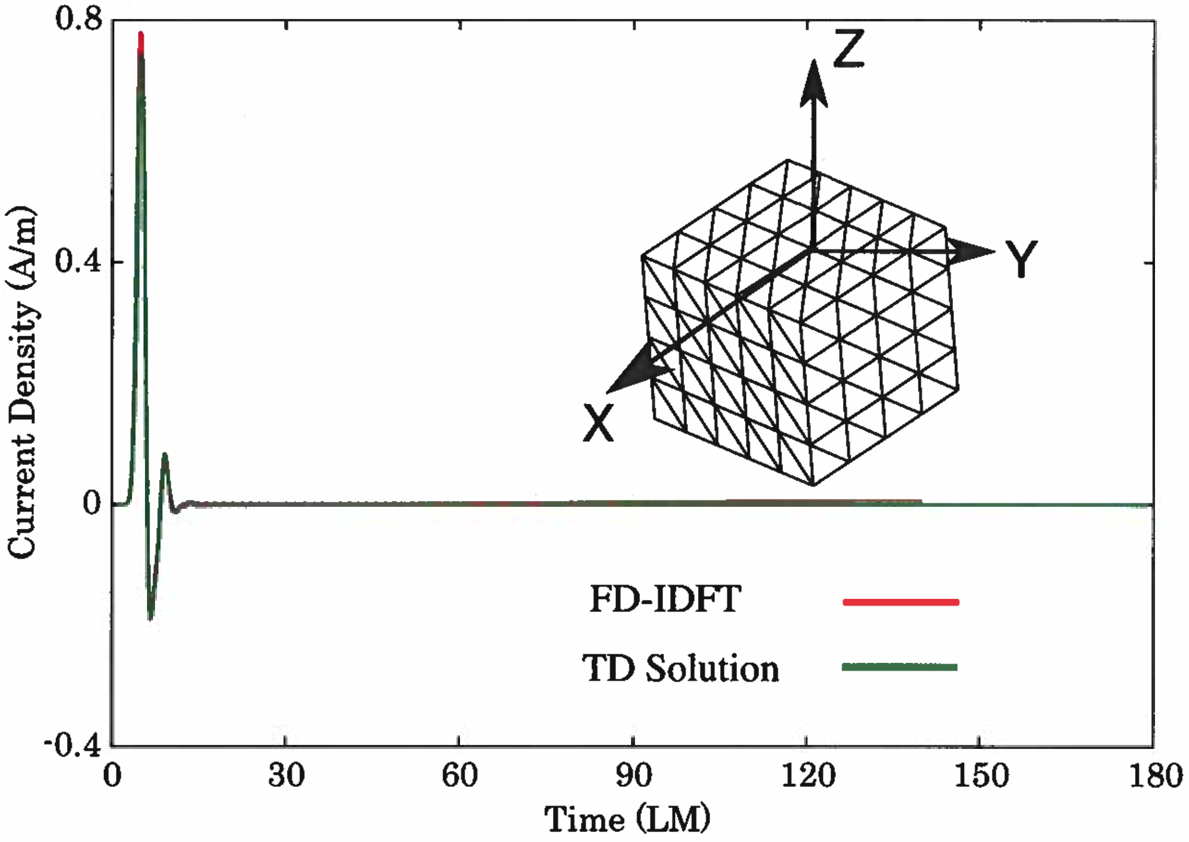

Fig. 28 — Current induced at the center of the top face of a conducting cube (a=1.0 m) illuminated by a Gaussian plane wave.

Next, we consider a combination of two square plates, each of side length $a = 1.0$ m and separated by $d = 0.1$ m, located with the center of the bottom plate coinciding with the coordinate origin. The two-plate configuration is illuminated by a Gaussian plane wave described by Eq. (84). Each plate is modeled with 112 triangular patches resulting in 366 spatial basis functions. The time-domain solution is obtained by employing 60 basis functions in time. The results are compared with the solution obtained using the frequency domain MOM using the same spatial patch scheme and inverse discrete Fourier transform (FD-IDFT). The FD-IDFT solution is obtained by using 512 frequency samples in the 0 to 512 MHz range. For illustration purposes, the induced current density at the center of the top plate is shown in Figure 29 and note that the solutions compare very well. We note that the induced current oscillates for a long time because of the close proximity of the plates and the solution captures this phenomenon very well.

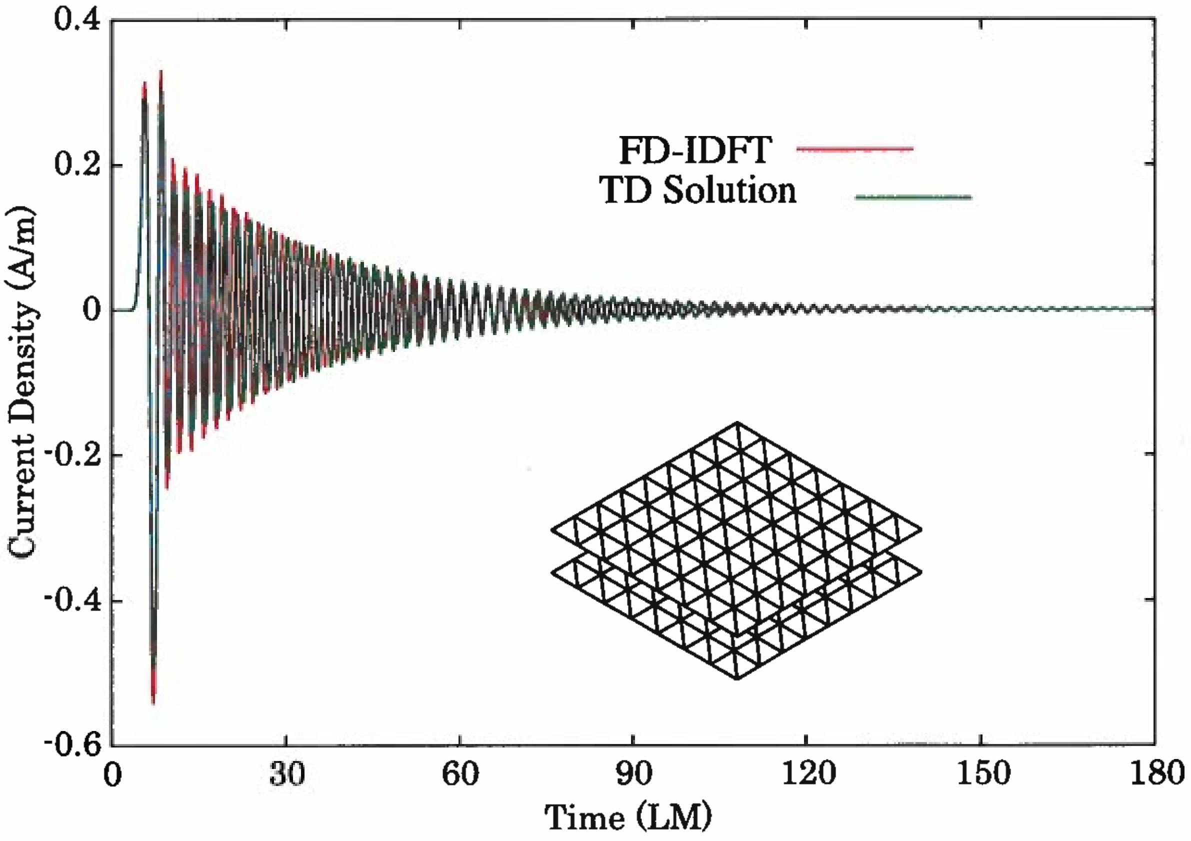

Fig. 29 — Current induced at the center of the top plate of a parallel plate configuration (a=1.0 m, d=0.1 m) illuminated by a Gaussian plane wave.

Now, we consider a combination of three square plates, each of side length $a = 1.0$ m and separated by $d = 0.2$ m, located with the center of the center plate coinciding with the coordinate origin. The three-plate configuration is illuminated by a Gaussian plane wave described by Eq. (84). Each plate is modeled with 180 triangular patches resulting in 753 spatial basis functions. The time-domain solution is obtained by employing 60 basis functions in time. The results are compared with the solution obtained using the frequency domain MOM using the same spatial patch scheme and inverse discrete Fourier transform (FD-IDFT). The FD-IDFT solution is obtained by using 512 frequency samples in the 0 to 512 MHz range. For illustration purposes, the induced current density at the center of the middle plate is shown in Figure 30 and note that the solutions compare very well. It is obvious that this configuration represents a complex scattering structure from the scattering point of view. The electromagnetic wave bounces back and forth between the plates and takes a very long time to decay to negligible value.

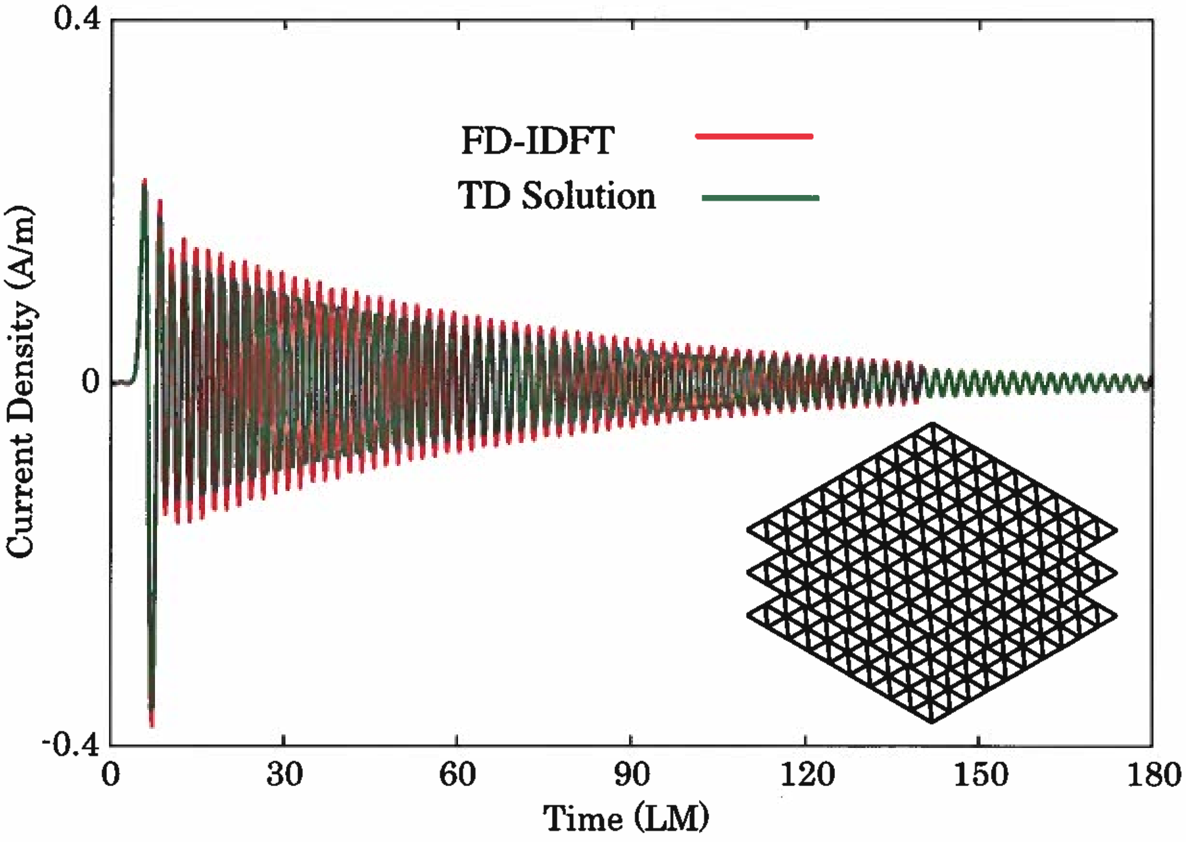

Fig. 30 — Current induced at the center of the center plate of a 3-parallel plate configuration (a=1.0 m, d=0.2 m) illuminated by a Gaussian plane wave.

Next, we consider an almond-shaped structure described in the inset of Figure 19. The almond is modeled with 432 triangular patches resulting in 648 spatial basis functions. The time-domain solution is obtained by employing 60 basis functions in time. The results are compared with the solution obtained using the frequency domain MOM using the same spatial patch scheme and inverse discrete Fourier transform (FD-IDFT). The FD-IDFT solution is obtained by using 512 frequency samples in the 0 to 512 MHz range. For illustration purposes, the induced current density at the center of the equator is shown in Figure 31 and note that the solutions compare very well. It is well-known that the almond-shaped body represents a body with low radar cross section and the time domain solution performs very well for this case.

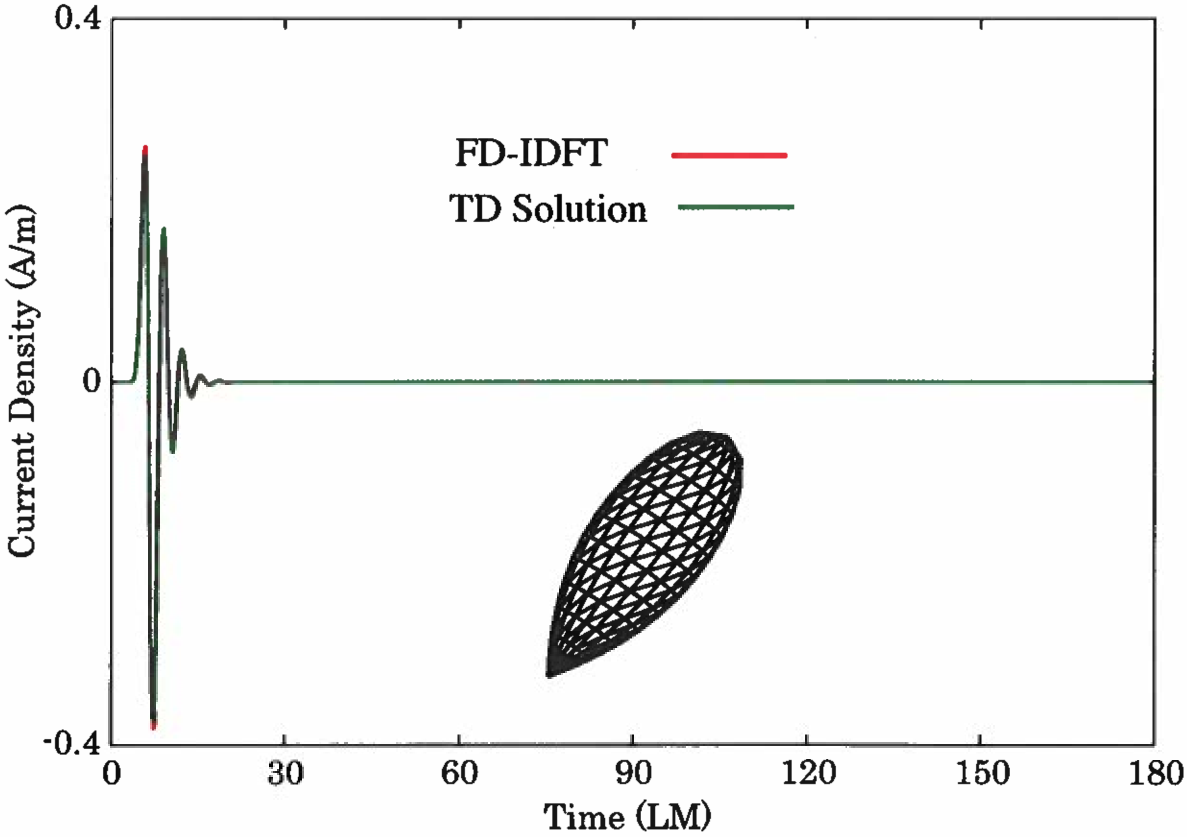

Fig. 31 — Current induced at the center of the equator of an almond-shaped structure illuminated by a Gaussian plane wave.

Next, we consider an aircraft-like object, as shown in Figure 13. The object is symmetrically placed in the XY-plane such that the center of the lower-side (belly) approximately coincides with the coordinate origin. The object dimensions are: 0.97 m, 0.86 m, and 0.25 m along the X, Y, and Z axes, respectively. There are 1000 and 48 basis functions for space and time variables, respectively, for the time domain solution. The current is sampled at the middle of an edge shown by a dot in the Figure 13. The IDFT solution is obtained in a similar manner as in the previous example. The results obtained by FD-IDFT, and the present method are shown in Figure 32. Again, we note good comparison between the two solutions.

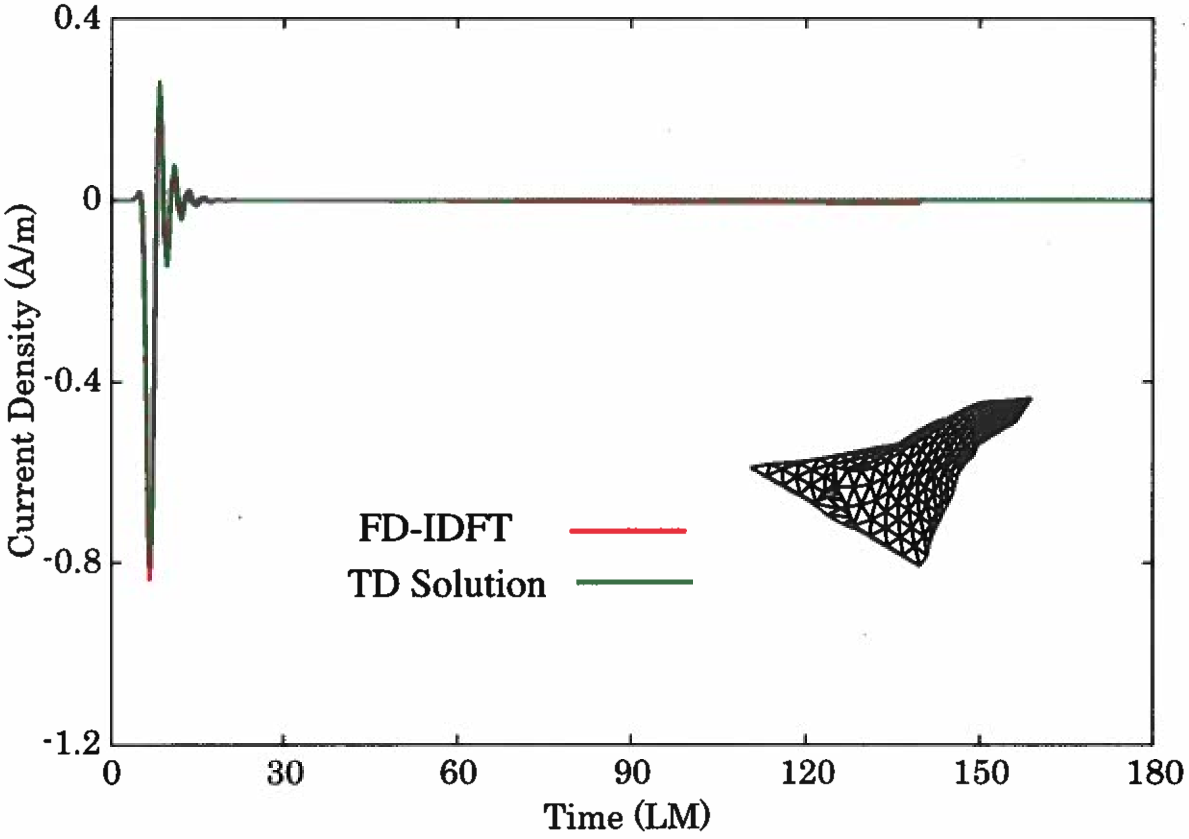

Fig. 32 — Current induced on an aircraft-like structure illuminated by a Gaussian plane wave.

Next, we consider a more complex aircraft-like object, as shown in Figure 33. The object dimensions are: 5.85 m, 3.5 m, and 1.46 m along the X, Y, and Z axes, respectively. There are 2673 and 40 basis functions for space and time variables, respectively, for the time domain solution. The current is sampled on a wing, shown by a red dot, in the Figure 33. The IDFT solution is obtained in a similar manner as in the previous example. The results obtained by FD-IDFT, and the present method are shown in Figure 34. Again, we note good comparison between the two solutions.

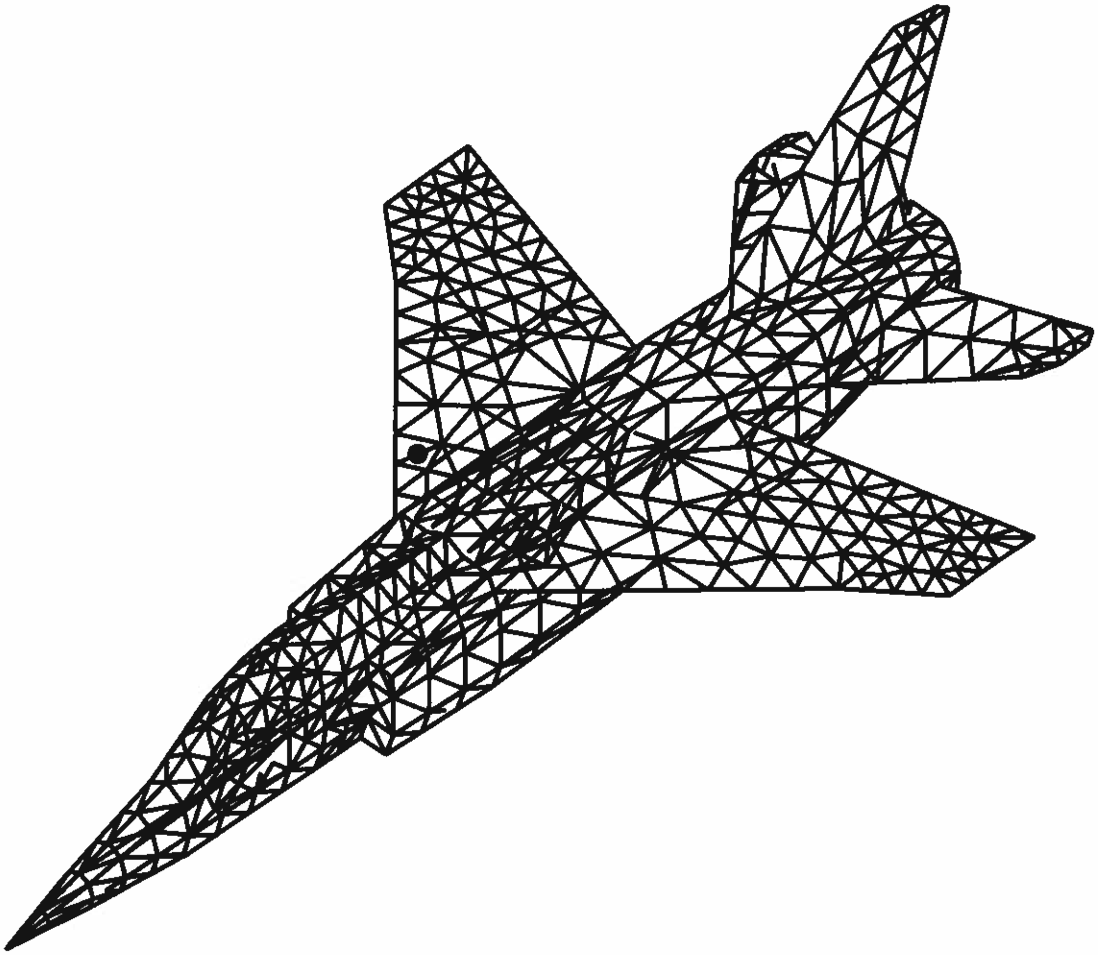

Fig. 33 — Triangulated model of an aircraft.

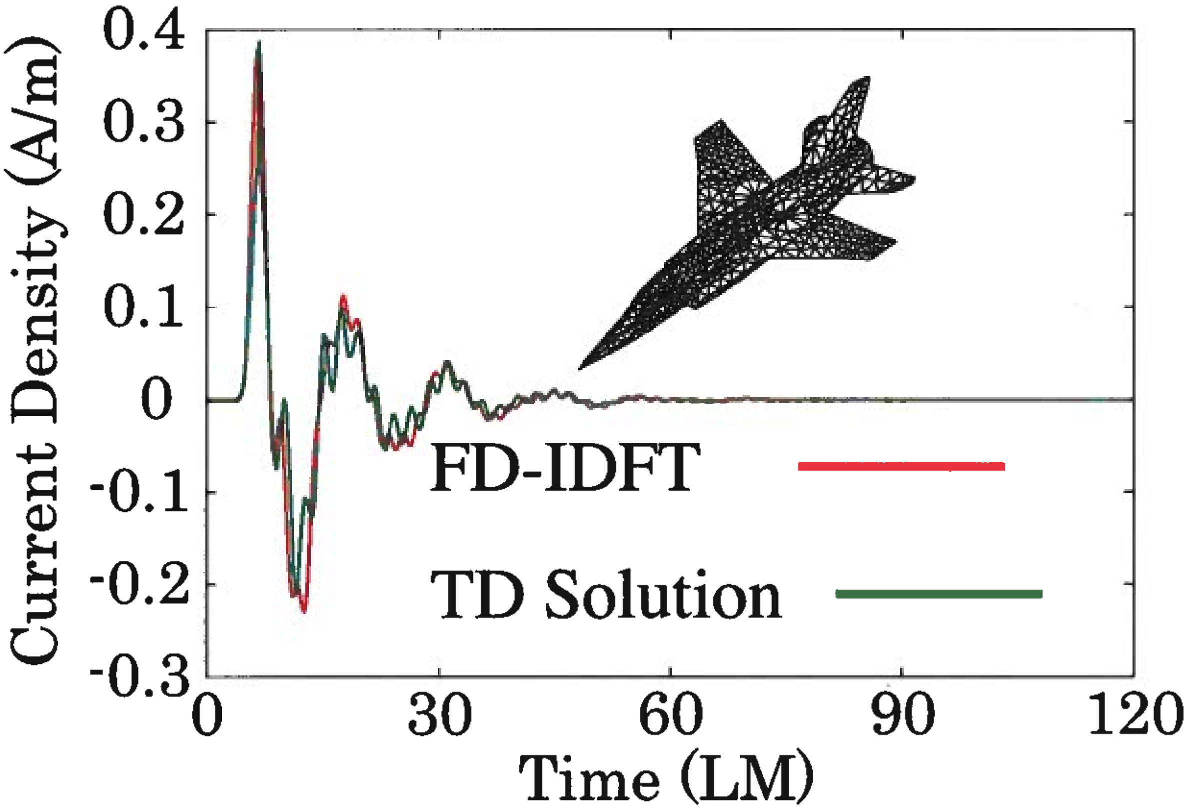

Fig. 34 — Current induced on the wing of a model aircraft illuminated by a Gaussian plane wave.

Next, we consider a deep cavity as shown in the inset of Figure 35. The depth of the cavity is 2.0 m. The inner and outer radii of cavity are 0.267 m and 0.4 m, respectively. The object is symmetrically placed in the XY-plane such that the center of the bottom surface coincides with the coordinate origin. There are 552 and 40 basis functions for space and time variables, respectively, for the time domain solution. The current is sampled at an edge located in the inner surface at the bottom of the cavity. The results obtained by FD-IDFT, and the present method are shown in Figure 35. Although we see a reasonable comparison, considering the complexity of the problem, it is speculated that neither solution is converged to the correct solution because of the coarse spatial sampling. The currents inside the deep zone are difficult to obtain and may require much higher number of unknowns.

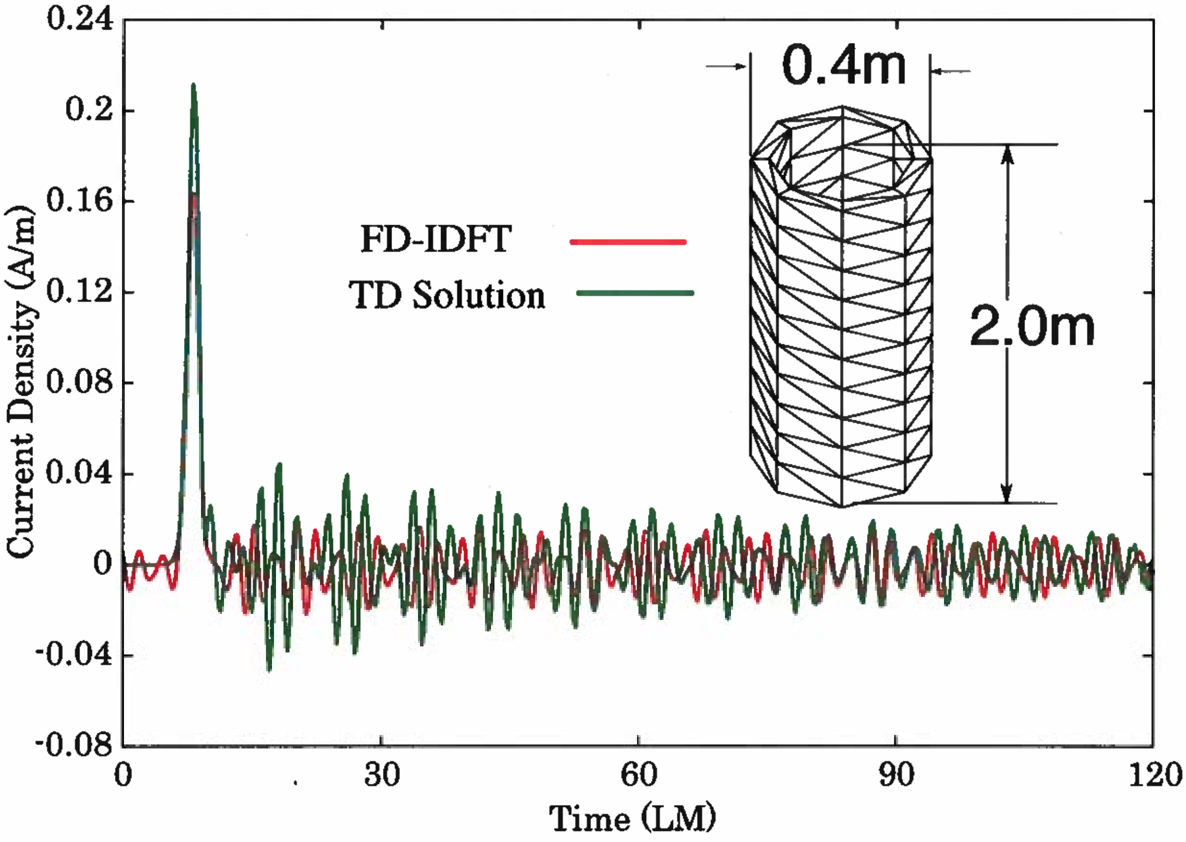

Fig. 35 — Current induced on the bottom surface of a deep cavity illuminated by a Gaussian plane wave.

Finally, we consider a ship-like object, shown in Figure 22. The ship is 5.56 m long, 0.716 m wide, and 0.387 m height and placed such that the origin is approximately coinciding with center of the top deck. There are 13,395 and 40 basis functions for space and time variables, respectively, for the time domain solution. The current is sampled at the middle of the upper-deck approximately coinciding with $x = y = 0$. The numerical results obtained by the method presented in this work is shown in Figure 36. Also, note that IDFT solution for this example is prohibitively expensive and hence not attempted.

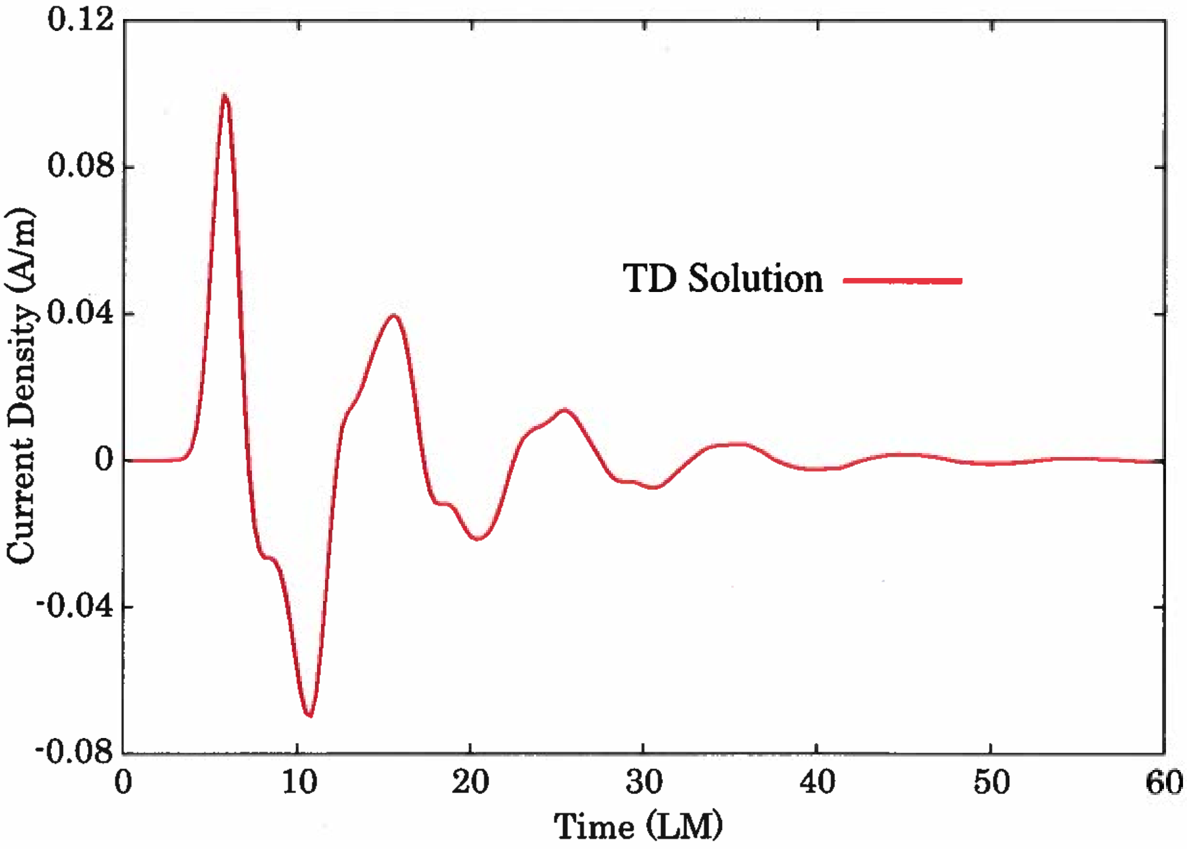

Fig. 36 — Current at the selected point on the ship-like object modeled by triangular patches.

5. RCS CALCULATION FROM TIME DOMAIN DATA

In this chapter, we present RCS calculations of selected targets after obtaining the current induced as a function time from the technique as described in the previous chapter. Once the induced current at all locations is obtained as a function of time, we use the straight-forward Fourier Transform method to obtain the currents at a given frequency. The Fourier transform for a time domain data may be defined as

$$I_k(f) = 2\pi \int_{t=0}^{\infty} i_k(t) e^{-j2\pi f t}\, dt \tag{86}$$

where $i_k(t)$ is the current induced at k^{th}-basis function and f is the given frequency. Here, we note that the induced current is zero for $t < 0$.

Since the current data is obtained at equal time intervals, the integral in Eq. (86) may be easily approximated by

$$I_k(f) = 2\pi \sum_j i_k(j\Delta t) e^{-j2\pi f j\Delta t}\, \Delta t \tag{87}$$

where Δt is the time interval. Next, the far-scattered electric field is obtained by the expression, given by

$$E^s(r) = -j\omega\mu \frac{e^{-jkr}}{4\pi r} \int_S f_k(r')\, e^{ja_k \cdot r'}\, dS' \tag{88}$$

where f_k represents the k^{th}-basis function, $\omega = 2\pi f$, $k = \frac{\omega}{c}$ is the wave number, a_k represents the unit vector from the origin to the observation point, and c is the velocity of the electromagnetic wave.

Lastly, the radar cross section (σ) is given by

$$\sigma(\theta, \phi) = \lim_{r \to \infty} 4\pi r^2 \frac{|E^s|^2}{|E^{inc}|^2} \tag{89}$$

which can be easily computed from Eq. (88) and the incident field given in Eq. (84).

Next, we present RCS (σ) of several objects at number of frequencies and compare with the frequency domain solution. We present two cases *viz.* a) Elevation cut (E-cut) where σ is obtained as a function of θ at $\phi = 0^0$ and b) Horizontal cut (H-cut) where σ is obtained as a function of ϕ at $\theta = 90^0$. Also, initially we use the time-domain solution due to the incident pulse as given in Eq. (84) to obtain RCS at 75 and 150 MHz. We note that the incident pulse described in Eq. (84) has a pulse width $T_p = 4.0$ LM and, hence, essentially a low-frequency pulse with limited bandwidth from 0 to 200 MHz. Later, we present results for several higher frequencies using a sharper pulse.

As a first example, we consider the square plate of length 2.0 m located in the XY-plane as shown in the inset of Figure 26. The number of basis functions for this case is 153. In Figure 37, we present the normalized bistatic RCS at 75 MHz and 150 MHz and compare with the frequency domain solution. We note a good comparison between the direct time domain solution and the frequency domain solution at these two frequencies.

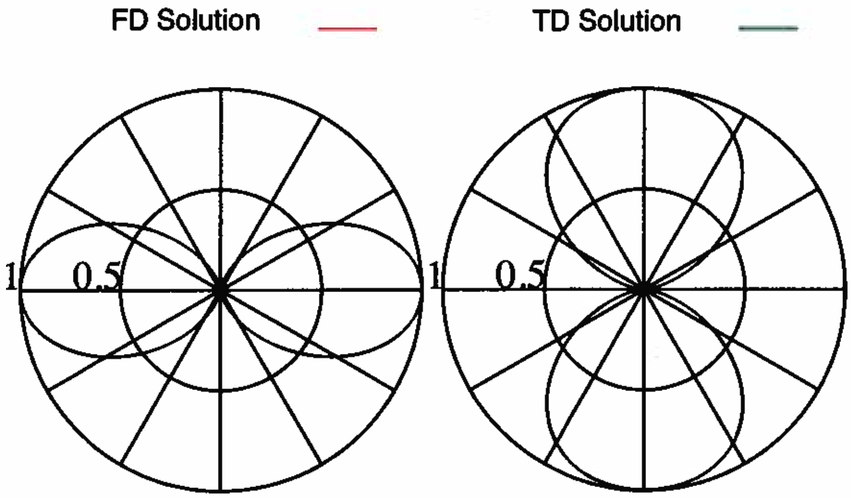

E-cut (75 MHz) H-cut (75 MHz)

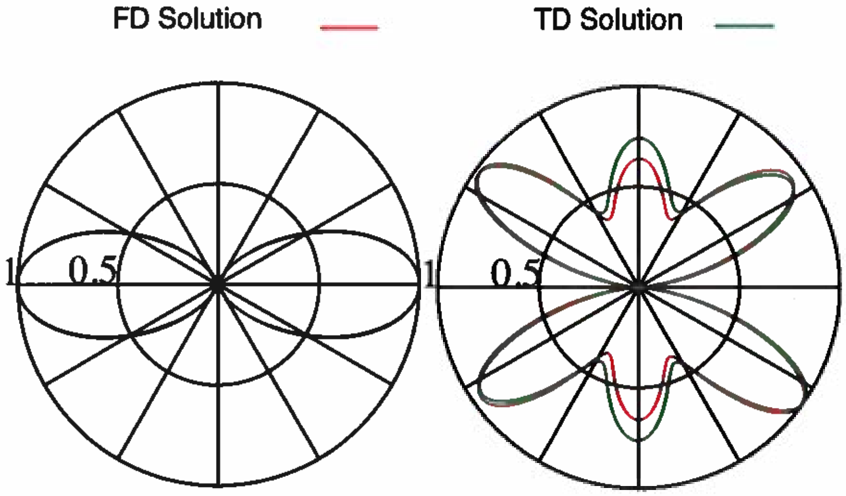

E-cut (150 MHz) H-cut (150 MHz)

Fig. 37 — Normalized bistatic RCS of a square plate (2 × 2 m) located in the XY-plane with center coinciding with the origin at 75 MHz and 150 MHz.

Next, we consider a conducting sphere of radius 1.0 m located with center coinciding with the origin and shown in the inset of Figure 27. The number of basis functions for this case is 1083. In Figure 38, we present the normalized bistatic RCS at 75 MHz and 150 MHz and compare with the frequency domain solution. Although both solution compare well, the minor deviations may be attributed to the selected incident pulse in the time domain because at these frequencies the amplitude of the incident pulse is quite low.

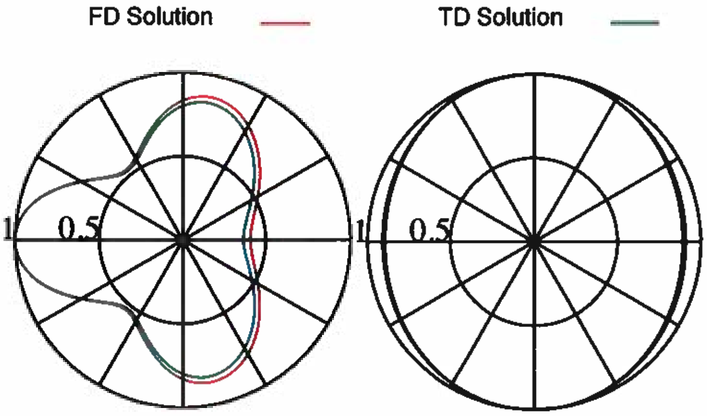

E-cut (75 MHz)

H-cut (75 MHz)

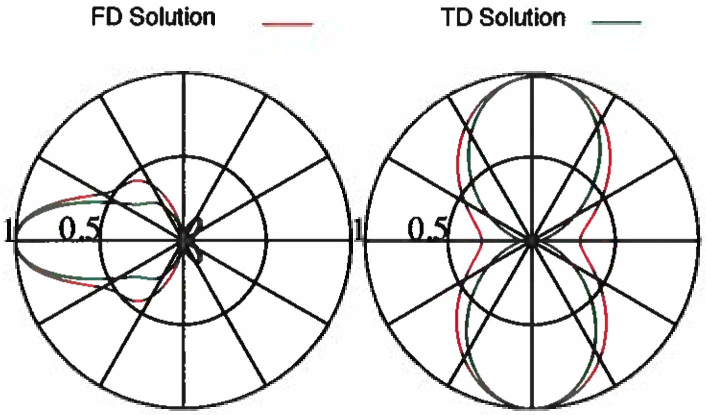

E-cut (150 MHz)

H-cut (150 MHz)

Fig. 38 — Normalized bistatic RCS of a conducting sphere, radius 1 m, located with center coinciding with the origin at 75 MHz and 150 MHz.

Next, we consider a conducting cube presented in Figure 28. The number of basis functions for this case is 882. In Figure 39, we present the normalized bistatic RCS at 75 MHz and 150 MHz and compared with the frequency domain solution. The figure shows both the elevation cut (E-cut) and azimuthal cut (H-cut) and we note a good comparison between the direct time domain solution and the frequency domain solution.

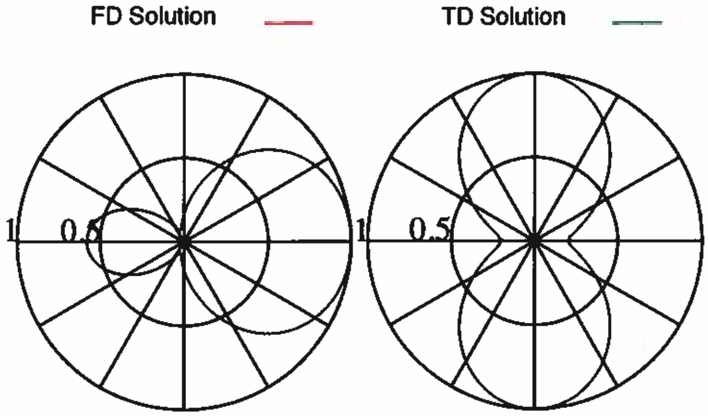

E-cut (75 MHz) H-cut (75 MHz)

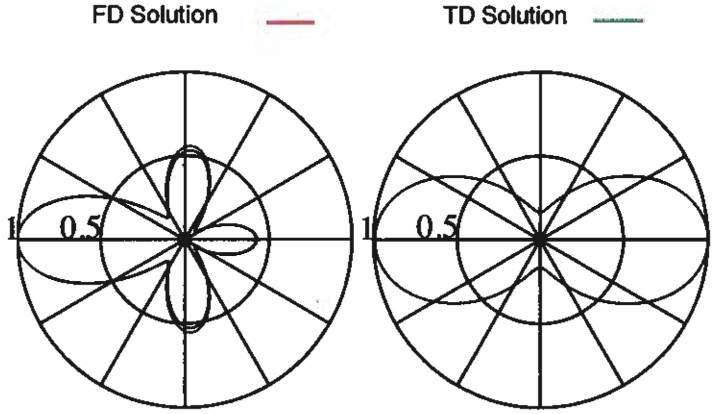

E-cut (150 MHz) H-cut (150 MHz)

Fig. 39 — Normalized bistatic RCS of a conducting cube, length 1 m at 75 MHz and 150 MHz.

Next, we consider a conducting almond presented in Figure 19. In Figure 40, we present the normalized bistatic RCS at 75 MHz and 150 MHz and compared with the frequency domain solution. The figure shows both the elevation cut (E-cut) and azimuthal cut (H-cut) and we note a good comparison between the direct time domain solution and the frequency domain solution. The number of basis functions for this case is 648.

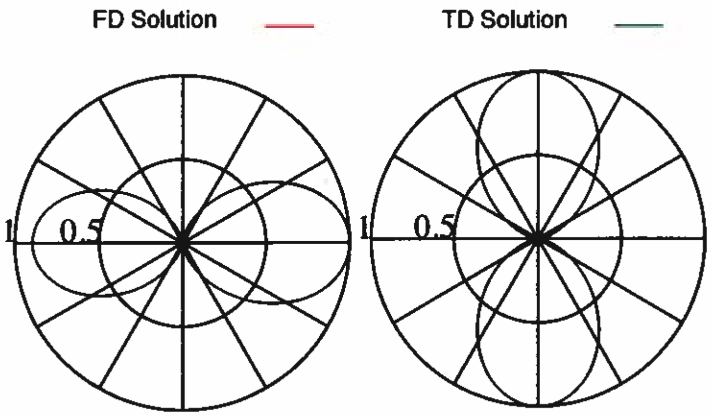

E-cut (75 MHz) H-cut (75 MHz)

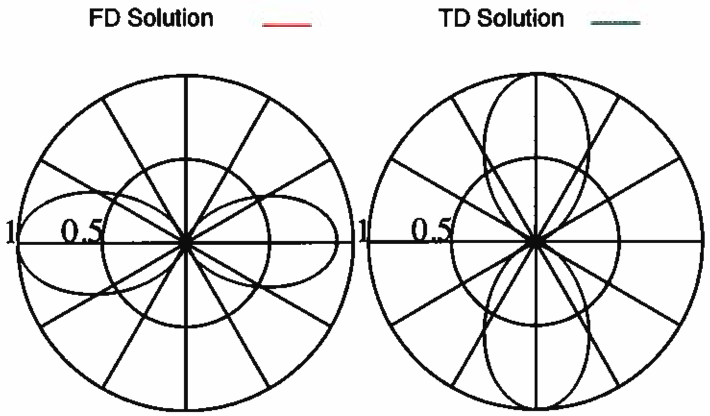

E-cut (150 MHz) H-cut (150 MHz)

Fig. 40 — Normalized bistatic RCS of a conducting almond at 75 MHz and 150 MHz.

Next, we consider an aircraft-like body presented in Figure 13. In Figure 41, we present the normalized bistatic RCS at 75 MHz and 150 MHz and compared with the frequency domain solution. The figure shows both the elevation cut (E-cut) and azimuthal cut (H-cut) and we note a good comparison between the direct time domain solution and the frequency domain solution. The number of basis functions for this case is 1000.

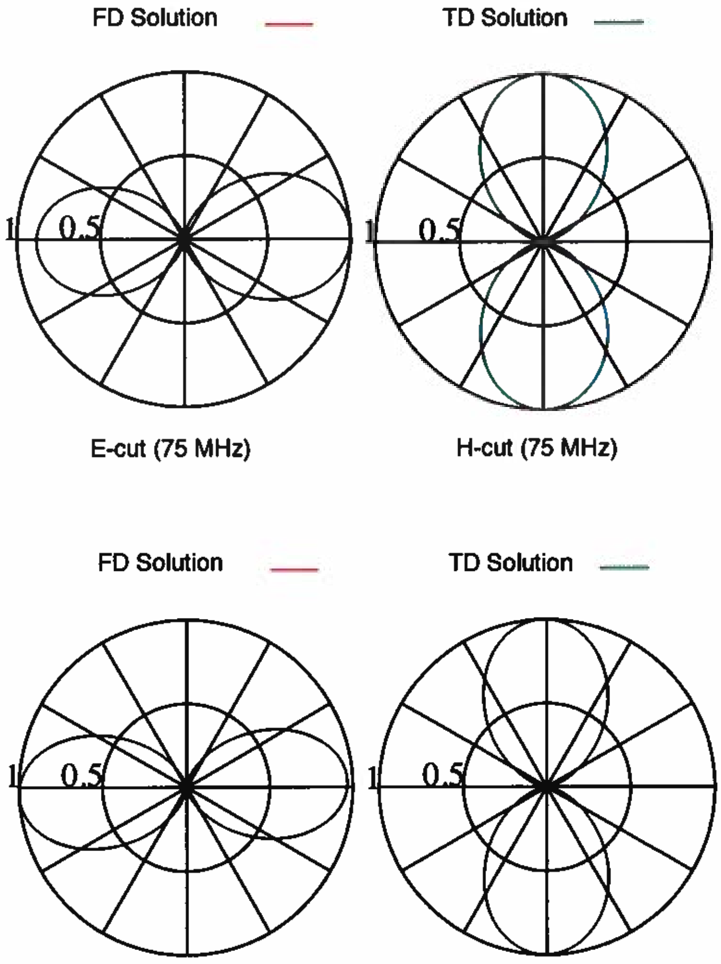

E-cut (75 MHz) H-cut (75 MHz)

E-cut (150 MHz) H-cut (150 MHz)

Fig. 41 — Normalized bistatic RCS of an aircraft-like body at 75 MHz and 150 MHz.

Now, we present RCS (σ) of four objects, *i.e.* a) square plate, b) conducting sphere, b) a deep cavity, and d) an aircraft-like object. The frequencies considered are: 300 MHz, 600 MHz, 900 MHz, 1200 MHz, and 1500 MHz. The time domain solution is obtained with a much sharper pulse with pulse width $T_p =$ 0.5 LM providing a bandwidth from 0 to 1.5 GHz. We compare the numerical results with the frequency domain solution. We note that the time domain solution requires a single computer simulation, whereas the frequency domain solution must be carried out at each frequency separately.

Consider a square plate of length 0.5 m located in the XY-plane as shown in the Figure 42. The number of basis functions for this case is 2,628. In Figures 43, 44, and 45, we present the normalized bistatic RCS at 300 MHz, 600 MHz, 900 MHz, 1200 MHz and 1500 MHz and compare with the frequency domain solution. We note a good comparison between the direct time domain solution and the frequency domain solution for the selected frequencies. However, some minor deviation for the H-cut may be attributed to the fact that the RCS for H-cut is quite low.

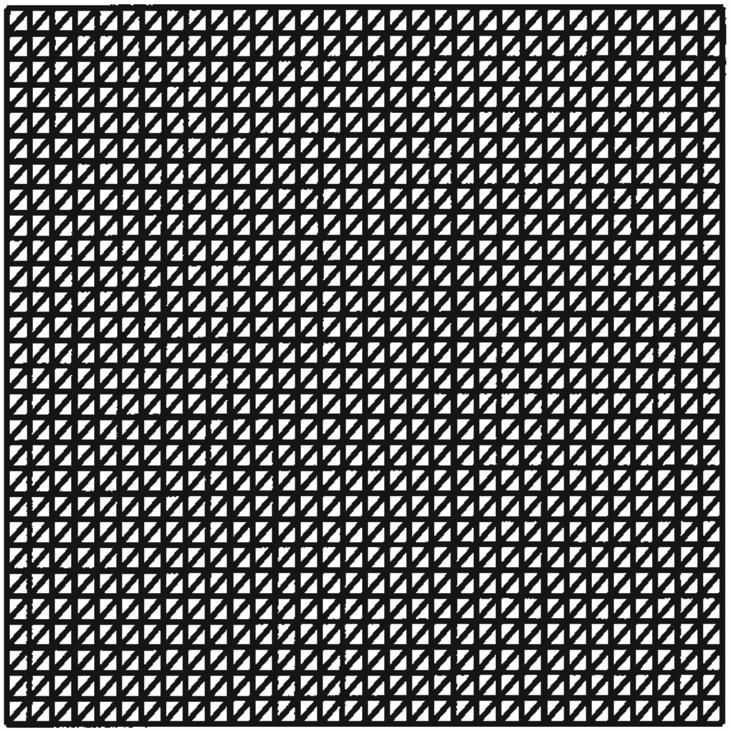

Fig. 42 — Triangulated model of a square plate.

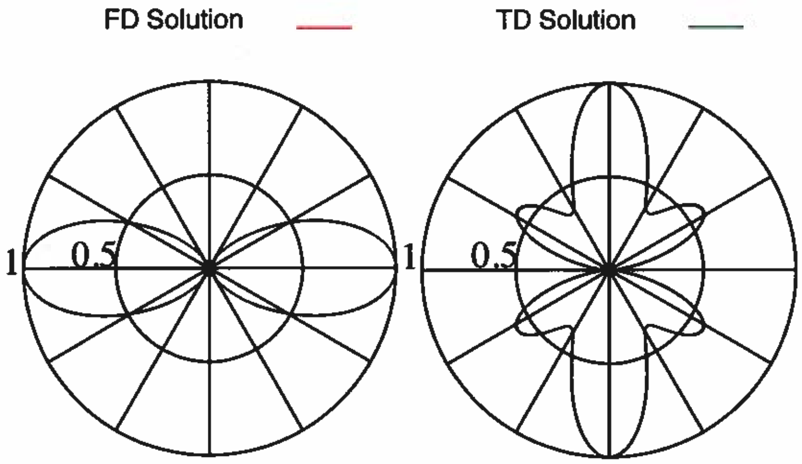

E-cut (300 MHz) H-cut (300 MHz)

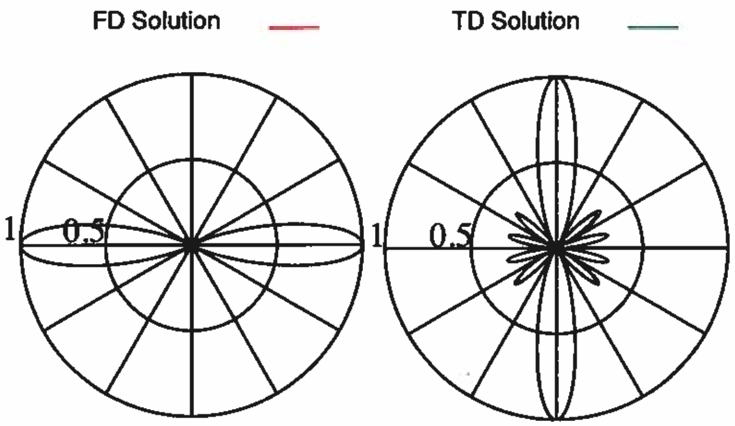

E-cut (600 MHz) H-cut (600 MHz)

Fig. 43 — Normalized bistatic RCS of a square plate (0.5 × 0.5 m) located in the XY-plane with center coinciding with the origin at 300 MHz and 600 MHz.

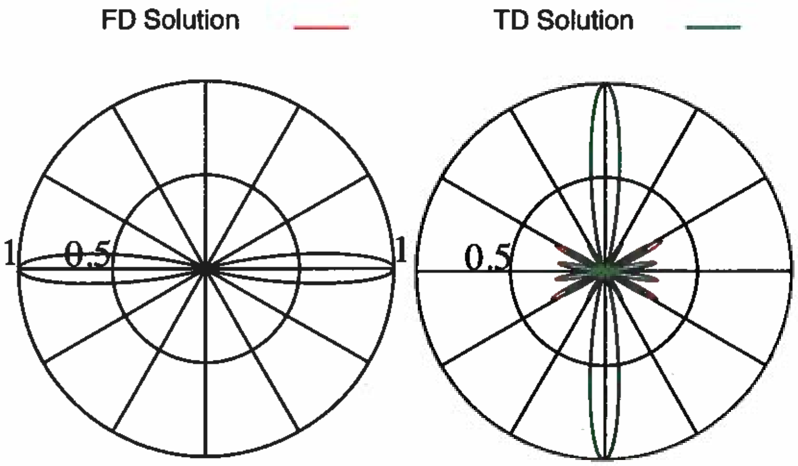

E-cut (900 MHz) H-cut (900 MHz)

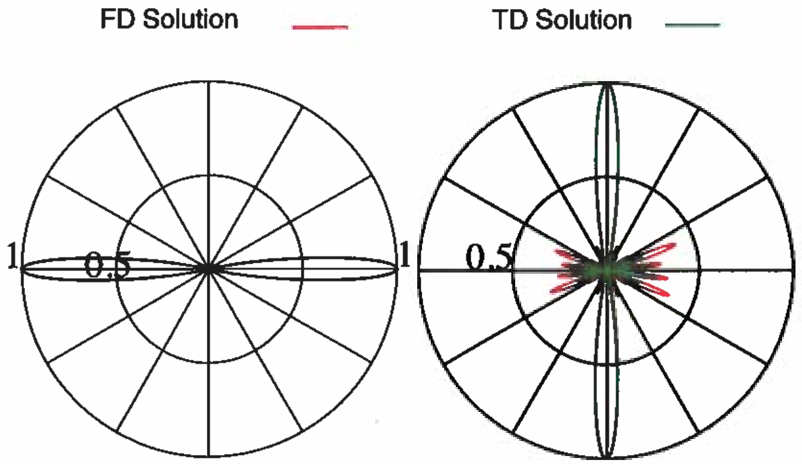

E-cut (1200 MHz) H-cut (1200 MHz)

Fig. 44 — Normalized bistatic RCS of a square plate (0.5 × 0.5 m) located in the XY-plane with center coinciding with the origin at 900 MHz and 1200 MHz.

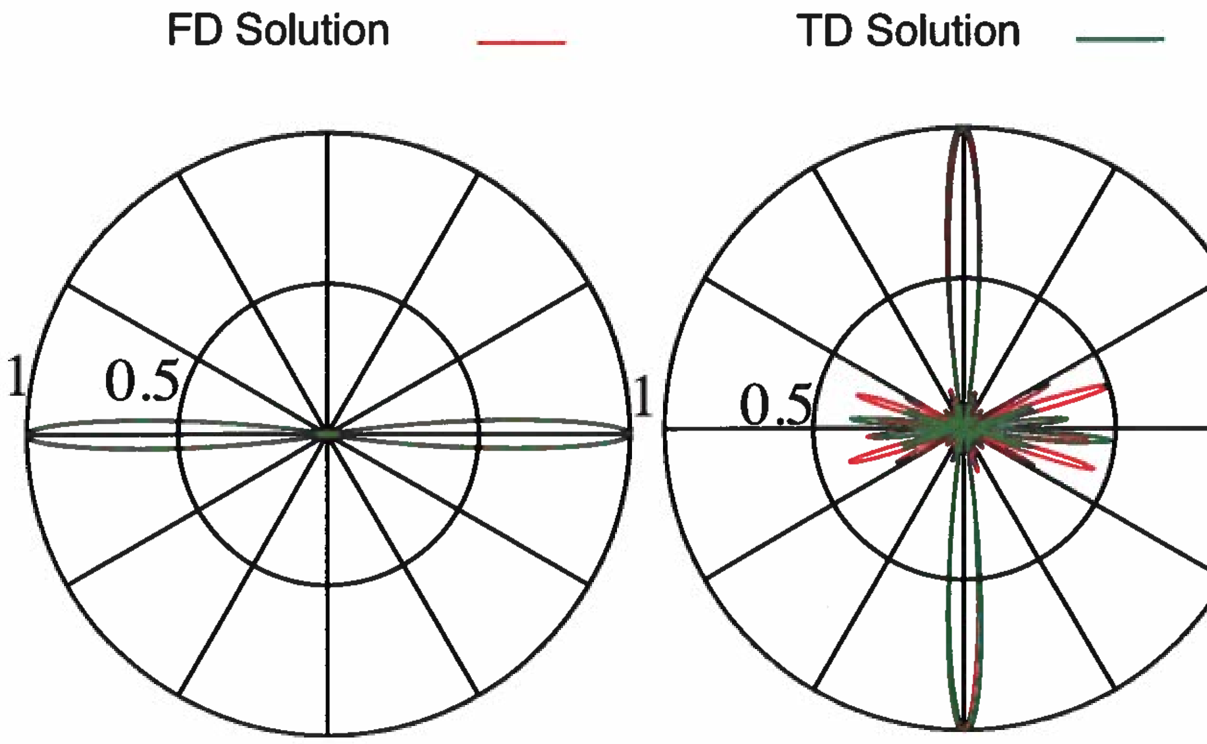

E-cut (1500 MHz) H-cut (1500 MHz)

Fig. 45 — Normalized bistatic RCS of a square plate (0.5 × 0.5 m) located in the *XY*-plane with center coinciding with the origin at 1500 MHz.

Next, we consider a conducting sphere of radius 0.25 m located with center coinciding with the origin. The triangulated model of the sphere is shown in Figure 46. The number of basis functions for this case is 2,160. In Figures 47, 48, and 49, we present the normalized bistatic RCS at 300 MHz, 600 MHz, 900 MHz, 1200 MHz and 1500 MHz and compare with the frequency domain solution. We note a good comparison between the direct time domain solution and the frequency domain solution for the selected frequencies. The differences in the H-cut may be attributed to a weak component of the scattered field.

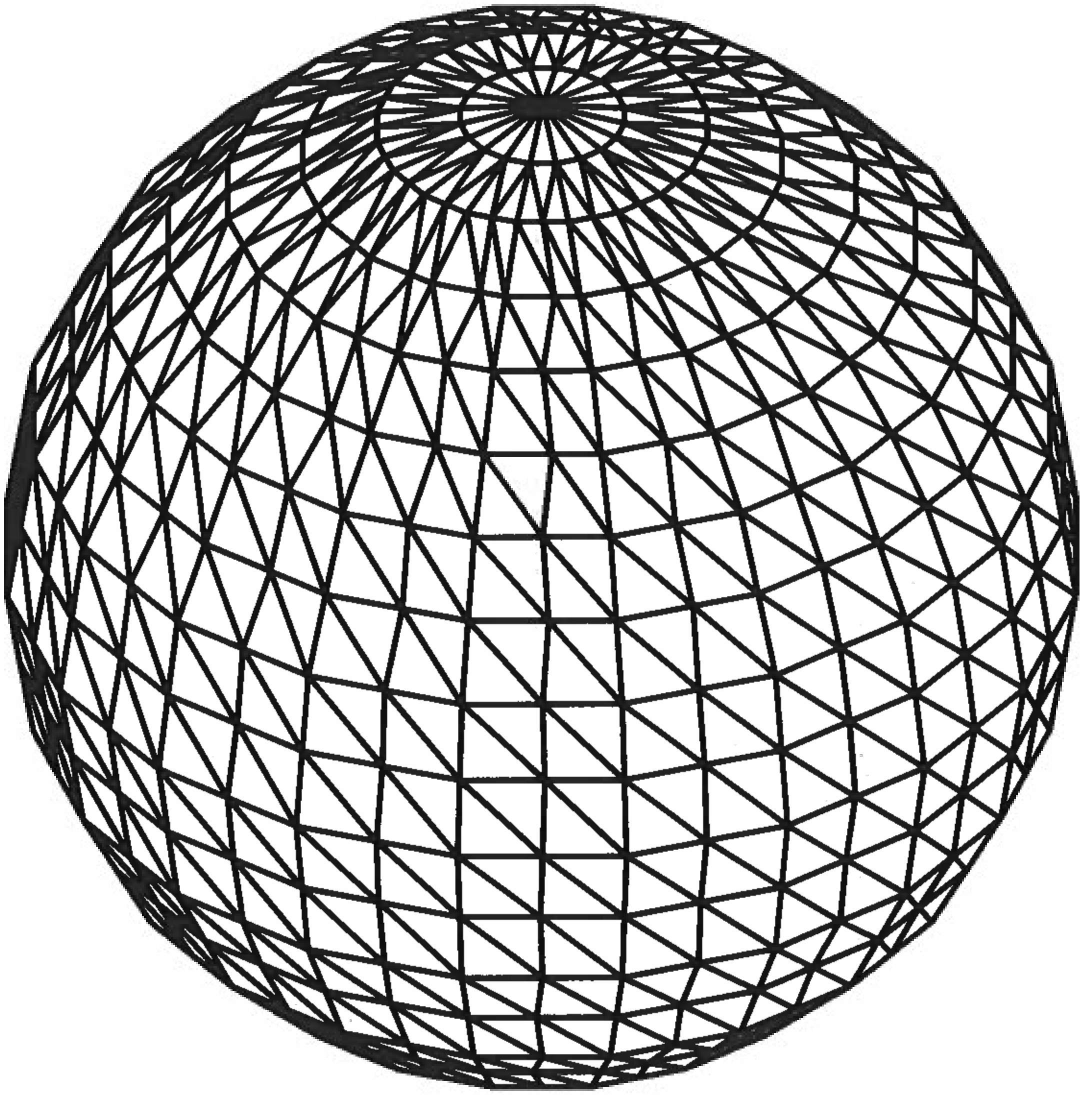

Fig. 46 — Triangulated model of a sphere.

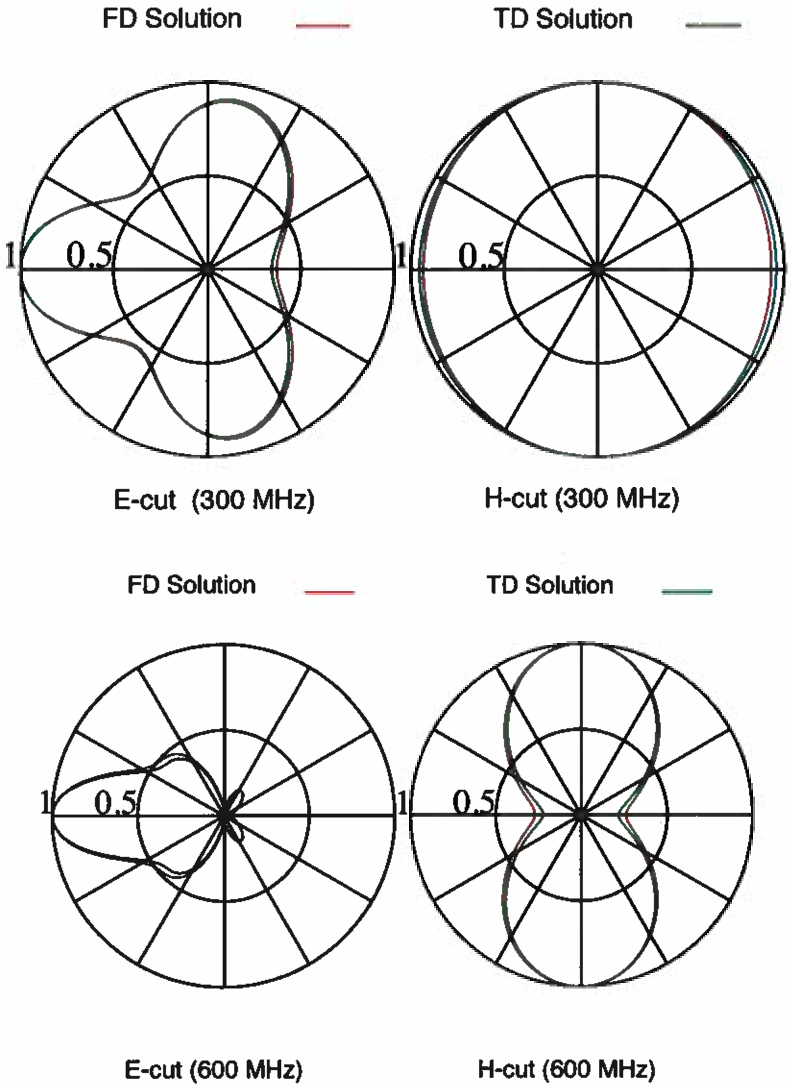

E-cut (300 MHz) H-cut (300 MHz)

E-cut (600 MHz) H-cut (600 MHz)

Fig. 47 — Normalized bistatic RCS of a conducting sphere, radius=0.5 m, located with center coinciding with the origin at 300 MHz and 600 MHz.

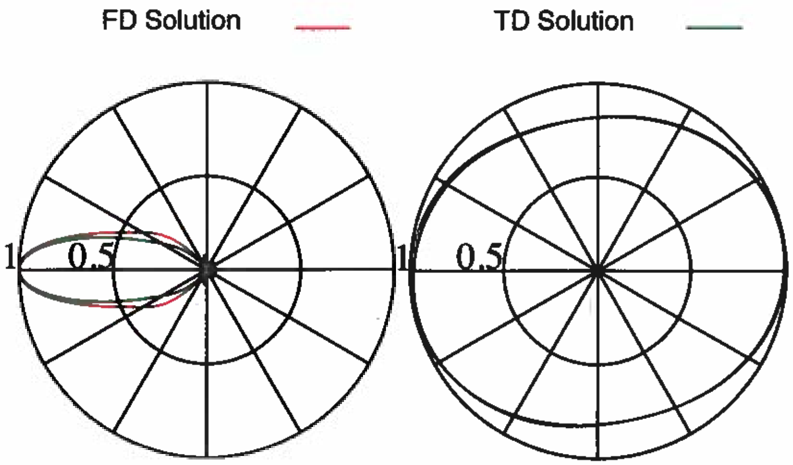

E-cut (900 MHz) H-cut (900 MHz)

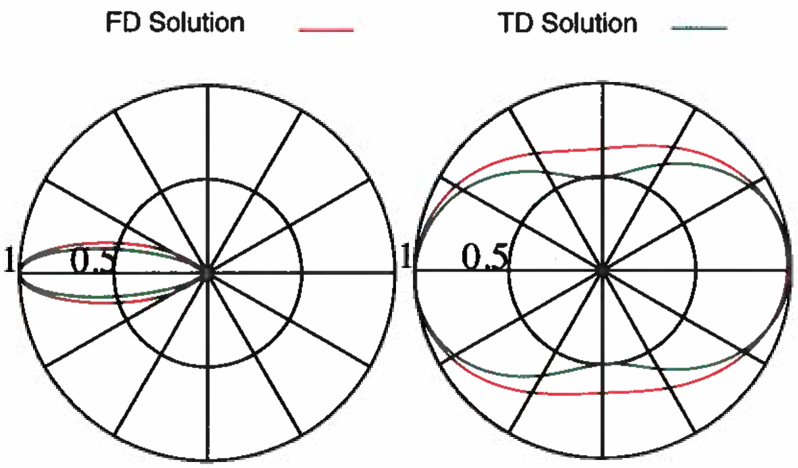

E-cut (1200 MHz) H-cut (1200 MHz)

Fig. 48 — Normalized bistatic RCS of a conducting sphere, radius=0.5 m, located with center coinciding with the origin at 900 MHz and 1200 MHz.

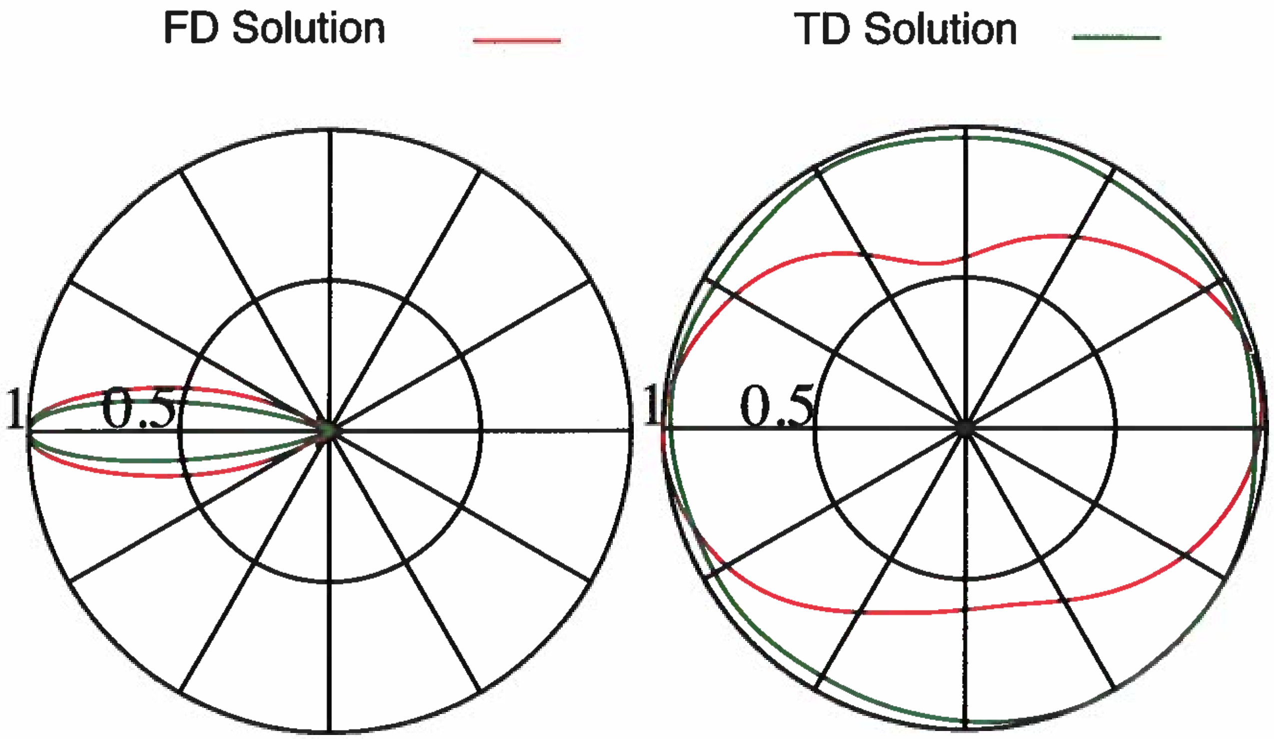

E-cut (1500 MHz)

H-cut (1500 MHz)

Fig. 49 — Normalized bistatic RCS of a conducting sphere, radius=0.5 m, located with center coinciding with the origin at 1500 MHz.

Next, we consider a deep cavity as shown in the inset of Figure 50. For this case, the depth of the cavity is 0.25 m and the inner and outer radii of cavity are 0.08 m and 0.1 m, respectively. The object is symmetrically placed in the XY-plane such that the center of the bottom surface coincides with the coordinate origin. The number of basis functions for this case is 2,208. In Figures 51, 52, and 53, we present the normalized bistatic RCS at 300 MHz, 600 MHz, 900 MHz, 1200 MHz and 1500 MHz and compare with the frequency domain solution. We note a good comparison between the direct time domain solution and the frequency domain solution for the selected frequencies. The differences in the H-cut may be attributed to a weak component of the scattered field.

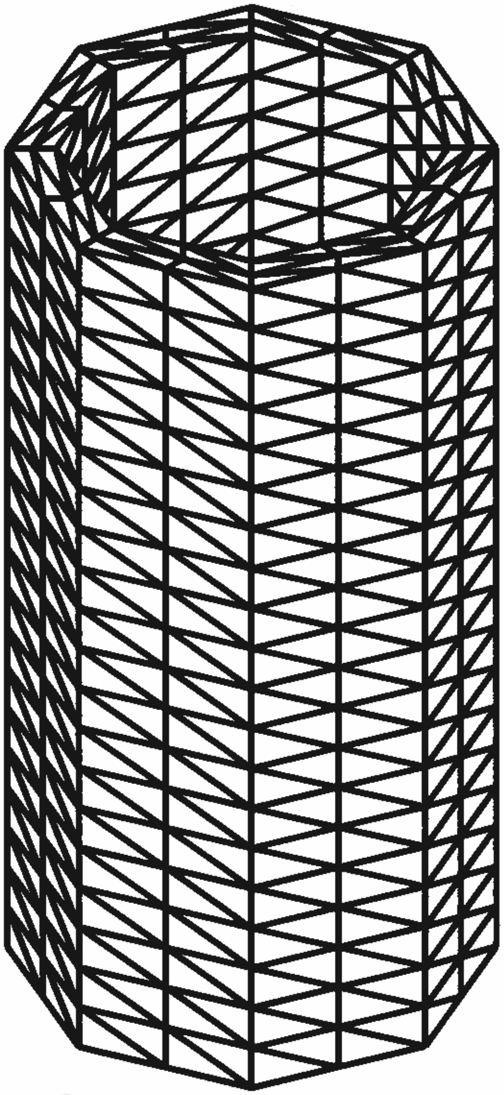

Fig. 50 — Triangulated model of a conducting cavity.

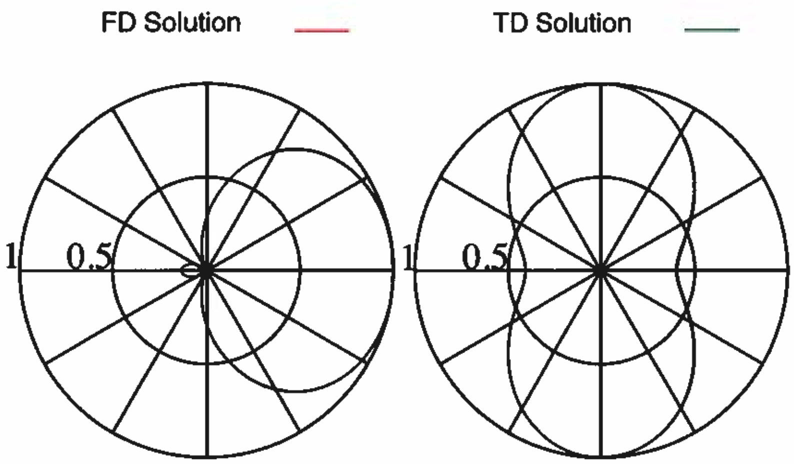

E-cut (300 MHz) H-cut (300 MHz)

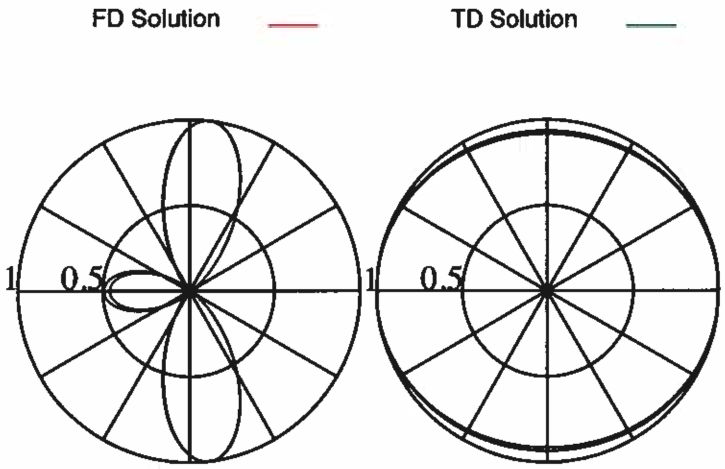

E-cut (600 MHz) H-cut (600 MHz)

Fig. 51 — Normalized bistatic RCS of a conducting cavity, length=0.25 m, inner and outer radii of cavity 0.08 m and 0.1 m, respectively, located with center coinciding with the origin, at 300 MHz and 600 MHz.

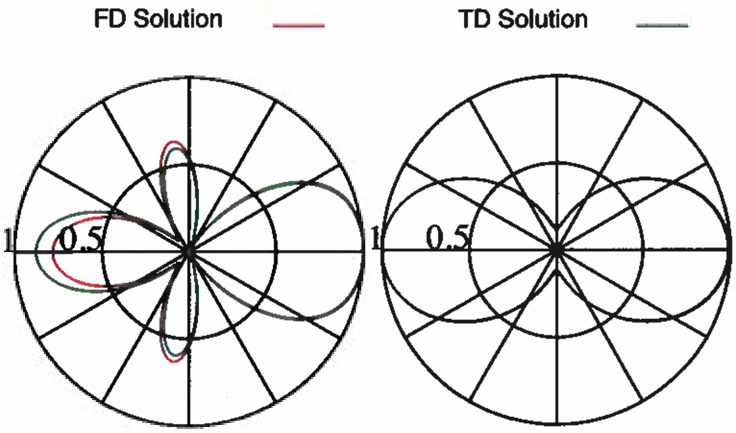

E-cut (900 MHz) H-cut (900 MHz)

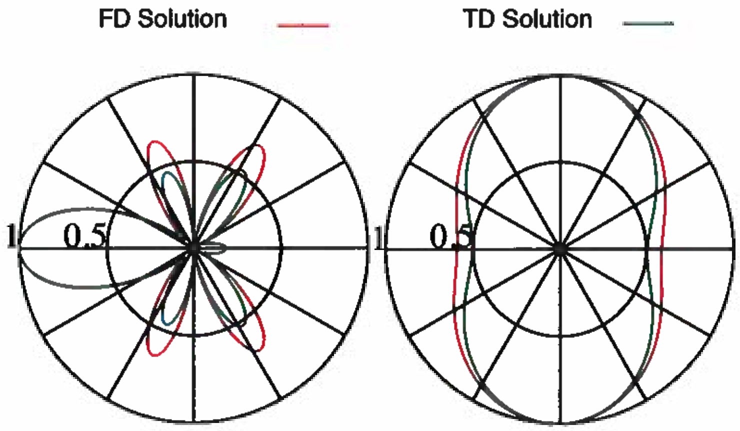

E-cut (1200 MHz) H-cut (1200 MHz)

Fig. 52 — Normalized bistatic RCS of a conducting cavity, length=0.25 m, inner and outer radii of cavity 0.08 m and 0.1 m, respectively, located with center coinciding with the origin, at 900 MHz and 1200 MHz.

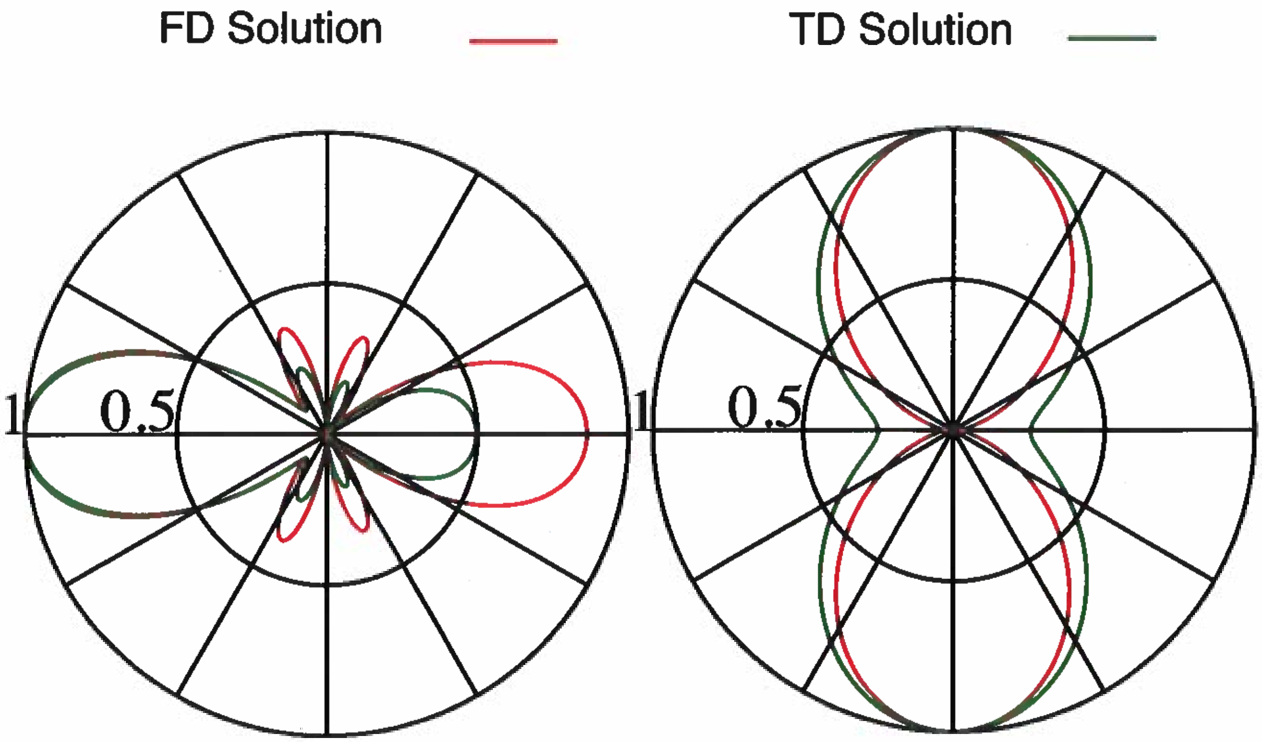

E-cut (1500 MHz)

H-cut (1500 MHz)

Fig. 53 — Normalized bistatic RCS of a conducting cavity, length=0.25 m, inner and outer radii of cavity 0.08 m and 0.1 m, respectively, located with center coinciding with the origin, at 1500 MHz.

Next, we consider an aircraft-like body presented in Figure 54. The body is 48.6 cm long, 43.8 cm wide, and 12.32 cm height. The number of basis functions for this case is 4025. In Figures 55, 56, and 57, we present the normalized bistatic RCS at 300 MHz, 600 MHz, 900 MHz, 1200 MHz, and 1500 MHz and ompared with the frequency domain solution. The figures shows both the elevation cut (E-cut) and azimuthal cut (H-cut) and we note a good comparison between the direct time domain solution and the frequency domain solution.

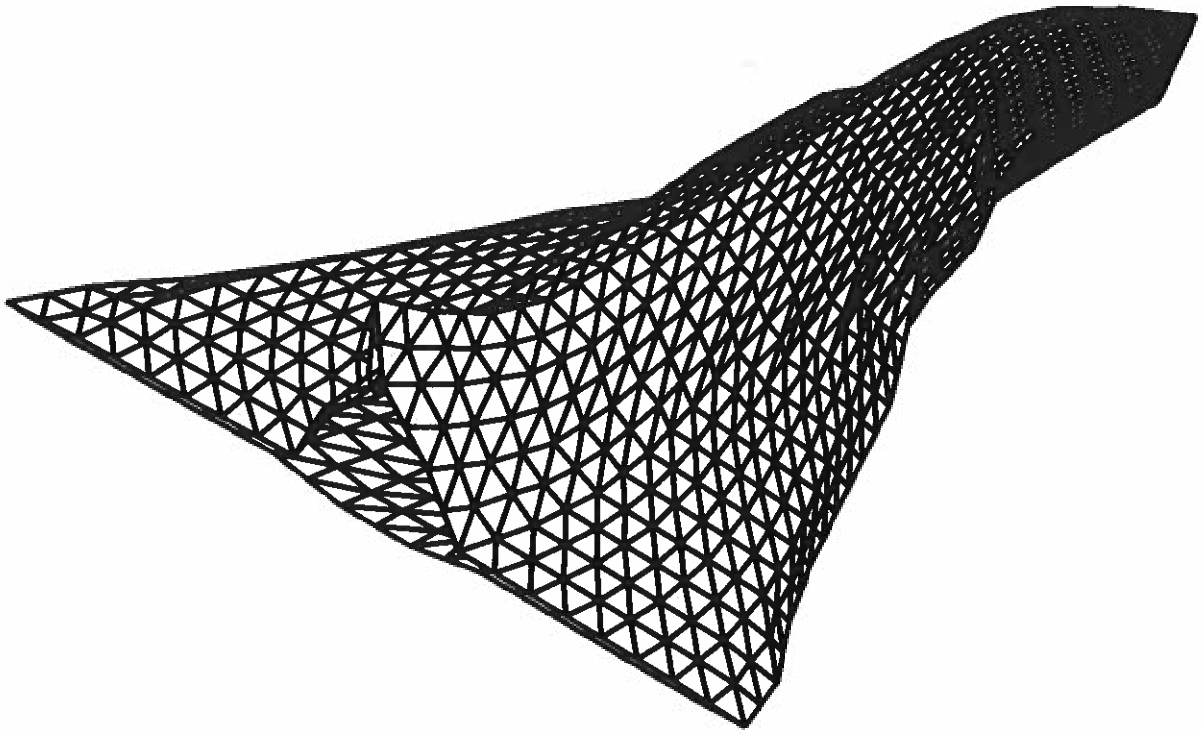

Fig. 54 — Triangulated model of an aircraft-like body. The body is 48.6 cm long, 43.8 cm wide, and 12.32 cm height.

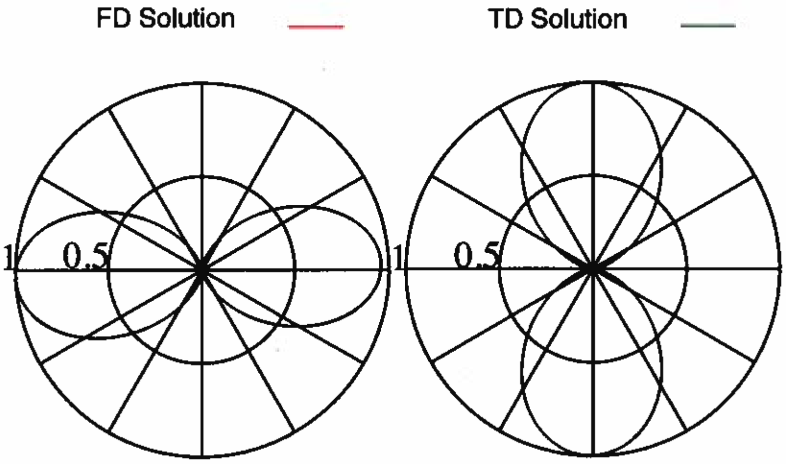

E-cut (300 MHz) H-cut (300 MHz)

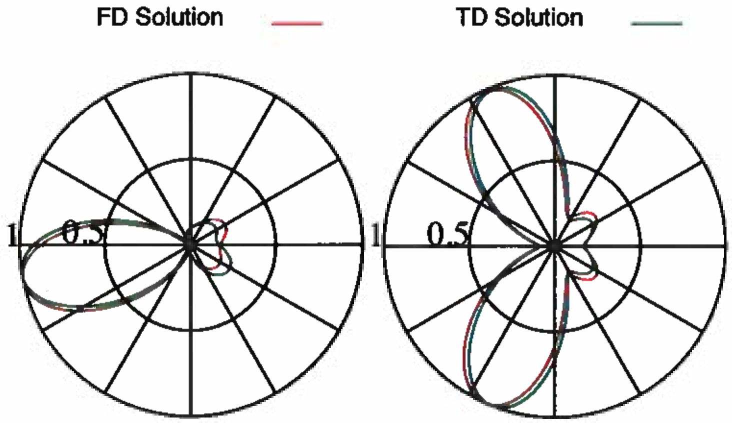

E-cut (600 MHz) H-cut (600 MHz)

Fig. 55 — Normalized bistatic RCS of an aircraft-like body, length=0.5 m, inner and outer radii of cavity 0.08 m and 0.1 m, respectively, located with center coinciding with the origin, at 300 MHz and 600 MHz.

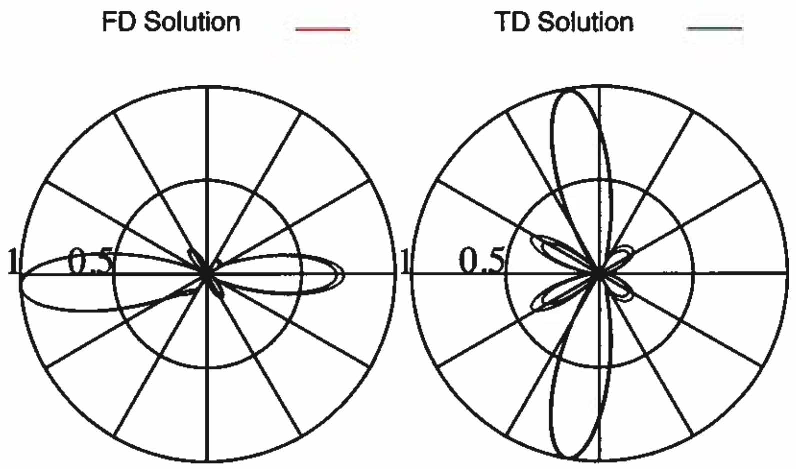

E-cut (900 MHz) H-cut (900 MHz)

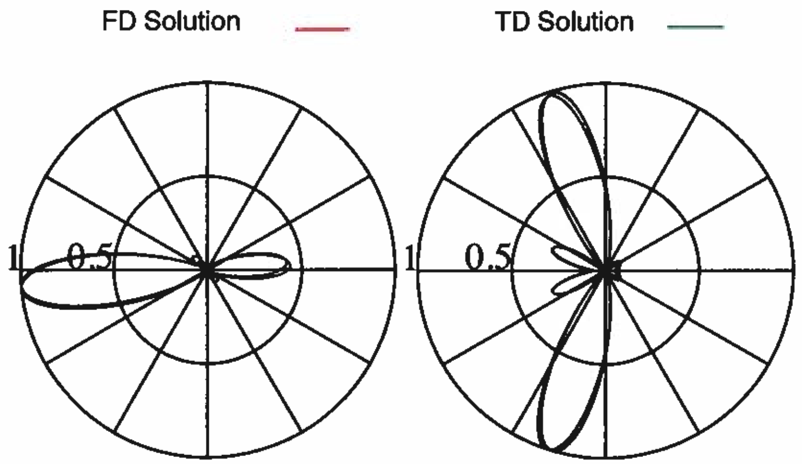

E-cut (1200 MHz) H-cut (1200 MHz)

Fig. 56 — Normalized bistatic RCS of an aircraft-like body, length=0.5 m, inner and outer radii of cavity 0.08 m and 0.1 m, respectively, located with center coinciding with the origin, at 900 MHz and 1200 MHz.

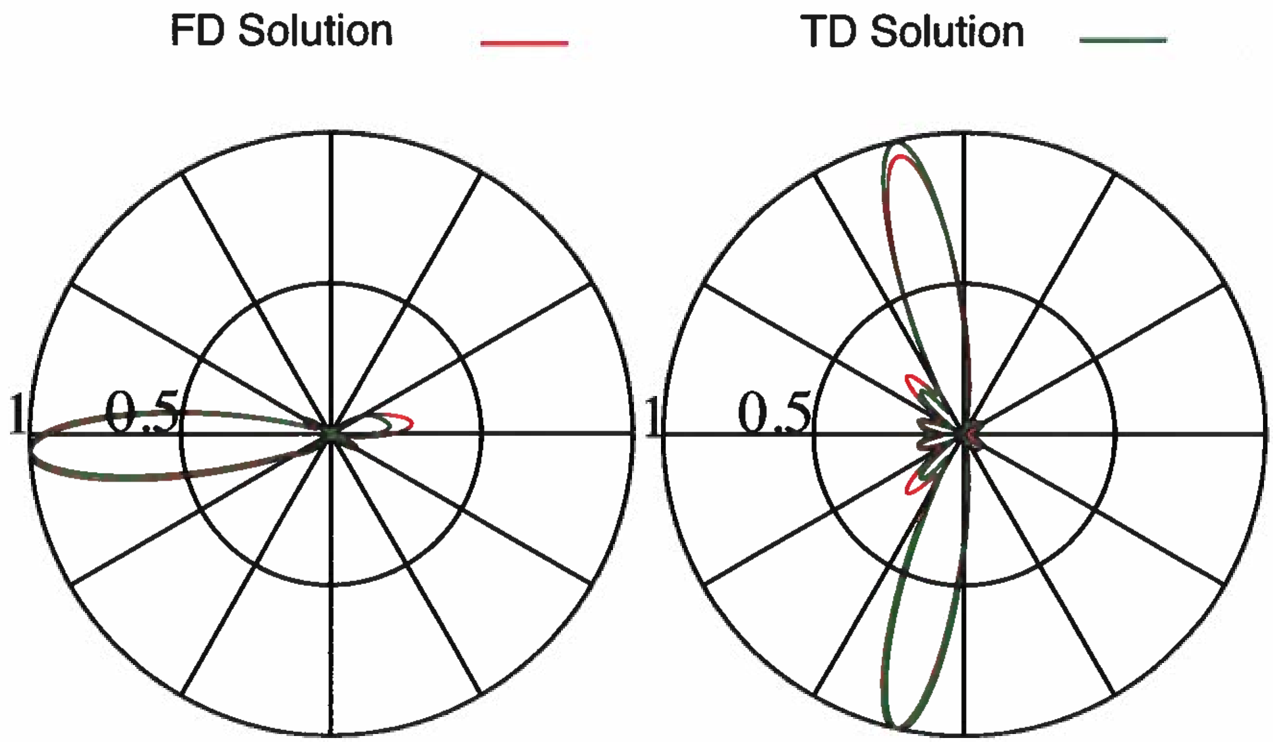

E-cut (1500 MHz) H-cut (1500 MHz)

Fig. 57 — Normalized bistatic RCS of an aircraft-like body, length=0.5 m, inner and outer radii of cavity 0.08 m and 0.1 m, respectively, located with center coinciding with the origin, at 1500 MHz.

Lastly, we consider another aircraft-like body presented in Figure 33. In Figures 58 to 60, we present the normalized bistatic RCS at 100 MHz to 500 MHz at 100 MHz interval and compared with the frequency domain solution. Again, the figures shows both the elevation cut (E-cut) and azimuthal cut (H-cut) and we note a reasonably good comparison between the direct time domain solution and the frequency domain solution.

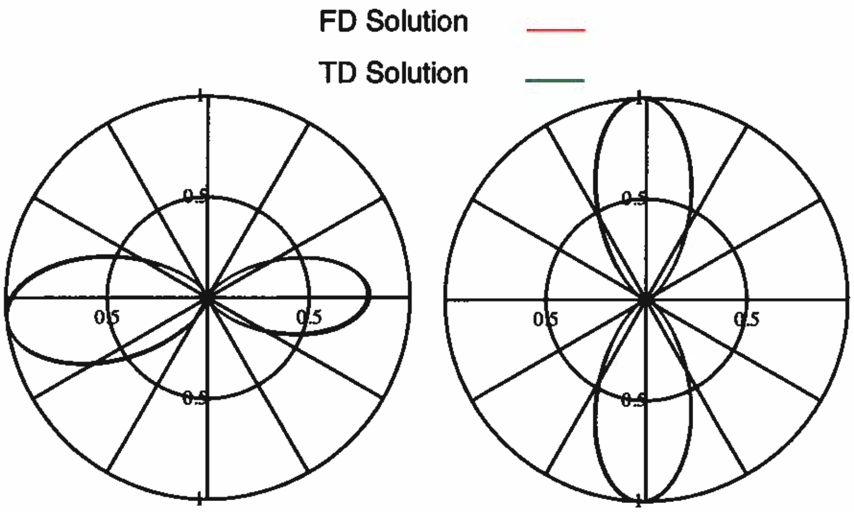

E-cut (100 MHz) H-cut (100 MHz)

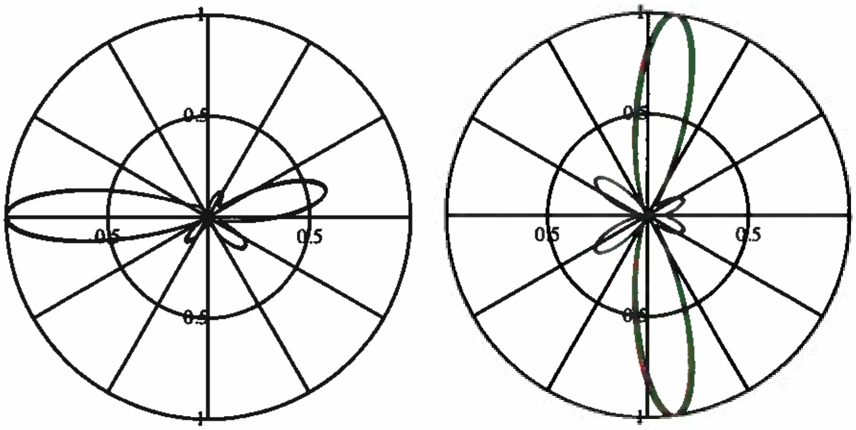

E-cut (200 MHz) H-cut (200 MHz)

Fig. 58 — Normalized bistatic RCS of an aircraft-like body (Figure 33) at 100 MHz and 200 MHz.

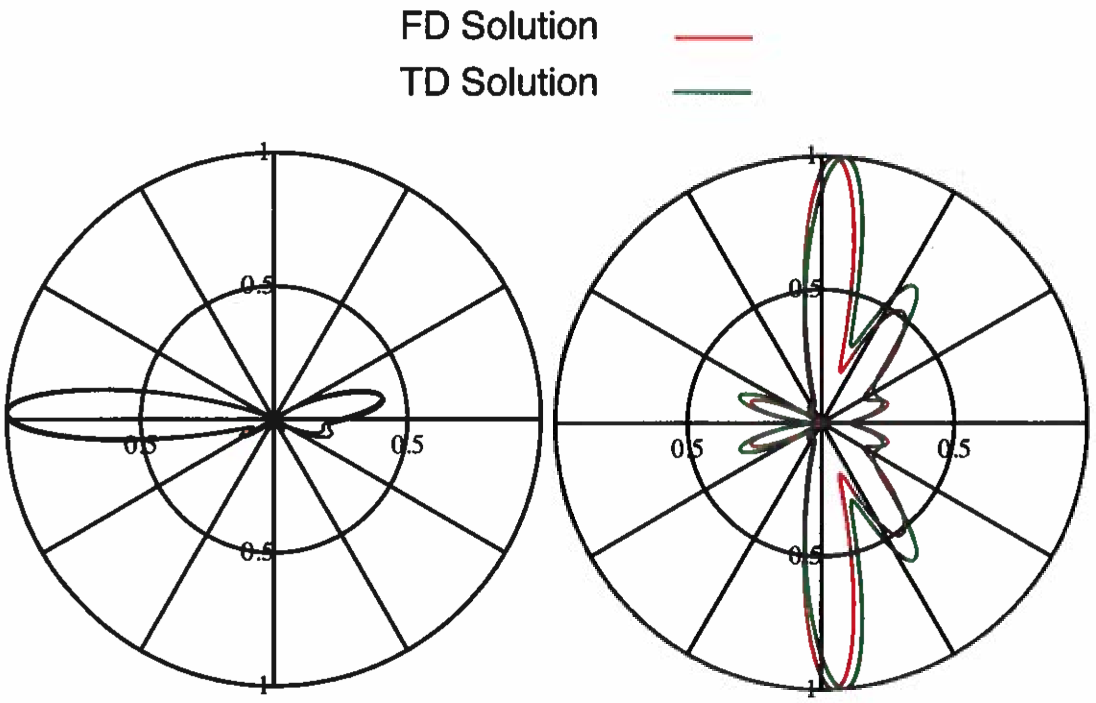

E-cut (300 MHz) H-cut (300 MHz)

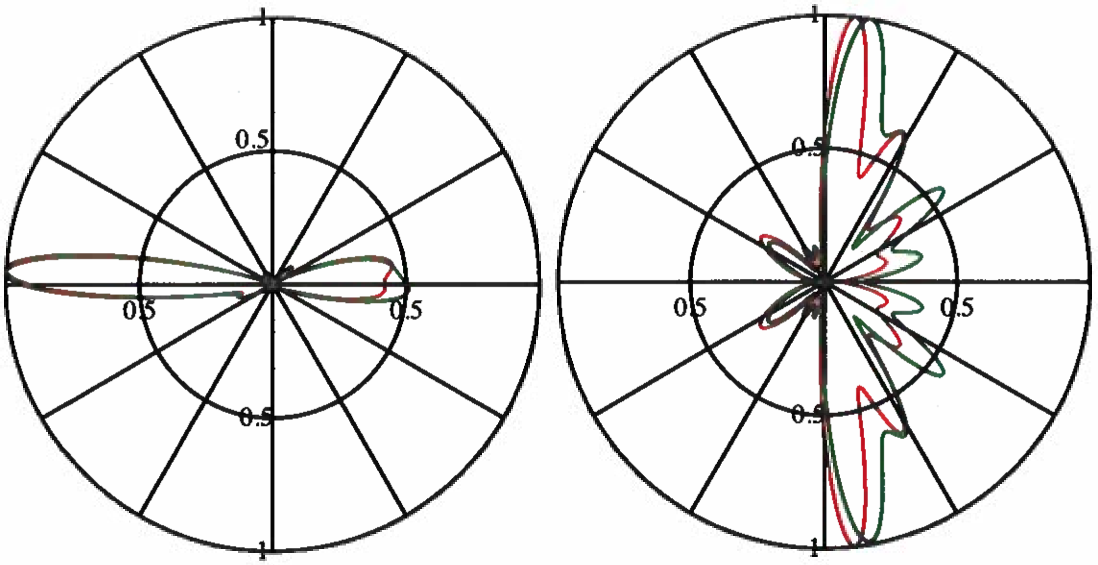

E-cut (400 MHz) H-cut (400 MHz)

Fig. 59 — Normalized bistatic RCS of an aircraft-like body (Figure 33) at 300 MHz and 400 MHz.

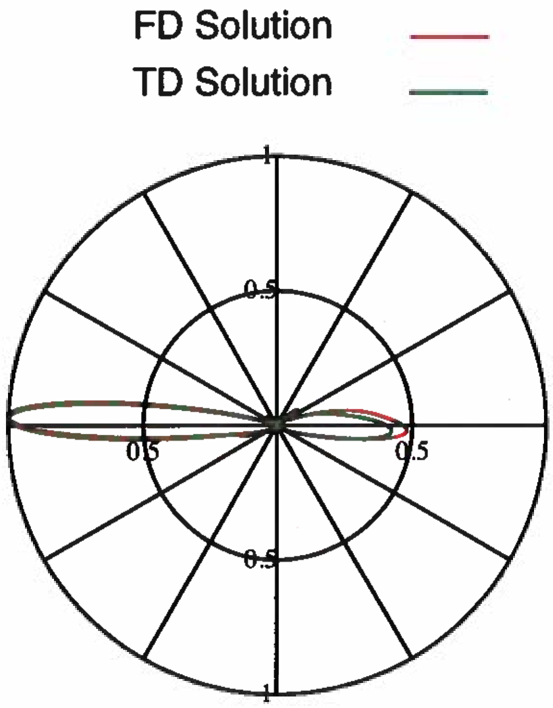

E-cut (500 MHz)

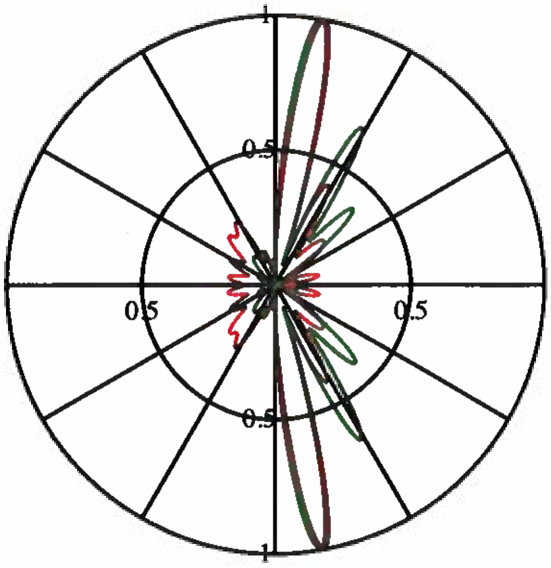

H-cut (500 MHz)

Fig. 60 — Normalized bistatic RCS of an aircraft-like body (Figure 33) at 500 MHz.

6. SUMMARY AND CONCLUSIONS

In this work, a simple and efficient method of moments (MOM) solution procedure is developed to determine the transient scattering from arbitrarily shaped, conducting scatterers by an arbitrary incident pulse directly in the time domain. The scatterer may either be an opened or closed, finite three-dimensional object.

In Chapter 2, conducting bodies are modeled as wire-grids and straight-forward method of moment solution procedure is applied. The wire-grid model enables the development of simple one-dimensional integro-differential equation for the induced current due to an incident pulse. Next, the pulse functions and Gaussian functions are used for expansion of the one dimensional space variable along the length of the wire and time variable, respectively. The testing is carried out by simple point matching procedure for both space and time variables. The resulting method of moments matrix is simply inverted without any further manipulation to obtain the current coefficients. The results for various geometrical shapes are compared with the solution obtained in the frequency domain at a number of frequencies and performing inverse Fourier transform (IDFT Solution). All the numerical results compared well with IDFT solution.

It may be noted that the numerical procedure presented in Chapter 2 is conceptually simple and easy to formulate and yet applicable to any type of complex body. However, the drawback of this procedure is the generation of a large moment matrix and inverting such a matrix is computationally expensive requiring prohibitively large computer time and memory. To overcome this drawback, a simple remedy is developed and executed in Chapter 3. In the new scheme, the Gaussian functions for expanding the time variable are defined in a controlled manner while retaining the pulse functions for the space variable. Further, the testing procedure is completely modified by resorting to Galerkin procedure where the expansion functions for space and time variables are also used as testing functions. The new procedure retained all the advantages of the numerical procedure developed in Chapter 2 with additional benefit being the new MOM matrix is actually a lower-triangular matrix. Further, the new MOM matrix is also block-wise Toeplitz, which requires much lower storage in terms of computer memory. Numerical results with the new procedure are identical to the old procedure and requires only a fraction of computer resources.

Next, in Chapter 4, arbitrarily shaped, three-dimensional bodies via patch modeling scheme were investigated. Note that patch-modeling scheme is superior to wire-grid modeling method because the electromagnetic conditions are enforced in a more accurate manner. In this work, the bodies were modeled by a set of triangular patches. Triangular patches have the ability to conform to any geometrical boundary or surface. The EFIE was used for the conducting case so that open or closed surfaces could be analyzed.

Finally, in Chapter 5, radar cross section (RCS) of many objects at various selected frequencies are calculated and compared with the frequency domain solution. It is important to note that only one simulation in the time domain is necessary to compute the RCS for various frequencies whereas the frequency domain solution needs to be performed for each frequency separately.

This work presented in this report can be extended in several different ways. The new procedure needs to be extended to dielectric bodies and dielectric coated conductors. This could be useful to stealth-type technology. The analysis could first be performed on two-dimensional bodies and then applied to three-dimensional ones.

Another area of further research could be in the area of target identification. The transient response obtained by this method may be used to extract the poles. These poles could then be used in identifying the object or to create various types of extinction pulses. Or, a library could be created for the returns from objects at various angles which could then be used with signal processing techniques in identifying a specific return.

REFERENCES

1. E. K. Miller, "Direct time-domain techniques for transient radiation and scattering form wires," *Proceedings of the IEEE* **68**, 1396–1423 (1980).
2. C. L. Bennett and G. F. Ross, "Time-domain electromagnetics and its applications," *Proceedings of the IEEE* **118**, 1203–1209 (1971).
3. K. S. Yee, "Numerical solution of initial boundary value problems involving maxwell's equations in isotropic media," *IEEE Transactions on Antennas and Propagation* **14**(3), 302–307 (1966).
4. P. B. Johns and R. L. Beurle, "Numerical solution of 2-dimensional scattering problems using a transmission line matrix," *Proceedings of the IEEE* **66**, 299–318 (1978).
5. R. F. Harrington, *Field Computation by Moment Methods* (Macmillan, New York, 1968).
6. E. M. Kennaugh and R. L. Cosgriff, "The use of impulse response in electromagnetic scattering problems," in *IRE National Convention Record*, pp. 72–77 (1958).
7. T. T. Wu, "Transient response of a dipole antenna," *Journal of Mathematical Physics* **2**(6), 892–894 (1961).
8. C. L. Bennett, *A Technique for Computing Approximate Electromagnetic Impulse response of conducting bodies* (Purdue University, PhD Thesis, 1968).
9. S. M. Rao, *Time Domain Electromagnetics* (Academic, New York, 2000).
10. D. A. Vechinski and S. M. Rao, "A stable procedure to calculate the transient scattering by conducting surfaces of arbitrary shape," *IEEE Transactions on Antennas and Propagation* **40**(6), 661–665 (1992).
11. A. Sadigh and E. Arvas, "Treating the instabilities in marching-on-in-time method from a different perspective," *IEEE Transactions on Antennas and Propagation* **41**(12), 1695–1702 (1993).
12. A. J. Pray, N. V. Nair, and B. Shanker, "Stability properties of the time domain electric field integral equation using a separable approximation for the convolution with the retarded potential," *IEEE Transactions on Antennas and Propagation* **60**(8), 3772–3781 (2012).
13. L. P. Zha, Z. H. Fan, D. Z. Ding, and R. S. Chen, "Time domain analysis of electromagnetic scattering problems by using integral equation method with space-delayed temporal basis functions," *IEEE Transactions on Antennas and Propagation* **62**(11), 5846–5851 (2014).
14. Y. S. Chung, T. K. Sarkar, B. H. Jung, M. S. Palma, Z. Ji, S. Jang, and K. Kim, "Solution of time domain electric field integral equation using the laguerre polynomials," *IEEE Transactions on Antennas and Propagation* **52**(9), 2319–2328 (2004).
15. Y. S. Chung, Y. Lee, J. So, J. Kim, C. Y. Cheon, B. Lee, and T. K. Sarkar, "A stable solution of time domain electric field integral equation using weighted laguerre polynomials," *Microwave and Optical Technology Letters* **49**(11), 1263–1264 (2007).
16. D. Omri and T. Aguili, "Electromagnetic coupling analysis of transient excitations of rectangular cavity through slot using td-efie with laguerre polynomials as temporal basis functions," *ACES Journal* **31**(10), 1221–1231 (2016).

17. S. M. Rao, D. A. Vechinski, and T. K. Sarkar, "Transient scattering by conducting cylinders - implicit solution for transverse electric case," *Microwave and Optical Technology Letters* **21**, 129–134 (April 1999).

18. S. M. Rao and T. K. Sarkar, "Implicit solution of time domain integral equations for arbitrarily shaped dielectric bodies," *Microwave and Optical Technology Letters* **21**, 301–205 (May 1999).